ALMA MATER STUDIORUM
Universitá di Bologna

SCUOLA DI SCIENZE
Corso di Laurea in Astrofisica e Cosmologia
Dipartimento di Fisica e Astronomia

A STUDY OF THE TURBULENCE OF THE NEUTRAL MEDIUM IN TWO NEARBY SPIRAL GALAXIES

Elaborato finale

Candidato:

Francesco Brignoli

Relatore:

Chiar.mo Prof.

Filippo Fraternali

Co-relatore:

Prof. Dr.

Tom Oosterloo

Sommario

La larghezza della riga a 21 cm emessa dalle galassie a spirale dipende dai processi fisici che liberano energia nel mezzo interstellare. La larghezza viene stimata misurando la cosiddetta dispersione di velocità (σ), che è proporzionale in primo luogo all'energia cinetica del gas. In questo contesto, l'idrogeno neutro (HI) è naturalmente portato a segregarsi in due fasi termodinamiche stabili, che possono coesistere entro un certo intervallo di densità del mezzo. Tali fasi vengono dette "Cold Neutral Medium" (CNM) e "Warm Neutral Medium" (WNM), e avrebbero larghezze di riga tipiche di $\sigma_{\mathrm{CNM}} \sim 0.8$ km s^{-1} e $\sigma_{\mathrm{WNM}} \sim 8$ km s^{-1}. Questo quadro teorico è tuttavia messo in discussione dall'evidenza che la dispersione nel gas interstellare può assumere uno spettro di valori molto più ampio di questo. Tali osservazioni dimostrano che - oltre all'allargamento termico - altri processi energetici sono in atto nel mezzo interstellare. È comune attribuire questi ultimi a fenomeni di turbolenza, ma resta ad oggi aperto il dibattito sulla loro origine.

Nel presente lavoro abbiamo studiato l'emissione a 21 cm di due galassie a spirale dell'universo vicino: NGC 6946 e M 101. Per quest'ultima abbiamo fatto uso di nuove osservazioni ottenute dall'interferometro di Westerbork (NL), mentre per la prima di osservazioni già presentate in passato (Boomsma et al., 2008). Per entrambe le galassie, abbiamo ottenuto precise misure della dispersione di velocità dei singoli profili, attraverso fit svolti con una funzione gaussiana. Contrariamente ad altri studi, abbiamo individuato e scartato i profili che mostravano una struttura asimmetrica o doppi picchi, in quanto riteniamo problematico definire una misura realistica della dispersione di velocità in questi casi.

La nostra analisi si è focalizzata su due temi principali. In primo luogo abbiamo confrontato i valori della dispersione nelle regioni dei bracci a spirale delle galassie con quelli delle regioni degli intrabracci. Abbiamo studiato come variano, tra un caso e l'altro, le relazioni fra σ e la densità di colonna e fra σ e il flusso di picco dei singoli profili. L'analisi statistica che abbiamo condotto non ha mostrato differenze palesi fra bracci ed intrabracci, sebbene si osservi che in certe regioni intrabraccio si raggiungono le dispersioni più elevate. Sia per i bracci, sia per gli intrabracci di NGC 6946, si osserva una crescita della dispersione media con la densità di colonna. Questo è parzialmente in disaccordo con risultati che attribuiscono alle regioni dei bracci le dispersioni più elevate (Shostak and van der Kruit, 1984). In M 101 tuttavia, l'andamento ottenuto è opposto, in quanto le dispersioni medie sono più elevate per

basse densità di colonna (sia per i bracci, sia per gli intrabracci).

La seconda linea di analisi è consistita nell'indagare il ruolo che occupano, nelle due galassie, i fenomeni di formazione stellare nell'innesco della turbolenza. Per questo abbiamo realizzato le mappe del tasso di formazione stellare per unità di superficie (*star formation rate density*). Abbiamo dunque studiato la relazione presente fra l'energia cinetica dell'idrogeno neutro per unità di superficie, dedotta dalla dispersione di velocità ($3/2 \, \Sigma_{HI}\sigma_{HI}{}^2$) e il tasso di formazione stellare per unità di superficie (Σ_{SFR}), seguendo un'approccio già utilizzato da Tamburro et al. (2009). Per NGC 6946 le due quantità mostrano un buon grado di correlazione, che diviene ottimo considerando le regioni centrali, con più intensa attività stellare. I dati si mostrano in accordo con un semplice modello di turbolenza indotta al mezzo interstellare da esplosioni di supernova. Per quanto riguarda M 101, la relazione ottenuta per la totalità della galassia risulta molto diversa, con una densità di energia cinetica del gas approssimativamente costante su tutto il disco. Tuttavia, considerando un'area di formazione stellare localizzata a Est dal centro della galassia, si riottiene in M 101 la stessa correlazione osservata per NGC 6946, quindi in ottimo accordo con il modello teorico di turbolenza da supernova.

Riteniamo che la differenza fra le due galassie sia da interpretare riconducendo l'innescarsi della turbolenza a due diversi processi fisici. Mentre per NGC 6946 essa può essere giustificata ammettendo un contributo prevalente da parte dei processi di formazione stellare, in M 101 devono essere in atto altri fenomeni. Visto che la struttura di questa galassia risulta globalmente perturbata, e vista la presenza di una enorme nube ad alta velocità che con ogni probabilità sta interagendo con il disco, è ragionevole imputare il comportamento di M 101 a fenomeni di accrescimento di materia extragalattica o di forte interazione con galassie satelliti.

Contents

Chapter 1

Introduction

In this Chapter we make up the main topics that compose the scientific background of this thesis. In Sect. 1.1 we briefly describe the composition of the Interstellar Medium (ISM) in the spiral galaxies, particularly focusing on the properties of the neutral atomic medium. In Sect. 1.2 we define what the velocity profile of the neutral hydrogen is, and we illustrate the physical information that can be inferred from it. Sect. 1.3 is dedicated to the turbulent phenomena that are thought to be present in the ISM. Finally, in Sect. 1.4 we outline the main goal of the present work, and the strategies used to achieve it.

1.1 The Interstellar Medium in spiral galaxies

Spiral galaxies are known to be constituted for a significant fraction by a non-stellar component. This is composed by atomic and molecular, neutral and ionized phases, and by dusts. As a whole, it is usually referred to diffuse matter or Interstellar Medium (ISM). The most abundant element that forms the ISM is hydrogen, that contributes $\sim 90\%$ of the total interstellar matter in the galaxies (Brinks, 1990). The atomic matter can be found in four possible phases (Tielens, 2010):

- **Cold Neutral Medium (CNM)**, with typical temperatures of T ~ 80 K and volume densities n ~ 50 cm^{-3}.

- **Warm Neutral Medium (WNM)**, with T $\sim$ 6000-8000 K and n $\sim$ 0.1 cm^{-3}.

- **Warm Ionized Medium (WIM)**, with T $\gtrsim 8000$ K and n ~ 0.5 cm^{-3}.

- **Hot Ionized Medium (HIM)**, with T $\sim 10^6$ K and n ~ 0.001 cm^{-3}.

As visible from the listed values, the atomic phases of the ISM has a complex thermal, density and ionization structure. However, both theoretical and observational arguments, suggest that they should coexist in approximate pressure equilibrium. A fraction of the ISM component ($\sim 50\%$) is constituted by **molecular gas**, that is cold (T $<$ 50 K) and generally collected in self-gravitating clouds of various sizes and densities.

The theory of the Interstellar Medium that is generally accepted today is based in the seminal paper by McKee and Ostriker (1977). They proposed a model of inhomogeneous ISM, composed by pc-scale clouds with a cold core and a warm (neutral and ionized) envelope. These structures would be embedded in the hot medium, which should fill roughly half of the total volume of the ISM (Fig. 1.1). These phases can coexist at the equilibrium pressure of:

$$< p > \sim 3 \times 10^{-13} \text{ dyne cm}^{-2}$$

The HIM should be continuously feed by the remnants of supernova explosions, that, in this model, are the main regulators of the three phase structure of the ISM.

A first observational evidence of a pressure equilibrium between the various media came from the study of Myers (1978), who calculated temperature, density and thermal pressure of different gaseous components of the ISM. His results showed that most of these could be confident within a pressure range spanning ~ 2 orders of magnitude, while T and n are changing by 5-6 orders of maginitude (Fig. 1.2).

A number of details still need to be included in a coherent picture of the ISM. One of the most debated issues is the role of turbulence, as we will outline in Sect. 1.3.

1.1.1   Neutral hydrogen and the "two-phase model"

If we consider just the two neutral atomic phases (CNM and WNM, together called HI), the picture is simpler.

Hydrogen is the simplest element in nature, composed by one proton and one electron. In its ground state, considering the spin of the electron and that of the proton, two different couplings can occur among them. These two levels have slightly different energies: when the atom de-excites from the highest level, an emission line

is emitted at a frequency:

$$\nu_{\mathrm{rest}} \sim 1420.4058 \text{ MHz} \sim 21.1\text{cm}$$

Even though the corresponding Einstein coefficient for the spontaneous emission is very low ($A_\nu = 2.9 \times 10^{-15}$ s-1), the huge abundance of neutral hydrogen makes this emission widespread in the Universe, and of crucial importance in astronomy. This widespread emission was theoretically predicted in 1944 by the Dutch physicist H.C.Van de Hulst (Van de Hulst, 1945). The observational evidence followed a few years later, with a joined publication by US (Ewen and Purcell, 1951), Dutch (Muller and Oort, 1951) and Australian scientists (Christiansen and Hindman, 1951).

Field et al. (1969) noticed that, if one assumes thermal balance between the heating and the cooling processes in the ISM, temperature is not a monotonic function of density (Fig. 1.3). The negative slope portion visible in between the two black points corresponds to an unstable density range of the medium (this is known as the "Field criterion", Field, 1965). The horizontal dotted line in the picture indicates the average pressure for which two density stable phases can coexist.
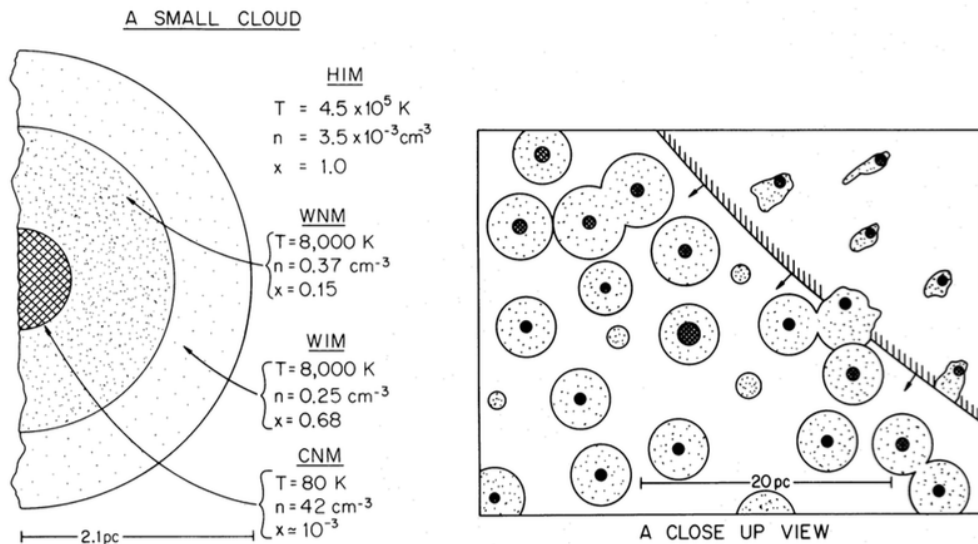
Figure 1.1: Figg. 1 and 2 from McKee and Ostriker (1977), describing their model of a three-phase ISM. **Left -** Cross section of a typical small cloud. The CNM occupies the central core, enveloped by the WNM and by an outer ionized layer (WIM). The region between the clouds is filled with the HIM. Typical temperatures T, number densities n and ionization fractions x are indicated. **Right -** Small-scale structure of the ISM (the box is 30×40 pc big). From the upper right a SN blast wave is expanding in the medium: the warm envelopes of the clouds are distorted by the remnant and evaporate, feeding the HIM.
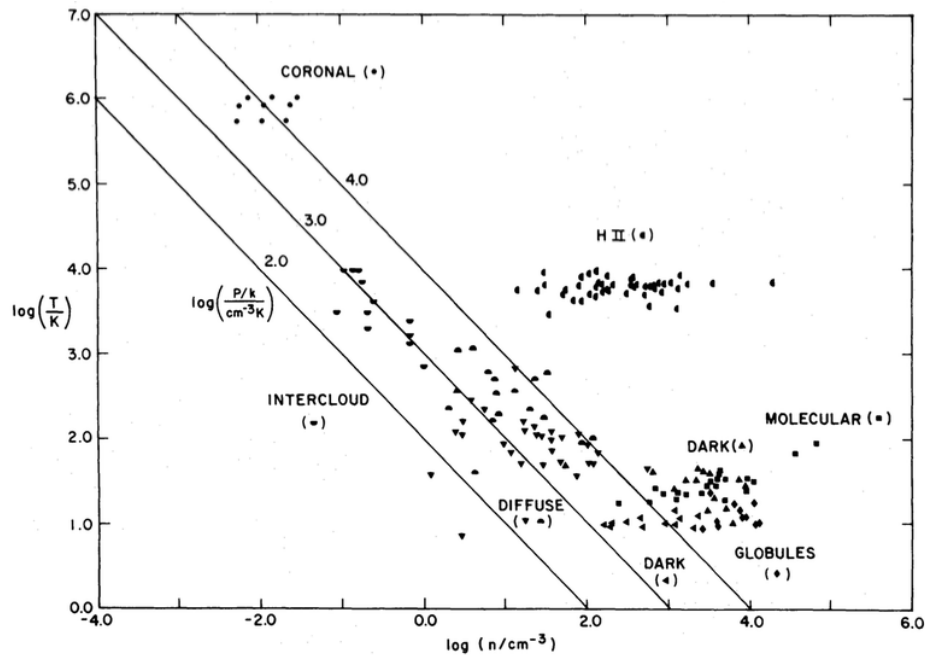
Figure 1.2: Fig. 1 from Myers (1978). The author collected different observations of the ISM in a range of temperature $1 < \log (T\ [K]) < 6$, and of density $-2 < \log (n\ [cm^{-3}]) < 5$. The various emitting sources are indicated in the plot. The data are roughly confident within 2 orders of magnitude from the average pressure, excluding the ionized HII regions (which are expanding) and the dark clouds (for which self-gravity cannot be neglected).

In this description the neutral medium is expected to be composed by a collection of dense and cold clumps, immersed in a warmer and more diffuse materia (the two stable points in Fig. 1.3). A portion of gas at intermediate densities/temperatures has to be considered temporary. Observed densities and pressures of the CNM and the WNM seem to well correspond to those expected from the Field criterion (Wolfire et al., 1995). Hence, neutral atomic gas is usually considered a "two-phase medium".

1.2 Observing at 21 cm: datacubes and velocity profiles

HI observations of galaxies are usually referred to as "datacubes". In them, each pixel contains the value of the HI emission of an ensemble of clouds, defined by three coordinates: Right Ascension, Declination (i.e. the position on the sky) and velocity along the line of sight (Fig. 1.4(a)). Line emission from disk galaxies is in fact subjected to Doppler shift due to its rotation motions. For this reason, different parts of a galaxy have different velocities with respect to the observer. Obviously, this causes the radiation coming from different areas of the object to have different

wavelengths, as a consequence of the relation:

$$1 - \frac{\lambda_{\text{rest}}}{\lambda_{\text{obs}}} = \frac{v}{c}$$

where λ_{obs} is the observed wavelength of the radiation, λ_{rest} the rest wavelength of the HI line ($\sim$ 21,1 cm), v the line-of-sight velocity of the gas in the region in question, while c is the speed of light.

In a datacube, the HI emission is "discretized" in "*voxels*", i.e. 3-D pixels with two spatial and one frequency dimensions. In the frequency dimension the cube is divided in "channels", and we call the frequency separation between them "channel width" of the data cube. An image at a certain frequency (velocity) is called channel map. If we fix the R.A. and Dec. position on the sky, and we extract the flux at the various velocities, we are observing the **velocity line profile** of the sky area corresponding to that position (Fig. 1.4(b)).

1.2.1 The velocity dispersion

A quantity that is of capital importance in the present work is the **velocity dispersion** of the gas (usually indicated with the Greek letter σ). Here we just
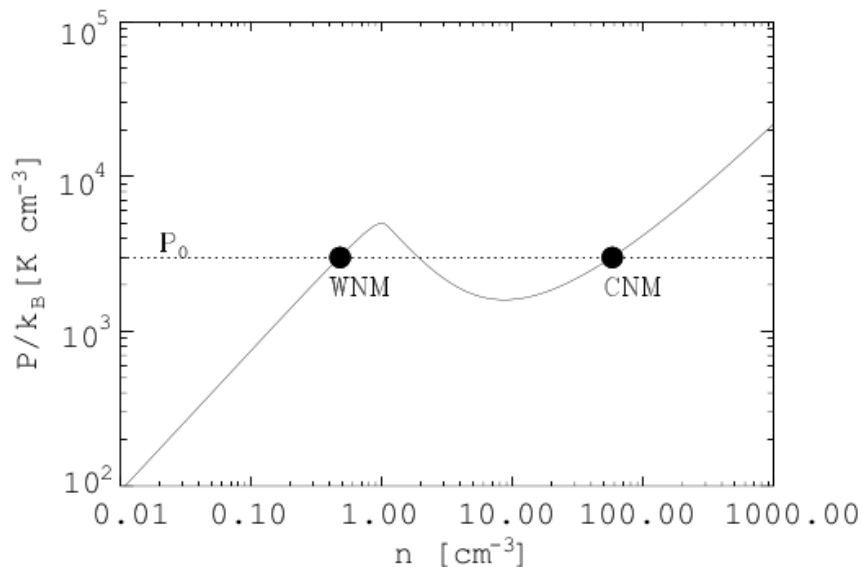
Figure 1.3: Illustration of the thermal pressure-temperature relation for the atomic ISM, in case of equilibrium between heating and cooling. The unstable region corresponds to the negative slope portion of the continuous curve. The horizontal dotted line indicate the mean pressure P_0 for which two stable phases of the medium can coexist (picture taken from Vázquez-Semadeni (2012)).
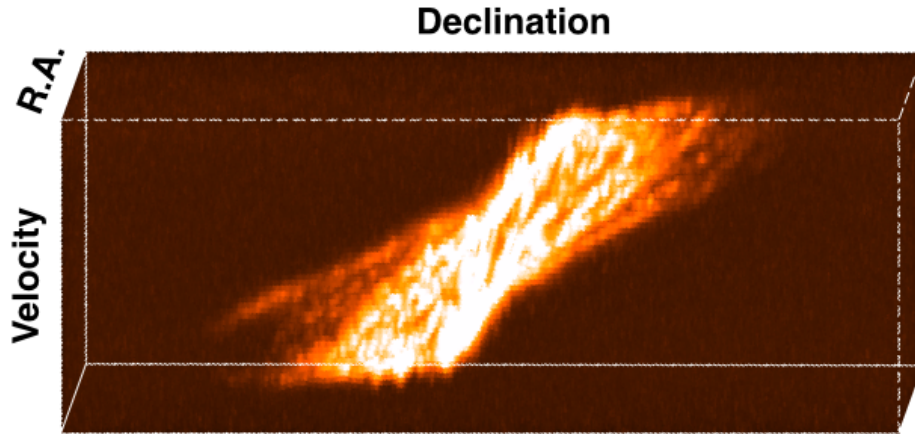
(a) 3-D datacube
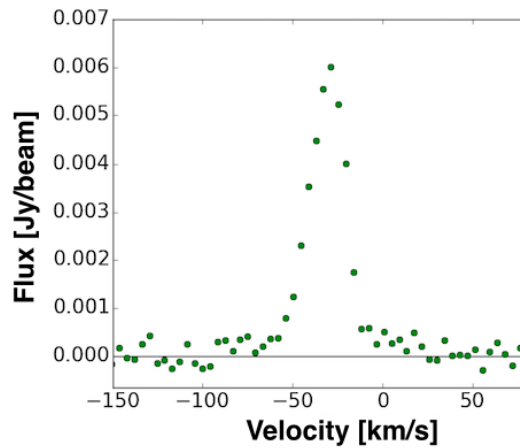
(b) Velocity profile

Figure 1.4: (a) 3-D visualization of the datacube of the spiral galaxy NGC 2403 (Fraternali et al., 2002): radio-astronomical line data are usually collected in this format. (b) Example of a line profile at a given R.A. and Dec. position extracted from the datacube of NGC 6946, one of the galaxies analysed in this thesis.

introduce the meaning of this quantity, while we refer to Sect. 2.3 for a description of the mathematical methods used to estimate it.

Reminding that the ISM - under certain conditions - can be described as a fluid (Clarke and Carswell, 2014), we define as a "fluid element" a volume of gas big enough that the mean free paths of the single particles contained are negligible. Moreover, it has to be small enough that we can ignore significant variations of the thermodynamical quantities within it. Every pixel of a datacube carries information of the motion of many fluid elements composing the ISM. The single gas particles

contained in every fluid element has random motions that we assume isotropic, and we can define an average velocity for each element. The velocity dispersion of the fluid elements contained in a pixel provides a measure of the range of velocities that they can assume, compared to the average velocity of that position.

This quantity can be inferred, for every pixel, from its line emission profile. Indeed, referring to the that in Fig. 1.4(b), we see that the emission comes from a range of channels centred around a peak. We remind that every channel corresponds to a different velocity with respect to the observer. Then, the more numerous are the channels with significant emission, the more the fluid elements in that pixel can assume different velocities from each other. From the broadening of the line profile we extract the value of the velocity dispersion.

It is important to be aware of the fact that velocity dispersion is not a quantity directly measured in an observation, but it is *derived* from the data. This means that we have to perform some mathematical calculations to obtain it (see Sect. 2.3). For this reason the definition of dispersion is not univocally established, and in the literature it is still debated what is the most correct way to measure it (see for instance the appendix of the recent work by Mogotsi et al., 2016).

In an ISM dominated by thermal pressure, it is straightforward to predict the typical velocities that the two HI phases should have. From the kinetic theory of gas we know that the average velocity dispersion of the medium in one of the three Cartesian directions is:

$$< v > = \sqrt{\frac{k_{\mathrm{B}}\, T}{m_{\mathrm{H}}}} \tag{1.1}$$

where k_{B} is the Boltzmann constant, T the kinetic temperature of the gas, m_{H} the hydrogen atom mass.

If we substitute in Eq. (1.1) the typical temperature of the CNM and of the WNM (cfr. Sect. 1.1), we obtain:

$$< v_{\mathrm{CNM}} > \sim\ 0.8\ \mathrm{km\ s}^{-1} \qquad < v_{\mathrm{WNM}} > \sim 8\ \mathrm{km\ s}^{-1} \tag{1.2}$$

1.3 Turbulence in the ISM: evidence and controversy

In spite of the apparently convincing theoretical picture of the ISM thermal structure described in Sect. 1.1, it is known that reality is more complicated. Already Dickey et al. (1977) observed a continuous distribution of neutral hydrogen tempera-

ture in the Milky Way, thus encompassing also he expected "unstable" regime. Successively, many authors showed that interstellar gas commonly exists in the region "forbidden" by the Field criterion (the negative slope portion in Fig. 1.3), inducing some authors to wonder whether there are really three phases in the ISM, rather than some kind of "continuous" distribution (Vázquez-Semadeni, 2012).

Taken from a different perspective, these observations demonstrate that the pressure of the ISM cannot originate just from thermal energy. A more complete description should include several other factors, such as cosmic rays, galactic magnetic field, dynamical phenomena like ram-pressure or macroscopic gas flows. In particular, the role of turbulent gas motions seem to be fundamental to understand the physics of the ISM (for comprehensive reviews on this topic see for instance Elmegreen and Scalo, 2004, Scalo and Elmegreen, 2004).

We can define turbulence as a chaotic gas motion not ascribable to thermal broadening (see Sect. 1.3.1). One of the most important phenomena where the turbulence is invoked comes indeed from kinematics studies of the HI emission in nearby galaxies. Measuring the velocity dispersion of the 21 cm radiation, all studies have shown that this reaches values up to 20 km s^{-1} in the inner parts of galaxies and typically maintains values of $\sigma \sim$ 7-8 km s^{-1} out to the outermost regions of the gaseous disks (e.g. Shostak and van der Kruit, 1984, Dickey et al., 1990, Kamphuis, 1993, van Zee and Bryant, 1999, Petric and Rupen, 2007, Boomsma et al., 2008, Tamburro et al., 2009, Ianjamasimanana et al., 2015). Referring to Sect. 1.2, these values are significantly higher than those of the CNM ($\sigma_{\mathrm{CNM}} \sim$ 0.8 km s^{-1}), and larger or comparable to those of the WNM ($\sigma_{\mathrm{WNM}} \sim$ 8 km s^{-1}), calculated for an ISM dominated by thermal pressure.

Most authors are convinced that turbulent motions is at the origin of these high dispersion values. In the following, we give a brief theoretical background on turbulence.

1.3.1 Some theoretical notes on turbulence

It is difficult to find a general, common definition of "turbulence" in fluid-dynamics. In the book by Lesieur (2008), the author indicates as the first property of a turbulent flow its unpredictability. In concrete terms, this means that it is impossible a deterministic description of its evolution. Indeed, in turbulent flows, a small perturbation (e.g. provoked by the presence of an obstacle) will generally amplify causing instability. For this reason they are usually counterposed to laminar flows , where

the streamlines, if perturbed, reform downstream[1] (see Fig. 1.5).
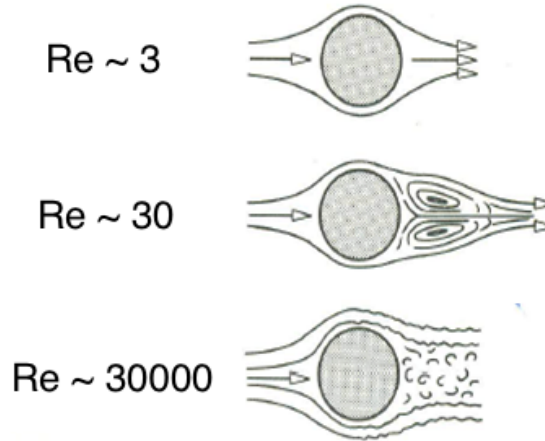
Figure 1.5: The behaviour of three different flow regimes while passing an obstacle. From top to bottom, the Reynolds number increases and the fluid passes from a laminar to a turbulent regime (readapted from A. F. Mills, "Heat Transfer", 2001).

From an operational point of view, it is common to define a quantity called "Reynolds number", to discriminate between these two types of flow:

$$Re \sim \frac{v\,l}{\nu} \tag{1.3}$$

where v is the fluid velocity, l a characteristic length of the fluid (e.g., considering the previous example: the linear dimension of the obstacle) and ν is the viscosity. We can qualitatively define the viscosity as the ability of the fluid to damp perturbations). In most cases, we can define a threshold Reynolds number above which the motion becomes turbulent (Fig. 1.5).

Since turbulence is not a deterministic phenomenon, it is very hard to get a theoretical description of it. Nevertheless, some of its basic properties are captured by the heuristic theory developed by Kolmogorov (1941) and Obukhov (1941). The theory is formulated under the hypothesis that turbulence is homogeneous, isotropic and fully developed in an incompressible flow (the density does not change with the flow). This means that the associated Reynolds numbers are very high. With this assumptions turbulence develops forming chaotic entities called eddies at

---

[1]Instabilities occour also in non-turbulent flows. In fact, under certain conditions, instabilities may lead to turbulence

a characteristic large scale L. These large eddies break apart forming eddies at smaller and smaller scales λ, transferring their kinetic energy from the largest to the smallest scales (the so called *"Kolmogorov cascade"*). This process continues down ti a scale λ_0 which is so small that the dissipation operated by viscosity cannot be neglected anymore.

In order to maintain a steady state system, the kinetic energy dissipated at the small scales has to be continuously supplied at the largest scales. It results that the kinetic energy of eddies of different scales follows a characteristic power-law distribution:

$$E_{kin}(k) \propto k^{-11/3}$$

where $k = 2\pi/\lambda$ is the wavenumber. For this reason, observations of power-law trends of the power spectrum in fluids are usually associated to turbulent processes. These kind of bahaviour has been observed in the ISM, as for example in the Large Magellanic Cloud (Elmegreen et al., 2001)

Of course this is a very idealized picture, especially if applied to the ISM. Indeed, the interstellar medium seems very far from realizing the assumptions required by the Kolmogorov-Obukhov theory (starting from that of incompressibility). However, it is particularly useful for its simplicity and to understand the fundamentals of turbulent flows. In particular, the central point of the Kolmogorov-Obukhov theory is the continuous feeding of turbulence at the large scales, because it is dissipated. If we believe that turbulent energy is responsible of the unexpected broadening of the HI line profiles in disk galaxies, we have to find a valid source of energy.

1.3.2   The feeding of turbulence

Several sources of energy have been proposed to drive the observed turbulence in the interstellar medium. The most popular is **stellar feedback**, which could provide energy through supernova (SN) explosions and powerful stellar winds from young and massive OB stars. Several papers suggest this as the main responsible for the feeding of disk turbulence. This may be corroborated by the fact that the gas velocity dispersion usually correlates with the star formation rate in galaxies. This has been observed in both nearby (e.g. Tamburro et al., 2009, Moiseev et al., 2015) and high-redshift galaxies (Green et al., 2010, Lehnert et al., 2013). Although it is very likely that star formation has a crucial role in driving the gaseous motions in the innermost regions of galaxies, the broadening of the line profiles in the disk

outskirts is more difficult to explain. The recent discovery of bright star forming regions at high distances from the galactic centres (e.g. Thilker et al., 2005, Gil de Paz et al., 2005) could give further support to this theory, even though the released energies would hardly be sufficient to explain the HI velocity dispersion.

Other mechanisms proposed invoke **galactic kinematics**. Indeed, turbulence could be generated by gravitational instability (Wada et al., 2002), spiral shock waves (Roberts, 1969), shear flows (Schaye (2004)), or gravitational potential energy of the arms (Elmegreen et al., 2003).

Some authors also considered the magnetic properties of the disks, suggesting that **magneto-rotational instability** in differentially rotating gas layers might produce a substantial amount of energy (Sellwood and Balbus, 1999, Tamburro et al., 2009).

Infall models have also been considered, referring with this to both galactic fountain (Bregman, 1980, but note that this phenomenon is still related to star formation), and to direct accretion of external intergalactic matter (e.g. Sancisi et al., 2008).

Further contributions could come from **thermal instability** (see for instance Hennebelle and Audit, 2007).

Despite the strong efforts made through theoretical, numerical and observational works, the final identification of the energy sources that can sustain turbulence and produce the broad HI-line profiles of the outermost regions of the disks, has not been reached yet.

To end of this section, we mention another point that we think should be considered. In the last years there has been growing evidence that the WNM dominates the outer regions of spiral galaxies, while the CNM is preferentially located in the inner disk (Pineda et al., 2013, Ianjamasimanana et al., 2015). Since the WNM dispersion is $\sim 8 \ \mathrm{km \ s^{-1}}$, it is legitimate to ask if the estimated filling factors for this component could be sufficient to generate the observed line widths. This could radically reduce the importance of turbulence in the outer galactic disks.

1.4 This thesis

The main aim of this thesis is to investigate the causes that produce the unexpected broad HI-line profiles in of disk galaxies. To give a contribute on this highly discussed topic, we performed a thorough study of two nearby spiral galaxies: NGC 6946 and M 101. In the choice of the galaxies we were guided especially by the very high quality of the data in our possess. In particular, the observations of M 101 that

we used are new Westerbork data never presented before.

In our study, we pursued the following strategy. First of all we searched for a precise and confident measure of the HI velocity dispersion. Since the definition of this quantity is subjected to some arbitrariness, in Chapt. 2 we compare the main methods normally used to estimate it, choosing the one that we think is more adequate. At the end of the Chapter, we show the total HI dispersion maps that we will use in the following Chapters.

The data analysis is divided in two Chapters. In Chapt. 3 we investigate relationships between the dispersion profiles and the spiral structure of the two galaxies. In particular, we define the arms and interarms, comparing the dispersion profiles obtained within them. In Chapt. 4 we look for pixel-by-pixel correlations between HI dispersion, column density and profile peak fluxes throughout the disk. A deep analysis is dedicated to understand whether the dispersion values exhibit significant differences between the arms and the interarms.

In Chapt. 5 we discuss our results, drawing a comparison between the two galaxies, and contextualizing them in the picture emerging from the literature. Moreover, we derive star formation rate density profiles of our galaxies, exploring their - global and local - correlations with the gas velocity dispersion. In particular, we estimate the turbulent kinetic energy input that could come from star formation processes, comparing it with a simple stellar-feedback driven turbulence model.

Chapter 2

Measuring the velocity dispersion

In the present Chapter we introduce the sample used in our study. Then, we describe the main challenges connected to the gas velocity dispersion measurement, and the chosen strategy to produce final dispersion maps.

2.1 The sample

Our study is limited to two nearby galaxies: NGC 6946 and M 101. Our present purpose, is to perform a very precise analysis of the HI velocity profiles, to investigate how their shape varies within a galaxy, and to define useful strategies for dispersion measurements. Our datasets were also chosen for their very high quality. Both galaxies were observed with the Westerbork Radio Synthesis Telescope (WSRT) at high spatial and velocity resolutions and with very long integration times (Tab. 2.2 and 2.4).
Finally, given their low inclination on the plane of the sky, both NGC 6946 and M 101 are very suitable for studies of the gas velocity dispersion.

2.1.1 NGC 6946

The main physical preperties of NGC 6946 are shown in Tab. 2.1, while in Tab. 2.2 we report the main characteristics of the observation. This dataset had already been analyzed in previous studies by Boomsma (2007) and Boomsma et al. (2008), even though their studies were focused on HI holes, high-velocity clouds and disk-halo connection, rather than on velocity dispersion. For our study we used the data reduced by Boomsma (2007).

Type		SAB(rs)cd	1
Distance	Mpc	6	2
Position of nucleus	$\alpha(2000)$	$20^h\ 34^m\ 52.3^s$	3
	$\delta(2000)$	$60°\ 09'\ 14''$	3
Kinematical centre	$\alpha(2000)$	$20^h\ 34^m\ 52.36^s \pm 0.13^s$	4
	$\delta(2000)$	$60°\ 09'\ 13'' \pm 2"$	4
Holmberg radius	arcmin	7.8	5
D_{25} [B mag arcsec^{-2}]	arcimin	11.2	5
Position angle		242°	4
Inclination angle		$38 \pm 2°$	4
V_{sys}	km s^{-1}	43 ± 3	4
M_B	mag	-21.38	5
L_B	$L_\odot$	5.3×10^{10}	5
HI mass	$M_\odot$	6.0×10^9	6 (*)
21-cm flux	Jy km s^{-1}	705.8	6 (*)
Conversion	kpc arcmin^{-1}	1.745	

Table 2.1: General information on NGC 6946. Notes - 1) de Vaucouleurs et al. (1976) 2) Karachentsev et al. (2000) 3) van Dyk et al. (1994) 4) Boomsma et al. (2008) 5) Carignan et al. (1990) 6) This study. (*) Slightly lower values than Boomsma et al. (2008) may come from different choices in eliminating the Milky Way emission, see Sect. 2.2.

Date of observation		Dec. 2001 - Jun.2002
Total observing time		16×12 h
Observed baselines		36-2772 m, step: 18 m
Field centre	α (2000)	$20^h\ 34^m\ 52.3^s$
	δ (2000)	$60°\ 09'\ 14''$
Heliocentric velocity of central channel	km s^{-1}	48
Total bandwidth	MHz	5 and 10 (*)
FWHM of primary beam	arcmin	36
Number of channels		512 and 1024 (*)
Channel separation	km s^{-1}	2.1
FWHM velocity resolution	km s^{-1}	4.2
Frequency taper		Hanning
FWHM of synthesised beam	arcsec	12×14
RMS noise per channel (no galaxy emission)	mJy beam^{-1}	0.22
RMS noise per channel (with galaxy emission)	mJy beam^{-1}	0.24
Conversion factor $T_B(K)/S(mJY)$		3.6

Table 2.2: Observing parameters for NGC 6946. (*) The first 8 observation have been done with 512 channels and 5 MHz bandwidth, the rest has been observed with 1024 channels and 10 MHz bandwith.

The spatial resolution of the datacubes is 12"×14". The data were Hanning smoothed, and the final velocity resolution is 4.2 km s^{-1}. We calculated the RMS of this observation using GIPSY (Groningen Image Processing SYistem, van der Hulst et al.

(1992), Vogelaar and Terlouw (2001)) task STAT: we averaged the background emission calculated on various channels without galaxy emission. We found $\text{RMS}_{\text{chan}} = 0.22$ mJy beam^{-1}. In the channels where the emission of the galaxy is present we measured (excluding NGC 6946 emission) a slightly higher value: $\text{RMS}_{\text{chan}} = 0.24$ mJy beam^{-1}. Boomsma et al. (2008) rounded at $\text{RMS}_{\text{chan}} = 0.2$ mJy beam^{-1}

Several other HI observations of this galaxy were taken in the past. In particular we mention the studies by Boulanger and Viallefond (1992) and Kamphuis (1993) who, using less resolved and more shallow data, performed also some measurements of HI velocity dispersion. Performing azimuthally averaged profiles, all these studies agree that dispersion is higher in the central regions of the galaxy and gradually decreases in the outskirts. Less agreement is present on the values, also because of the different resolutions of the observations (larger beam data are more affected by beam-smearing effects). In the highest resolution data (Boomsma et al., 2008) the dispersion spans from ~ 13 km s^{-1} in the very inner region, to ~ 6 km s^{-1} at 20 kpc (Fig. 5.1).

2.1.2 M101

M 101 is a giant spiral galaxy, its properties are summarized in Tab. 2.3. For the study of this galaxy we used new WSRT observations performed in March 2013 by Tom Oosterloo as Principal Investigator, who also performed the data reduction. This observation - a mosaic of five different pointings - are the deepest ever obtained for this galaxy at the 21-cm wavelength (Tab. 2.4).

The spatial resolution is 15.97"×13.19". Also in this case, data were Hanning smoothed giving a final velocity resolution of 8.24 km s^{-1}. In Fig. 2.1 we show the borders of the mosaic, superimposed to an optical image and the outer HI contour.

Due to the mosaic, the integration time and sensitivity varies across the field. As a consequence, the RMS per channel in M 101 has a radial dependence (increasing out from the centre of the field, see again Fig.2.1), and it also shows a slight variation between the first and latest channels. The plot in Fig. 2.2 displays the azimuthal profile of RMS for the first and the last channel of the datacube. For channel 1 it variates from 0.15-0.16 to 0.34 mJy beam^{-1}, while for channel 119 it grows from 0.17 in the centre of the picture to 0.35 mJy beam^{-1}. We note that M 101 emission lies in a central box smaller than the whole field (approximatively within ~ 1000" or ~ 29 kpc), were the noise is lower and flatter. We used channels from 1 to 10 and

Type		SAB(rs)cd	1
Adopted distance	Mpc	7	2 (^{a})
Position of nucleus	$\alpha(2000)$	14^h 03^m 12.6^s	2
	$\delta(2000)$	$54°$ $20''$ $56''$	2
Holmberg radius	arcmin	14	3
D_{25} [B mag arcsec^{-2}]	arcmin	16	4
Position angle		$40°$	5
Inclination angle		$18°$	6
V_{sys}		241 ± 2	1
M_B		-21.45	1
L_B	$L_{B,\odot}$	5.9×10^{10}	1
HI mass	$M_\odot$	2.84×10^{10}	7 (*)
21-cm flux	Jy km s^{-1}	2454	7 (*)
Conversion	kpc arcmin^{-1}	2	

Table 2.3: General information on M 101. Notes - 1) de Vaucouleurs et al. (1991) 2) Tully et al. (2013) 3) Holmberg (1958) 4)Mihos et al. (2013) 5) Kamphuis (1993) 6) Bosma et al. (1981) 7) This study. (*) Excluding the big HVC, see Par. 2.2. (^{a}) Distance of M 101 is still debated in the literature. The most of the estimates, with different methods, are around $\sim$7 kpc. That adopted by us is determined with Cepheids.

from 100 to 118, where there is no galactic emission, to build the map of the noise that we will use in the following studies (see Sect. 2.5). In the central region of the mosaic (inside R $\sim$ 29 kpc) we found an average RMS = 0.22 mJy beam^{-1}. In the same area, we also measured the RMS$_{chan}$ in the channels where the emission of the galaxy is present by selecting areas without galactic emission. We found a value of: RMS$_{chan}$ = 0.24 mJy beam^{-1}.

M 101 HI emission was also deeply studied in the past, but not particular focus was given to the velocity dispersion. Van der Hulst and Sancisi (1988) discovered a huge high-velocity cloud ($\sim$2$\times$10^8 M$_\odot$) over the north and east sides of the disk. High velocity clouds (recent reviews are Sancisi et al. (2008) and Wakker and Woerden (2013)) are gas complexes that appear at velocities very different from that of the normal rotation of the galactic plane (up to hundreds km s^{-1} different). Firstly discovered as a diffuse phenomenon in our Milky Way, they were later observed in nearby spiral galaxies, using deep radio observations. The one discovered by Van der Hulst and Sancisi (1988) was one of the first HVC observed in an external galaxy. In their paper they proposed also some explanations for its origin, ruling out some of them (supernova explosions), and discussing some alternatives (cloud-galaxy collision, tidal interaction with satellites, dynamical origins). The mystery of the origin of this cloud is still unsolved, though. In particular it has not been demonstrated

Date of observation		Mar. 2013
Total observing time		five 4 × 12 h
Field centre 1(*)	α (2000)	$14^h\ 03^m\ 12.0^s$
	δ (2000)	$54°\ 20'\ 6''$
Field centre 2(*)	α (2000)	$14^h\ 02^m\ 32.7^s$
	δ (2000)	$54°\ 11'\ 11.7''$
Field centre 3(*)	α (2000)	$14^h\ 02^m\ 04.9^s$
	δ (2000)	$54°\ 25'\ 13.4''$
Field centre 4(*)	α (2000)	$14^h\ 04^m\ 19.4^s$
	δ (2000)	$54°\ 26'\ 44.3''$
Field centre 5(*)	α (2000)	$14^h\ 03^m\ 51.7^s$
	δ (2000)	$54°\ 30'\ 47.5''$
Heliocentric velocity of central channel	km s^{-1}	292
Total bandwidth	MHz	10
FWHM of primary beam (one pointing)	arcmin	36
Number of channels		1024
Channel separation	km s^{-1}	4.12
FWHM velocity resolution	km s^{-1}	8.24
Frequency taper		Hanning
FWHM of synthesised beam	arcsec	13.19 × 15.97
Minimum RMS noise per channel (^{a})	mJy beam^{-1}	0.18
RMS noise per channel (^{b}) (empty channels)	mJy beam^{-1}	0.22
RMS noise per channel (^{b}) (galaxy channels)	mJy beam^{-1}	0.24
Conversion factor T_B/S	K/mJy	2.9

Table 2.4: Observing parameters for M 101. The final datacube is a mosaic obtained from five different pointings. (*) See Fig. 2.1. (^{a}) average for the channels without galaxy emission, calculated in the centre of the mosaic. (^{b}) average for R<1000" $\sim$ 29 kpc.

whether an interaction, even partial, between the cloud and the disk has happened or not. Some years later, Kamphuis (1993) investigated this high-velocity gas and provided a first mapping of the HI holes in this galaxy. He also performed a study of the velocity dispersion, providing an azimuthally averaged dispersion map, reported in Fig. 5.2 He concluded that the dispersion decreases from the inner (12 km s^{-1}) to the outer regions (8 km s^{-1}). He also claimed a higher average values in the arms than in the regions between them (12-15 km s^{-1} against 6 km s^{-1}). We will compare these results with ours in Sect. 5.1.

2.2   Preparing the datacubes

Both NGC 6946 and M 101 observations present some peculiarities that deserve to be discussed.
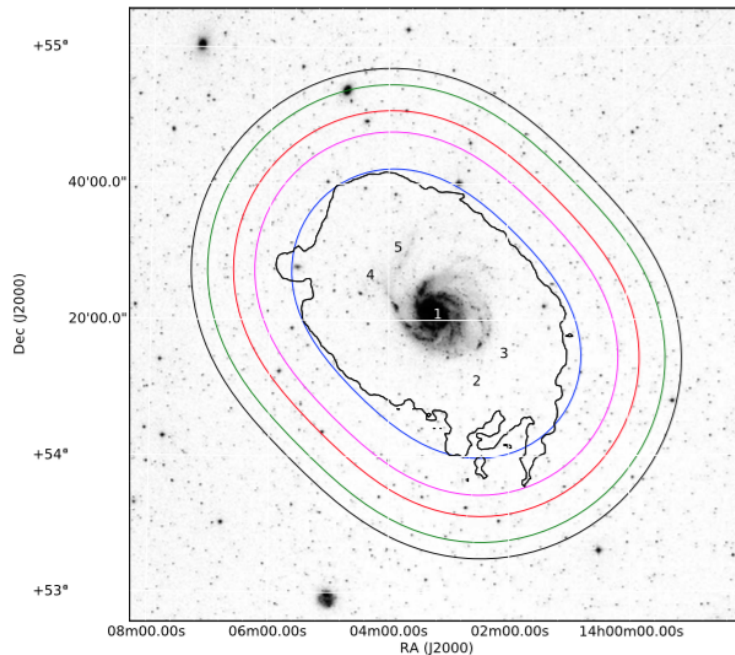
Figure 2.1: Optical image of M 101. The numbers are the centres of the HI observation pointings (see Tab.2.4). Blue to black contours are 0.5, 0.75, 1.0, 1.5 and 2.0 in units of the noise of a single 12-h observation (0.64 mJy/beam). The minimum noise per channel is 0.28, and we measured it at 0.18 mJy beam^{-1}. The outer black contour indicates also the total field of the mosaic (courtesy Tom Oosterloo).

2.2.1 Foreground emission from the Milky Way in NGC 6946 datacube

Between channel 33 (-62.5 km s^{-1}) and channel 47 (-3.6 km s^{-1}), the HI observation of NGC 6946 is affected by HI emission by our own Galaxy. Using GIPSY task PYBLOT we performed a manual clipping of this foreground Milky Way radiation. In some channels the spurious emission is easy to recognise and to exclude, while in channels number 41 (-28.8 km s^{-1}) to 44 (-16.2 km s^{-1}) included it is particularly difficult, for our Galaxy's emission is of comparable intensity, and sometimes superimposed to that of NGC 6946 (see Fig. 2.3).

2.2.2 High-velocity clouds in M 101 datacube

As already mentioned in Sect. 2.1, M 101 hosts a large High-Velocity Cloud, whose main complex lies north-east from the centre, extending with a long tail to the South and to the west (Fig. 2.4). It consists of extra-planar material, and covers
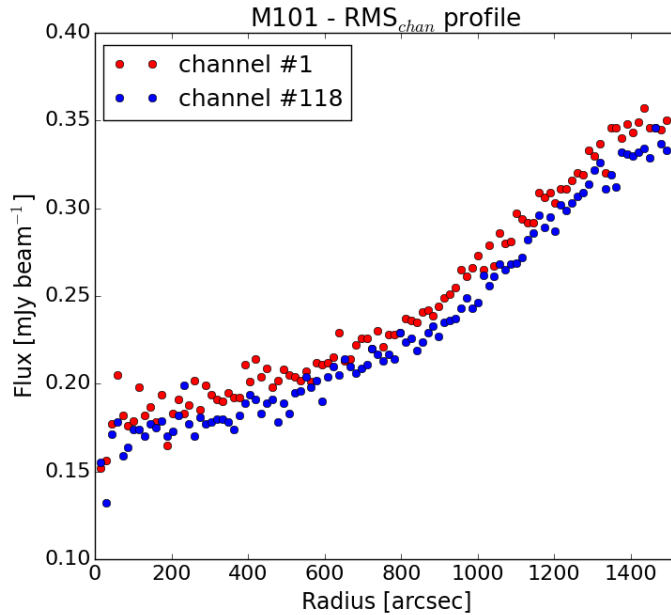
Figure 2.2: RMS azimuthal profile for two channels in the M101 dataset. Red points are relative to the first channel, while blue one to the last. It is evident that there is a shift between the two sequences, due to the frequency dependent sensitivity of the telescope. The inner 1000" ($\sim$ 29 kpc) ellipse - where the most of M 101 emission is - has an RMS below 0.25 mJy beam^{-1} with average values reported in Tab. 2.4.

about 15% of the total HI column density distribution and one third of the optical emission of the galaxy (Kamphuis, 1993).

In order to perform our study of the dispersion in the disk, we decided to use PY-BLOT to clip the HVC, because the cloud could give problems in the profiles fitting phase of our analysis. The automatic procedures to measure velocity dispersion (Sect. 2.3) indeed, could have been influenced by the relative peaks produced by the HVC, as we verified by inspecting a certain number of individual profiles by eye.

In our very high resolution data, the HVC emission is visible in correspondence of its main structures, that are the N-E main complex, and the final elongation of the southern tail (see Fig. 2.4). Using position-velocity plots like those in Fig. 2.5 (where we performed a smoothing of the datacube to lower resolutions to enhance the emission of the cloud), it is easier to distinguish the cloud's emission from that of the galaxy. Indeed, the HVC emits at higher velocities than the galaxy, being usually separated by some channels with no emission (Fig. 2.5(b)). There is just a problematic area, which lies where the main complex is, that in position-velocity plots appears to have a continuity with M 101 (Fig. 2.5(c)). This is very interesting,
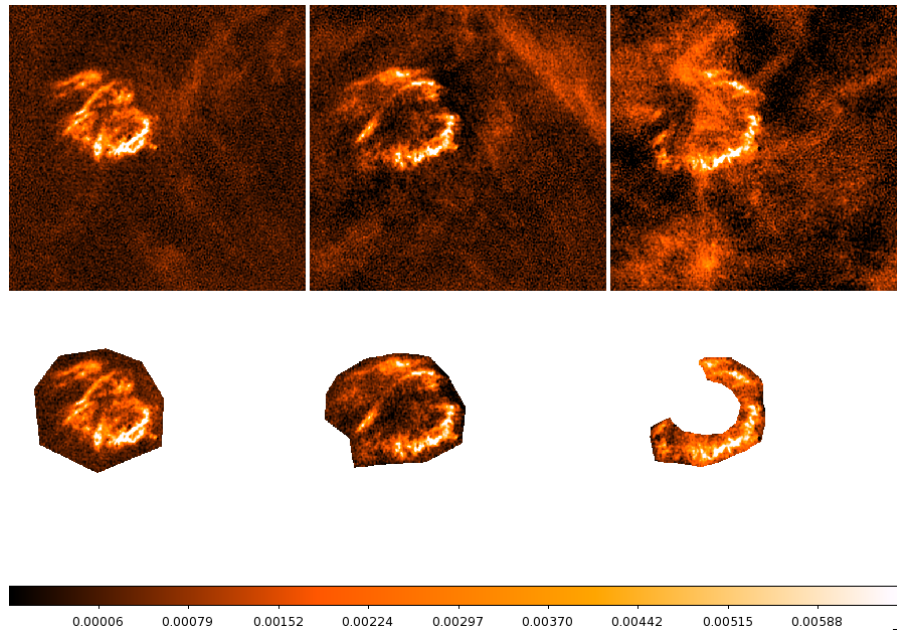
Figure 2.3: Top: Channels number 38 (-41.4 km s^{-1}), 41 (-28.8 km s^{-1}), 43 (-20.4 km s^{-1}) in NGC 6946 datacube. Milky Way foreground emission is clearly visible as large dffuse "clouds" stretching throughout the field. While in several channels it is easily distinguishable from the proper NGC 6946 component, for channels between 41 and 45 this is not straightforward. Colour scale is in Jy beam^{-1}. Bottom: the corresponding masks we built with GIPSY's PYBLOT.
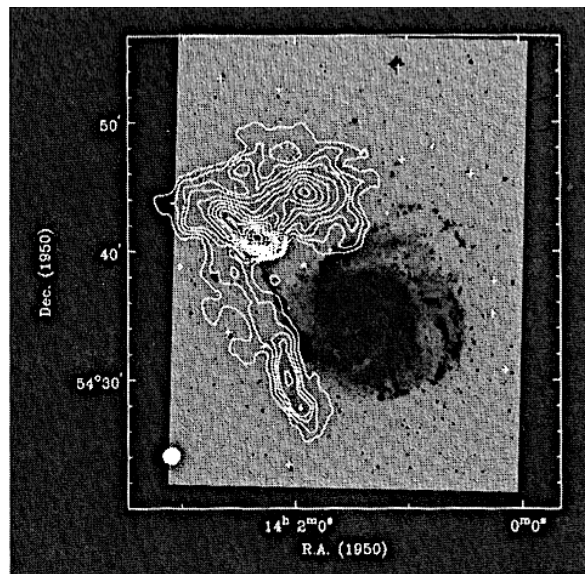
Figure 2.4: A picture from Kamphuis (1993) PhD Thesis: the huge HVC, superimposed on an optical image of M 101. Contour levels indicate HI column density, and they are 0.7, 1.4, 2.1, 2.8 10^{19} cm^{-2}, and 4.3 to 17.0 10^{19} cm^{-2} in steps of 1.4 10^{19} cm^{-2}.

because it could be interpreted as an interaction between the cloud and the galaxy. However, it also makes difficult it to decide, in that area, where emission from M 101 ends and the HVC starts. Looking at P-V plots as that showed in Fig. 2.5, we decided to consider the emission at v > 368.3 km s^{-1} as part of the Cloud's main complex.

(a)

(b)

(c)
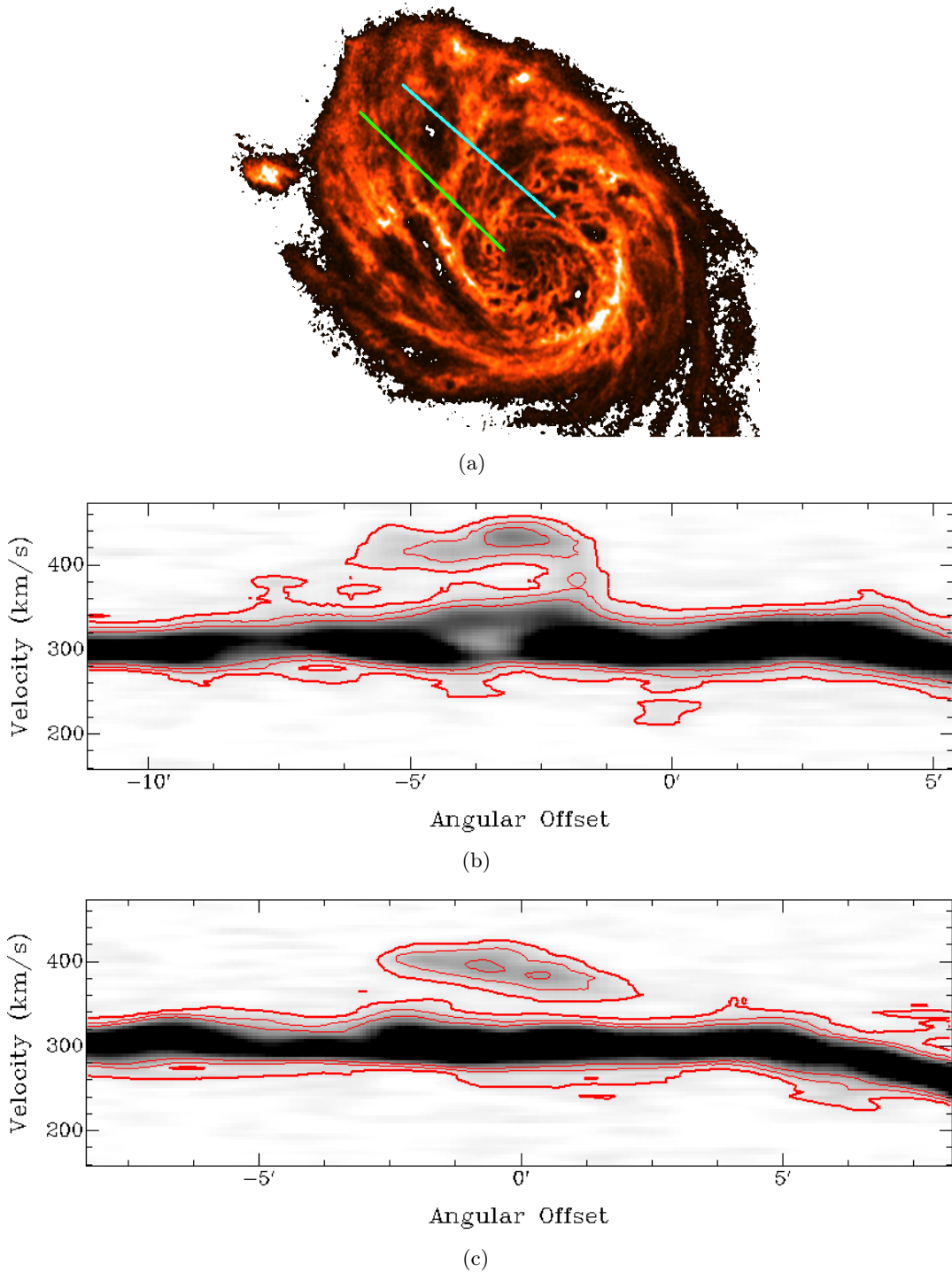
Figure 2.5: Position-velocity diagrams showing the HVC in M 101. They were obtained from a datacube smoothed to $50''$ resolution to enhance the cloud's emission. (a) HI column density map with the cuts superimposed. (b) Cut correspondent to the green line in (a). It is taken from α (14^h 04^m 43.6^s), δ ($54°$ 32^m 53.6^s) to α (14^h 03^m 22.5^s), δ ($54°$ 21^m 40.0^s). A "chimney" feature, which extends up to ~ 450 km s^{-1} is clearly visible in the middle of the picture. (c) Cut correspondent to the cyan line in (a). It is taken from α (14^h 04^m 20.0^s), δ ($54°$ 35^m 7.1^s) to α (14^h 02^m 54.1^s), δ ($54°$ 24^m 23.7^s). The HVC in this case lies completely separated from the galaxy. Both Fig. (b) and (c) contour levels are 20, 50, 90 mJy beam^{-1} ($3\sigma = 20$ mJy beam^{-1} at this resolution).

2.3   Methods to estimate the velocity dispersion

The first challenge of our work was to obtain reliable velocity dispersion maps. Here we briefly describe the two main methods used to obtain a dispersion measurement from line profiles.

2.3.1   Second moment

Moments are a useful tool to characterize the properties of a distribution.
The k-th moment of a distribution $\phi(x)$, about a value x_0 is defined as:

$$\mu_k = \int_{-\infty}^{+\infty} (x - x_0)^k \phi(x) dx \tag{2.1}$$

First order moments have a clear physical meaning: the 0-th moment of $\phi(x)$ is the integral under the curve, while the 1-st moment is the weighted mean, and the 2-nd moment is proportional to the dispersion of the distribution. Eq. (2.2) is the **variance** of a distribution, that is the 2-nd order moment about the mean value of the distribution, normalized on the total flux under the curve (i.e. the 0-th moment):

$$var = \frac{\int_{-\infty}^{\infty} (x - <x>)^2 \phi(x) dx}{\int_{-\infty}^{\infty} \phi(x) dx} \tag{2.2}$$

The square root of this value can be a good estimate of the dispersion of the distribution. However, it is important to pay attention not to include the noise in the calculation, for it can deeply influence the variance value, especially for low density profiles. We discuss these implications in Sect. 2.6.

2.3.2   Fitting profiles

A more direct way to measure a profile velocity dispersion is through the fitting of the profile with a theoretical distribution. Since our goal is to measure the random motions of the gas, the most natural choice is for a single-peaked normal distribution. As we will see in Sect. 2.4, HI velocity profiles are not perfectly Gaussian, so there could be other distributions which better fits the observed curve (e.g. Gauss-Hermite distributions, see e.q. van der Marel and Franx (1993)).
Another possibility is to fit multiple Gauss components. However, despite in many cases this would give a more precise fit of the profile, it is not trivial to obtain the velocity dispersion information from these fits. Some studies use double Gaussian

fits to determine the width of the broad, warm gas component and of the cold and narrow one (Ianjamasimanana et al. (2012), Ianjamasimanana et al. (2015)). In that way one would distinguish between the two components that should compose the HI layer of disk galaxies (see Sect. 1.1). In our opinion the double Gaussian fitting does not have such a straight-forward interpretation. Indeed, in principle there is not just one possible convolution of two normal distributions that can well interpolate the observed line profiles. Different couples of Gaussians, of different widths, can produce fits of comparable goodness. For instance, it is not considered the possibility that HI gas could be composed not just of two components (the thermally stable phases CNM and WNM) but of a wider range of phases. Temperatures between that of CNM and WNM are known to be unstable, but they are diffusely observed in the ISM (Sect. 1.3). Double Gaussian fits would correctly reproduce such profiles made of multiple ISM components. Then, to include also this possibility, of particular importance in our study, we decided to perform single gaussian fitting on our data.

From single Gaussian fitting it is possible to measure the **Full Width Half Maximum (FWHM)**. Considering a Gauss function centred in x_0:

$$f(x) = Ae^{-(\frac{x}{\sqrt{2}\sigma})^2} \tag{2.3}$$

where A is the peak amplitude and σ the dispersion, we can find the width at a certain height α as:

$$Ae^{-(\frac{x_\alpha}{\sqrt{2}\sigma})^2} = \alpha A$$

$$x_\alpha^2 = -2\sigma^2 \ln \alpha$$

To calculate the FWHM is then immediate ($\alpha = 0.5$):

$$\text{FWHM} = 2x_{\alpha=0.5} = 2\sigma\sqrt{2ln2} \sim 2.355\sigma$$

Conversely, from the FWHM, the dispersion of the Gaussian is then calculated as:

$$\sigma = \frac{1}{2.355}\text{FWHM} \tag{2.4}$$

2.4   Type of profiles

To understand which of the two just defined methods is the most suitable to obtain a good dispersion measure, it is of primary importance to inspect the shapes

of the line profiles in our galaxies.

We can define three main types of profiles, present in both our galaxies:

- **nearly Gaussian profiles** (Fig. 2.6), i.e. profiles that presents an apparently Gaussian shape. Most of the line profiles are indeed of this shape. We discuss later in this Section the challenges connected in estimating dispersion from these profiles;

- **asymmetric profiles** (Fig. 2.7(a)), i.e profiles with a single peak, but without a Gaussian shape, usually characterized by a long and highly one-sided tail;

- **double-peaked profiles** (Fig. 2.7(b)), i.e. profiles (either Gaussian or not) with two separated peaks.
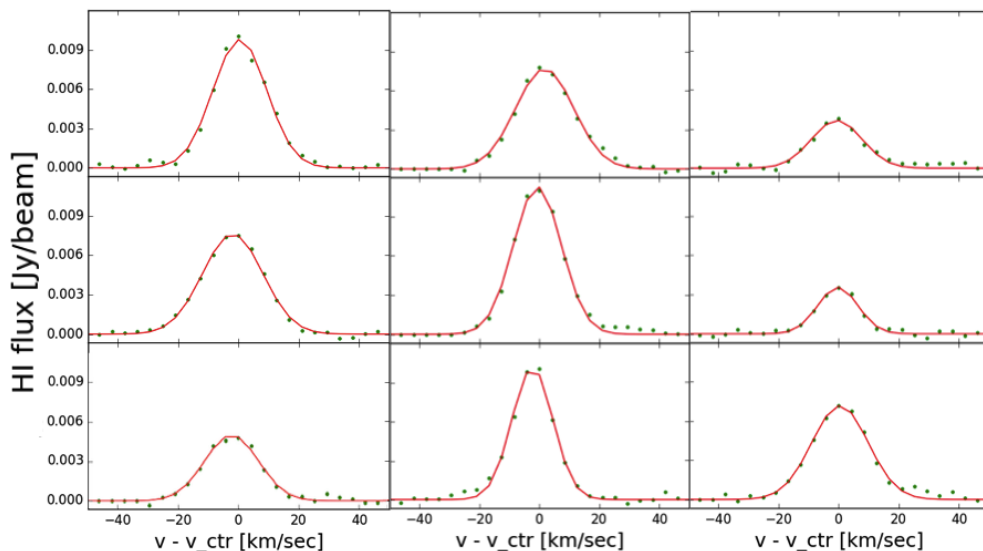
Figure 2.6: Some profiles of NGC 6946. Most of the profiles in our data are this shape, which can be approximatively well described by a single Gauss fit (red curve).

When we measure the dispersion of the asymmetrical and the double-peaked profiles using the methods described in Sect.2.3, we obtain values among the highest in the whole datasets. Thus, it is of capital importance to discuss whether to include them or not in a study of turbulence-generated profiles. This kind of profiles are usually found near HI holes. These are generally related to Supernova explosions and to the expansion of the remnant through the ISM. Then, gas surrounding the holes is usually subjected to motions that tend to be ordered in a preferential direction (that of the expansion). When two components of the expansion, or one of the expansion
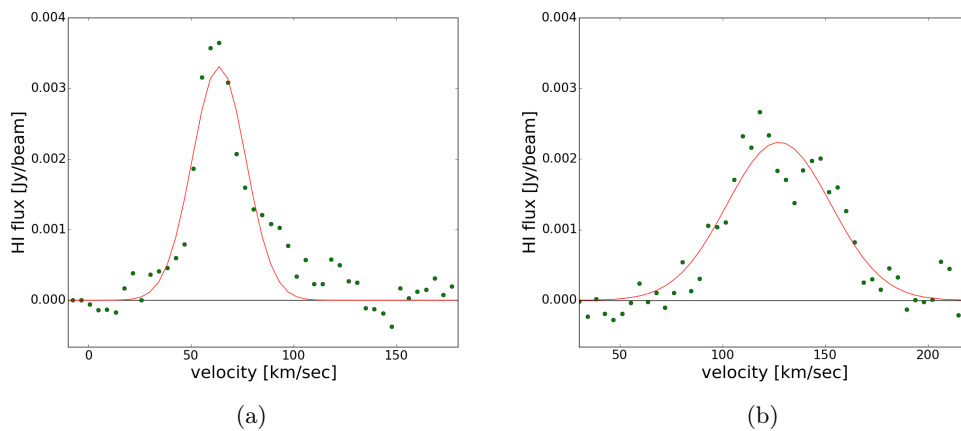
Figure 2.7: (a) An asymmetric peak taken from NGC 6946 datacube. The superimposed Gauss fit (red curve) does not reproduce the full profile. (b) Typical double horn feature. The fitting procedure interprets the profile as a very wide single peak: including profiles of this sort in a statistical study of the dispersion can change our results.

and one of the unperturbed ISM end up in the same beam, one observes double peaks. As a consequence, we think that double peaks are located in regions where gas is not dominated by random motions, but rather by temporary ordered ones.

In the following we identify the double peaks and exclude them from our study. In a picture of a feedback generated turbulence, this could sound strange, since superbubbles evolution should be one of the main sources of turbulent motions. Although, what we aim to study is a "developed" turbulence that should establish in a second moment, when superbubbles-induced gas motions have become of random nature (cfr. Sect. 1.3). For what concerns asymmetric profiles, since they are often found near HI holes, they could be of the same nature of the double peaks, but the spatial resolution of the telescope could be not good enough to separate them. Another possible origin of asymmetric profiles could lie in extraplanar gas (neutral hydrogen located in the galactic halos, see for instance Oosterloo et al. (2007)). In this case we are not referring in particular to High Velocity Clouds, while to gas at slightly different velocities from the normal rotation of the galactic disk. Features like these - that are known to be common in NGC 6946(Boomsma et al., 2008) - can produce profiles with very broad wings.

2.5   Selecting "bad" profiles

Once we have decided to clip double-peaked and asymmetrical profiles, in the present section we describe the criteria chosen to individuate them.

2.5.1   Double peaks

To find double-horns we started performing a single-peak Gaussian fitting of the velocity profiles, using GIPSY's task XGAUFIT, which performs an automatic fit of the whole datacubes. One of the task's output is the reduced chi-square (χ^2). Since a single Gauss fit of a double-horn profile is by definition a bad fit, we expected these profiles to be those with highest χ^2 (see for instance previous Fig. 2.7(b)).
The χ^2 calculated by XGAUFIT is defined as:

$$\chi^2 = \frac{(x- <x>)^2}{d.o.f} \tag{2.5}$$

where $<x>$ is the mean value of the variable (in our case, measured flux for each channel), while $d.o.f.$ are the degrees of freedom of the observation (in our case the number of data in each profile). We further normalized Eq. 2.5 to the $\mathrm{RMS_{chan}}$ value of the dataset. In this way we obtained values roughly comparable to unity. For NGC 6946 we used the $\mathrm{RMS_{chan}}$ value measured for the channels without galactic emission (Tab. 2.2). Since the noise is flat in this datacube, we judged it was fine to use a constant value for the normalization. The observations of M 101 are instead obtained with multiple pointing, then the noise depends on the position in the image (see Sect. 2.1). We built a noise map for this datacube, to obtain the RMS value characteristic for every pixel. We used the channels without galactic emission, to be consistent with the procedure used for NGC 6946, so the noise map was produced using channels 1 to 10 and 100 to 118. Finally, we divided the χ^2 map for the noise map.
We then had to find a χ^2 value which discriminates from good to bad profiles. To do this we performed a thorough inspection of a significant number of profiles, using GIPSY task XGAUPROF, which allows us to visualize single profiles with superimposed fits. We also used position-velocity (p-v) diagrams to visually inspect the galaxy regions in correspondence to the studied profiles. This was especially useful to check if the double-peak profile corresponds to a HI hole, which we considered a further indication that we were in proximity of a perturbed environment.

The visualization of a handful of profiles made us understand that a constant χ^2 value, fixed for each peak flux, was not suitable for our goal. Indeed, profiles with high density peak have systematically higher χ^2 values than low signal to noise ratio (S/N) peaks. So, for example, a fixed χ^2 value which seemed good for high S/N non-Gaussian profiles, resulted too tolerant for low S/N profiles. For them indeed, the sum of just a few residuals could be sufficient to deviate from a Gaussian shape. For this reason we look for a correlation between peaks ampitude and the maximum acceptable χ^2 for a profile of that amplitude. So, in general, calling y the reduced χ^2 (always weighted on $\mathrm{RMS_{chan}}$ value), and x the maximum amplitude of the profile, the profile was recognised as "bad" and clipped if:

$$y > \alpha x + \beta \tag{2.6}$$

To find α and β (the parameters of the linear correlation) a careful visual inspection of lots of profiles was needed.
For both NGC 6946 and M 101 we adopted the parameters:

$$\alpha = 50$$

$$\beta = 1.46$$

Obviously with this criterion not just double-horn profiles are selected, but also those which deeply deviate from a Gauss shape, like for example profiles with very broad wings, either both or one sided, and with very low S/N (usually present in the galaxy outskirts).
However, although not all the profiles with high χ^2 are double-peaked, we found that nearly all the double-peaked profiles have high χ^2.

Let us now briefly discuss the masks produced using the criterion just described. In Fig. 2.10(a) we show the mask obtained for NGC 6946. In the north side of the picture, we notice some correlation between the high χ^2 profile positions and the channels that we masked to eliminate Milky Way foreground emission (see Sect. 2.2). Many of the remaining blank values are found in correspondence of HI holes.
In Fig. 2.10(b) is shown the mask produced for M 101. Many more blank values are visible, compared to NGC 6946 map. This is related to the different procedure adopted: for NGC 6946 we normalized the χ^2 on a constant RMS value, while for M 101 we used the noise map, which could present some fluctuations due to the random

nature of noise. In the inner galaxy, three main clipped regions are visible. The one N-E to the centre appears correlated with the HVC main complex and tail (Sect. 2.1). We think this is interesting: since we have clipped it from the cube (Sect. 2.2), in principle we would not have expected to find non-Gaussian profiles in this region. The fact that we find them may be the indication that the HVC has in fact interacted with the disk gas. Diametrically opposed to the centre - on S-W side - another high-χ^2 region is individuated. This lies in correspondence of a peculiar feature of M 101 HI disk. Already Kamphuis (1993) noticed in that region an unexpected slope changing in the rotation curve of the galaxy, which is particularly evident in the p-v plot showed in Fig. 2.8 at $+1'$ angular offset. They sustained that a possible origin could be a tidal interaction with a companion (likely NGC 5474, which lies 90 kpc - projected - south of M 101's centre). Another possibility is that it shares a common origin with the HVC. A further indication of that could be the fact that these two features are symmetrically displaced with respect to the centre.This hypothesis then, sounds particularly intriguing.

The last main blank region in Fig. 2.10(b) is located N-W of the centre, and it corresponds to a bright HI arm. A visual inspection with XGAUPROF showed that line profiles in that area present particularly asymmetric shapes, with broad wings. We think this is due to shear flows present in that region. This should be evident looking at Fig. 2.9, where we show the high χ^2 values we are discussing, superimposed on the measured velocity field of M 101. In that region a sudden change in the direction of the iso-velocity contour is evident. Features like these are likely due to shear flows in the ISM of a galaxy.

2.5.2   Asymmetric profiles

Even though the just defined "χ^2" criterion is good in finding also some asymmetric profiles, not all of them are identified in this way. A good way to measure the deviations from a Gaussian shape of a distribution is calculating the **skewness** of a single peak Gauss-Hermite (h3) fitting of the profiles.

For any distribution $\phi(x)$, its skewness is defined:

$$\xi = \frac{1}{\mu_0} \int_{-\infty}^{\infty} \left(\frac{x - x_0}{\sigma}\right)^3 \phi(x) dx \tag{2.7}$$

As the dispersion of a distribution is proportional to its 2-nd moment, the **skewness** is proportional to its 3-rd moment. Skewness is an indicator of the asymmetry of

(a)

(b)
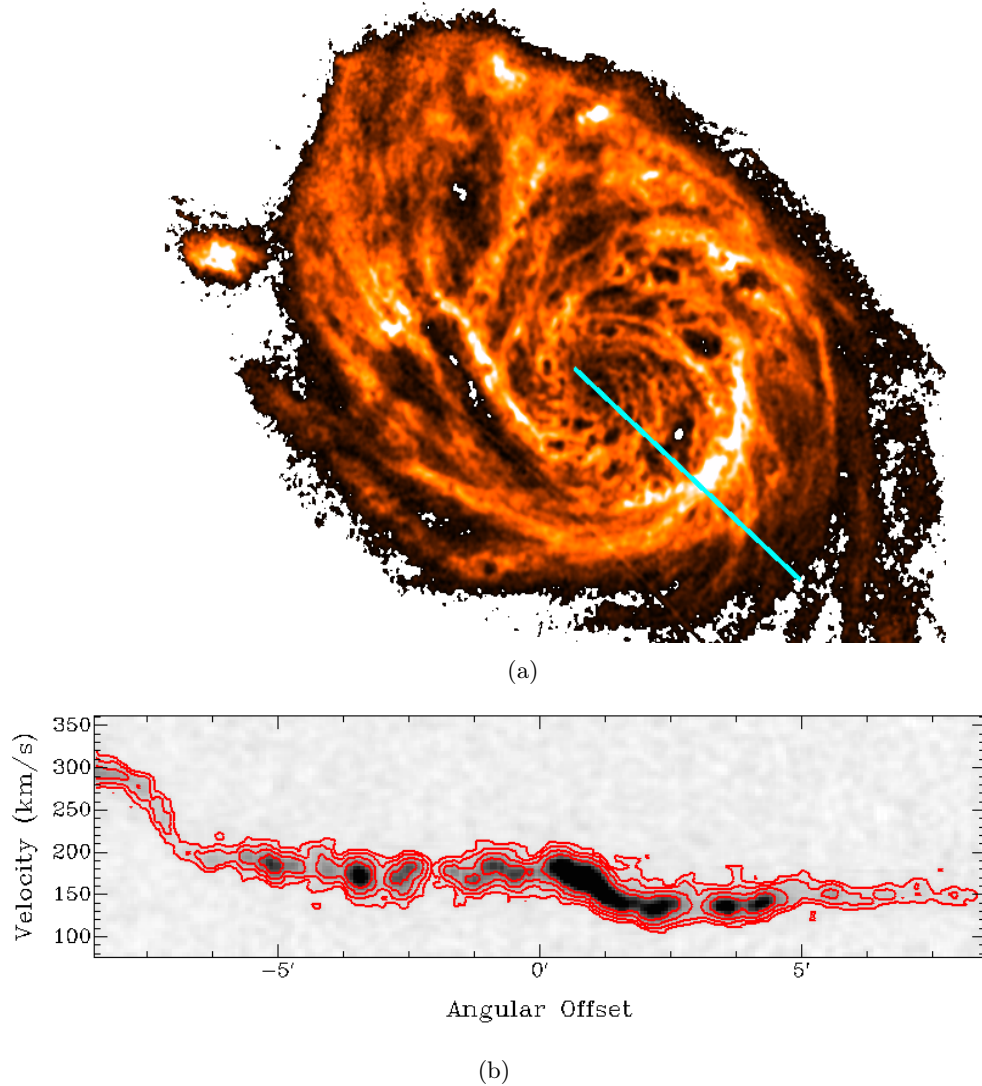
Figure 2.8: Position-velocity plot of M 101, showing the disk velocity change S-W to the centre. (a) HI column density map of M 101 with the cut superimposed. (b) The correspondent P-V plot. The precise coordinates are: α (14^h 03^m 21.1^s), δ ($54°$ 21^m 45.0^s) to α (14^h 01^m 56.4^s), δ ($54°$ 10^m 9.0^s). Red contours are 0.66 mJy beam^{-1} (3σ), 1.32, 2.64 and 5.28 mJy beam^{-1}. From 0' to 2' of Angular Offset an unexpected change in the disk mean velocity is visible. The greater velocity change at $\sim$ 6'-7' is relative to the galactic centre.

a distribution. In practice: the higher it is (either negative or positive), the higher is the asymmetry. For its properties then, skewness is a particularly useful tool to find profiles with tails on one side. Since the skewness of a normal distribution is by definition zero, to estimate deviations from Gaussianity one usually uses a fit with a
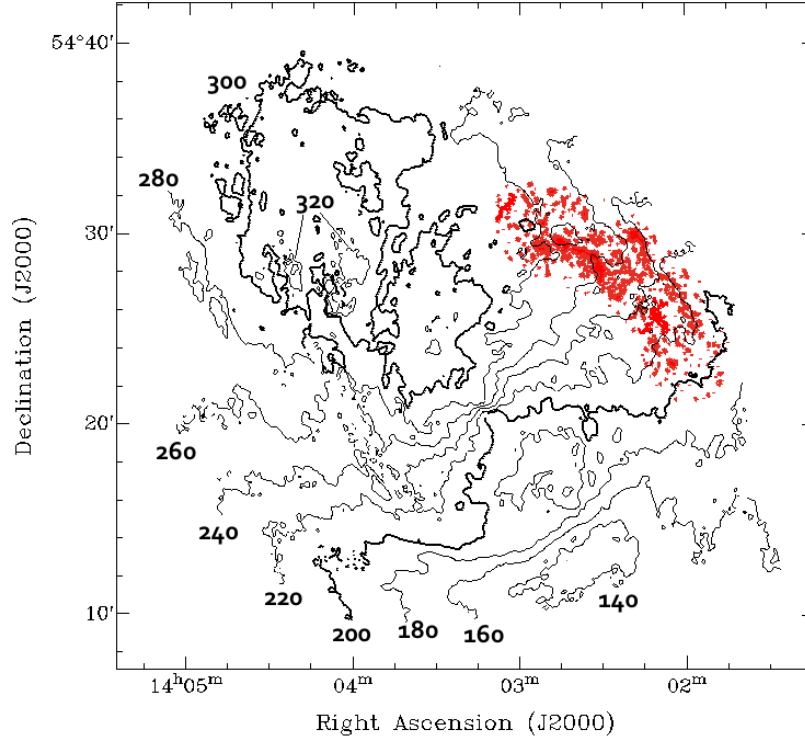
Figure 2.9: Velocity field measured for M 101: heliocentric velocities projected on the line of sight are indicated. The red spots N-W from the centre indicate the $\chi^2 > 2$ values that are present in the region of one of the main spiral arms of the galaxy. In the same region a change in the iso-velocity pattern, likely due to shear flows, is visible.

Gauss-Hermite (h3) distribution. This is defined as:

$$\phi(x) = ae^{-\frac{y^2}{2}}\left[1 + \frac{h_3}{\sqrt{6}}(2\sqrt{2}y^3 - 3\sqrt{2}y)\right]$$

where h$_3$ is the Gauss-Hermite distribution parameter, and $y = \frac{x-b}{c}$. The parameters a, b and c they reduce to be, respectively, the A, x_0 (mean) and σ of a standard Gaussian.

After obtaining the skewness map, we performed a visual inspection (with XGAUPROF and pv-plots, as for the double-peak candidates) of many high skewness profiles, to define a ξ value which discriminates from good to asymmetric profiles. We decided that the value:

$$|\xi| = 1.2$$

was a good compromise to select these profiles. We judged that a constant skewness value was sufficient to find the asymmetric profiles which had not already been selected by the χ^2 criterion.

In Fig. 2.11 we show the masks obtained with this method. Looking at the map produced for M 101 (Fig. 2.11(b)), we think it is remarkable that many "blank" values are in correspondence of the region where the HVC lies (we remind that its emission has been completely eliminated). Differently from the high-χ^2 map (Fig. 2.10(b)), here the clipped values are also in correspondence of the HVC "tail" (see Fig. 2.4), and not only in proximity of the "main complex". As seen for the χ^2 mask, to find strong deviations from a Gaussian shape of the profiles in this area is very interesting. Indeed, it could be a signature that we are in presence of a perturbed environment, maybe by interactions between the cloud and the galaxy.
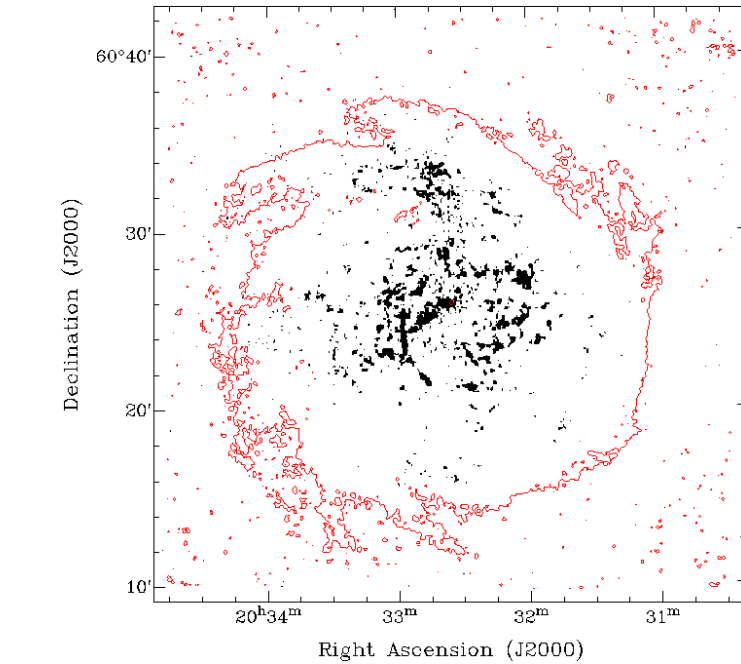
(a) NGC 6946.
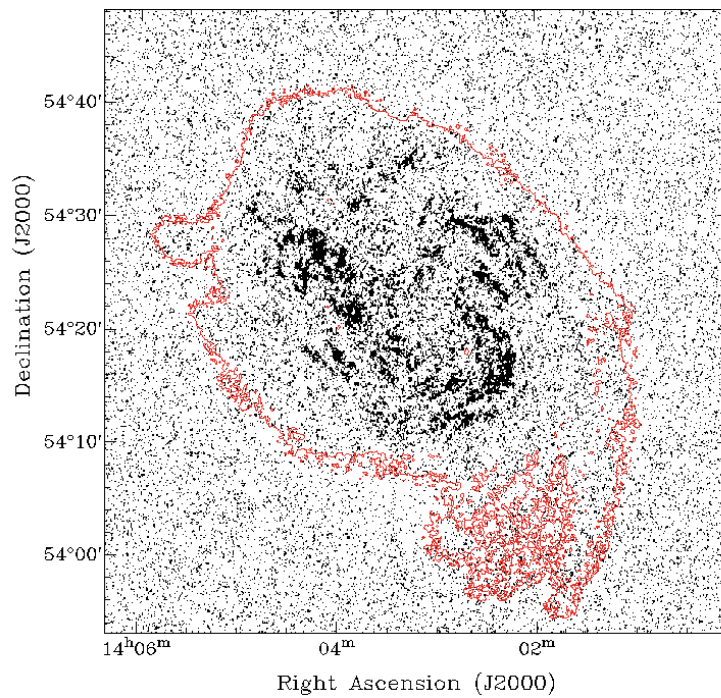
(b) M 101.

Figure 2.10: The high χ^2 maps used as masks in our study. Blank values (black) are in correspondence of the "bad" profiles. Red contours are at $5 \times 10^{19} cm^{-2}$. In (a) there is a tiny correlation visible between clipped profiles and emission from the Milky Way foreground (in the north side, see Fig. 2.3). Many of the other blanks are located near HI holes. In (b) we can observe many blank values in correspondence to the HVC cloud, even though it was excluded during the fitting procedure. The other blank locations are discussed in the text.
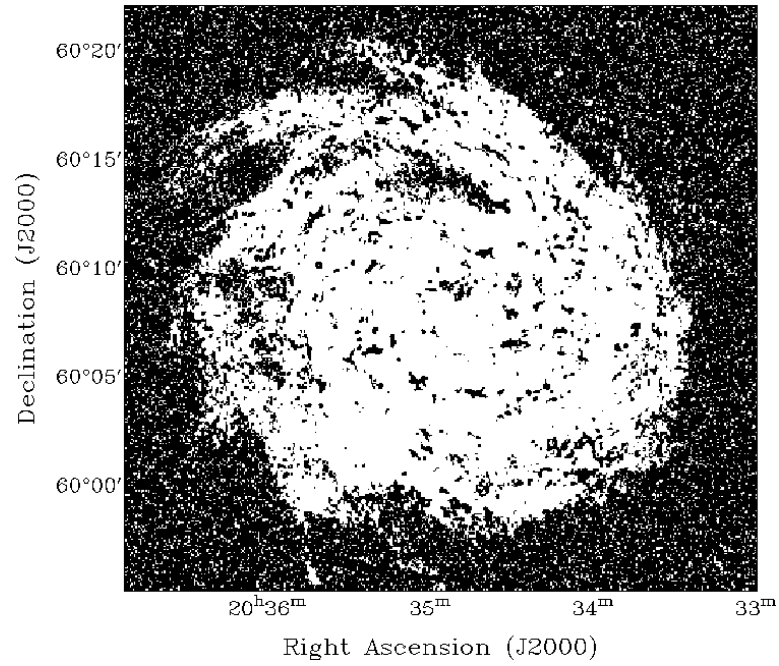
(a) NGC 6946.
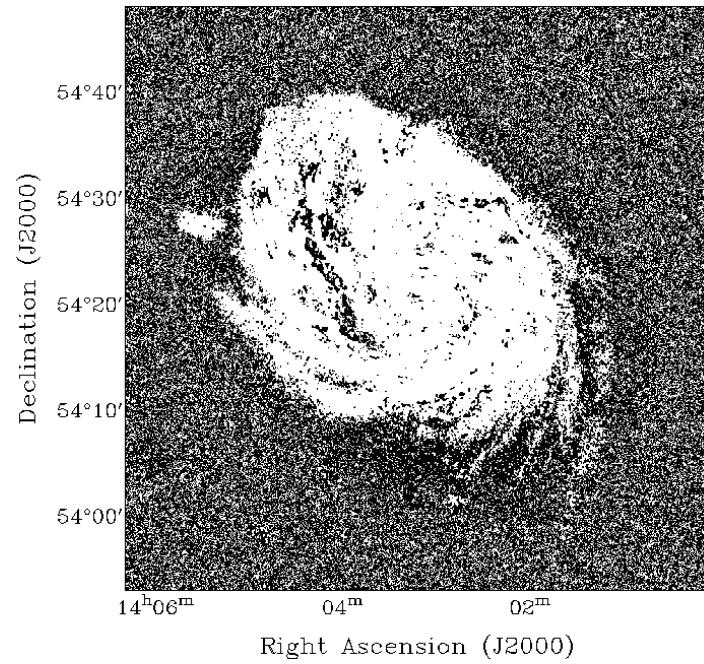
(b) M 101.

Figure 2.11: The high skewness maps used as masks in our study. Blank values (black) correspond to the $|\xi|>1.2$ profiles. Also in this case in (b) an increment in blank values is visible in correspondence of the HVC, even though this was excluded during the fitting procedure (see discussion in the text).

2.6 Velocity dispersion maps

Once we had both the double-horn and the high skewness masks, the last step was to calculate the HI velocity dispersion of the remaining profiles. As described in previous Sect. 2.3, there are mainly two possible methods to use.

The first we tried was to fit the profiles with a theoretical curve, running XGAU-FIT on the datacubes. The fitting function was set as a single Gauss function, with amplitude filter at 3RMS, to exclude profiles with low S/N. The fitting parameters (amplitude, centre, dispersion) were left free, while the background term was fixed to zero (as default in XGAUFIT).

One of XGAUFIT outputs is the velocity dispersion map of the datacube. We then combined those maps, obtained for both NGC 6946 and M 101, with the "bad" profiles maps described in Sect. 2.5 and shown in Fig. 2.10 and 2.11. The resulting map should contain just profiles that should be approximatively well fitted by a single Gaussian. Then, these maps should hypothetically represent the areas of the galaxies with profiles produced by both thermally broadening and fully developed turbulence (see Sect. 1.3.1).

Obviously this is an ideal picture: a visual inspection of many non-masked profiles, as the p-v plots of some regions of the galaxies, revealed that in certain areas non Gaussian profiles were still present. In NGC 6946, these areas are expecially those in correspondence to the Milky Way influenced channels, while in M 101 most of them are again near the HVC area. Every conclusion that we will give relatively to these regions will be given consciously of these problems.

Another common problem we noticed during this kind of procedure, was that some fit could not reach the peak of the profile (see for example Fig. 2.12). This reflects the fact that also these profiles are not precisely Gauss-shaped. In particular, profiles like these, usually present anomalous tails, even though not so big to reject them. These profilese could be successfully fit with a broad and a narrow Gaussian functions. However, as mentioned, the interpretation of these two components is not straightforward, and it is very difficult to automatize. Moreover, we would have to decide which of the two Gaussian should be representative of the local dispersion. For all these reasons we prefer to fit a single Gaussian also in these cases.

In Fig. 2.14(a) and Fig. 2.15(a) we report the two final velocity dispersion maps obtained with the "Gaussian fitting method" for NGC 6946 and M 101.

We then tried to measure the dispersion calculating the second moment, now
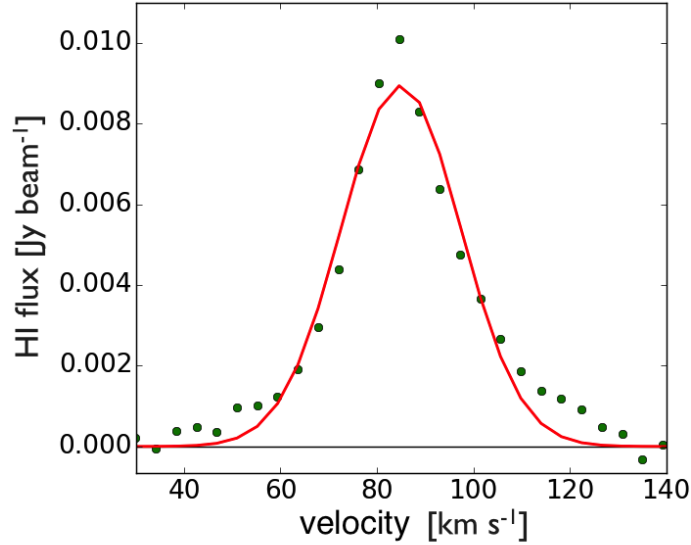
Figure 2.12: A sample profile from NGC 6946 datacube. Profiles like this are considered approximatively Gaussian even though the fit with a normal function (red curve) shows deviation from a Gaussian shape, in the tails and in the peak.

using GIPSY task MOMENTS. This method is heavily dependent on the parameter choices used. In particular MOMENTS allows the user to choose a RANGE over which to perform the moment calculation (we chose from 3σ to infinity as for the Gaussian fitting). Another parameter is WINDOW: even if an amplitude value is within the range, it is considered in the moment calculation only if it is surrounded by a number of channels (with amplitude within the range) grater or equal to the number chosen in WINDOW. This is a useful method to eliminate spurious profiles. After having tried many possibilities, we found that WINDOW = 3 was the most suitable way to calculate second moment in our data.

The second moment maps obtained after multiplication with the masks (Sect. 2.5) are shown in Fig. 2.14(b) and Fig. 2.15(b).

2.6.1   Comparing the methods

By looking at the maps in Fig. 2.14 and Fig. 2.15, we can outline some significant differences. In general the second moment maps give systematically lower values than the Gaussian fit maps. A deeper insight shows also that some high dispersion areas (in the XGAUFIT produced map) correspond to very low values in the MOMENTS generated maps. For NGC 6946 this is particularly evident in the outer disk. Superimposing HI column density maps, we noticed that usually these regions
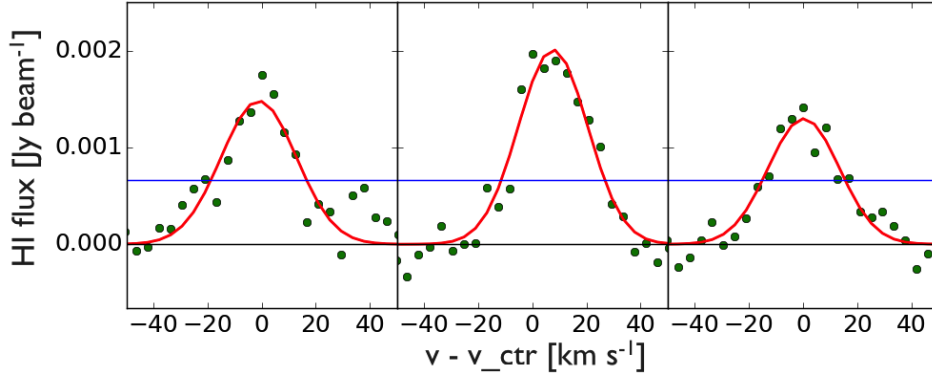
Figure 2.13: Three sample low S/N profiles with Gaussian fits superimposed (red curves). For profiles of this kind second moment calculation and Gauss fitting gave two very different values. In these profiles, from left to right: σ_{XGAU}=13.69 km s^{-1} vs $\sigma_{2^{nd}MOM}$=7.35 km s^{-1}; σ_{XGAU}=12.65 km s^{-1} vs $\sigma_{2^{nd}MOM}$=8.84 km s^{-1}; σ_{XGAU}=13.04 km s^{-1} vs $\sigma_{2^{nd}MOM}$=8.47 km s^{-1}. Excluding values below 3σ (the blue line) in the Gaussian fitting procedure, we obtained dispersion values compatible to the reported XGAUFIT ones (obtained including all the datapoints).

have low integrated flux values.

Both these differences could be explained considering the different ways the two methods employ to calculate the dispersion. The FILTER keyword in XGAUFIT has a different meaning than RANGE in MOMENTS. Filtering means to exclude the profile with *peak* value lower than a threshold (3σ), but to consider the values below 3σ during the fitting procedure, when these values belong to a profile with peak higher than the threshold. Putting a range in the second moment calculation means instead that, in every profile, the values below 3σ are not taken into account. This generates, without any doubt, a systematic underestimation of the dispersion using the second moments method.

On the other hand, considering background values in the XGAUFIT method could also produce an unrealistic broadening of the profiles, especially of those with low peak amplitude (more influenced by noise during the fitting procedure). To check this possibility, we performed visual inspections of many low S/N profiles, which gave high dispersion values with XGAUFIT, but low values using MOMENTS (in Fig. 2.13 we show some representative profiles for NGC 6946). To decide if we were in the presence of broad profiles we tried to run the fitting procedure excluding all the data below 3σ. In almost all cases we found a dispersion value comparable to that obtained without excluding these data. For this reason we concluded that the Gauss fit procedure gives a more realistic calculation of the velocity dispersion of our

HI profiles.

We noticed however that, for profiles with peak amplitude slightly above the noise, XGAUFIT could give on overestimation of the dispersion value, while MOMENTS largely underestimates it. This effect is particularly present in the very outskirts of the galaxies, regions usually excluded from the studies that we are going to describe in the next chapters.

In conclusion, we decided to perform all the data analysis described in the next chapters on the XGAUFIT genereted maps (Fig. 2.14(a) and Fig. 2.15(a)).
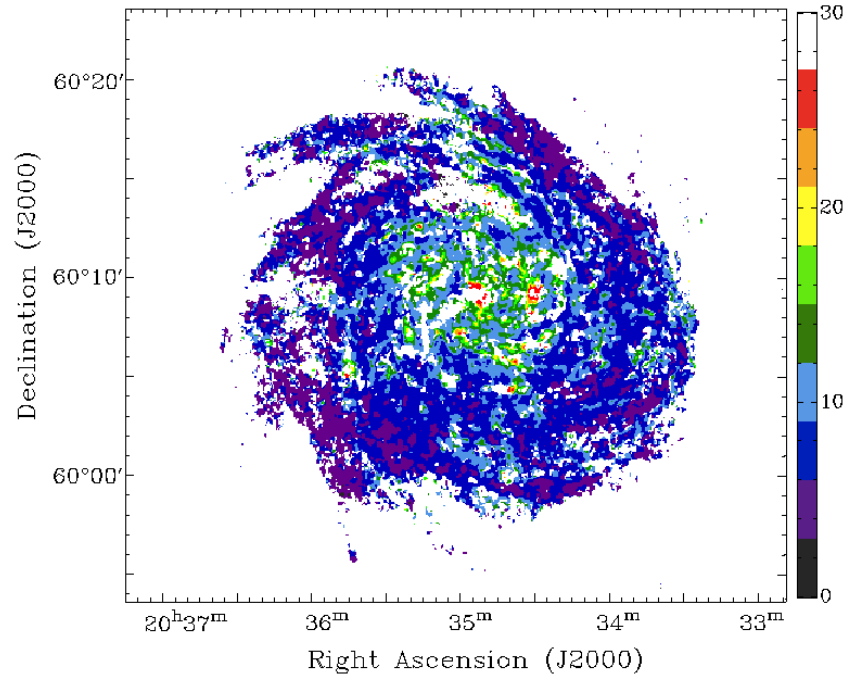
(a) Gaussian fit map
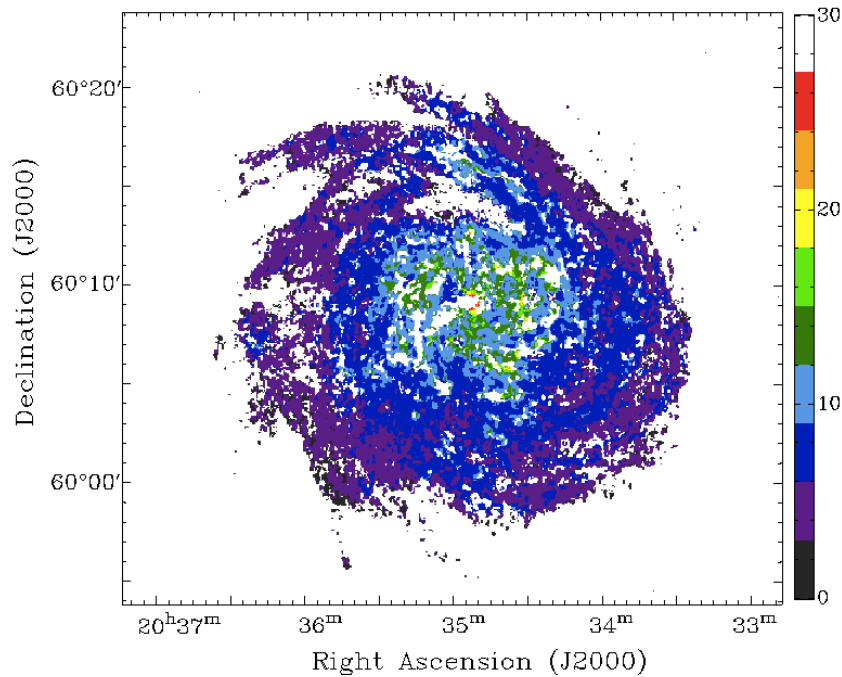
(b) Second moment map

Figure 2.14: Dispersion maps produced for NGC 6946. For both, colours change from purple (3 km s^{-1}) to red (greater than 27 km s^{-1}) in steps of 3 km s^{-1}. Blanks are due to: profiles too bad to fit, amplitude filtering, masks described in 2.5. To get (a) we used GIPSY task XGAUFIT with a single Gaussian fitting function and an amplitude filter of 3σ. The map (b) was obtained with GIPSY task MOMENTS, filtering amplitudes below 3σ and with the parameter WINDOW = 3 (see Sect. 2.6).
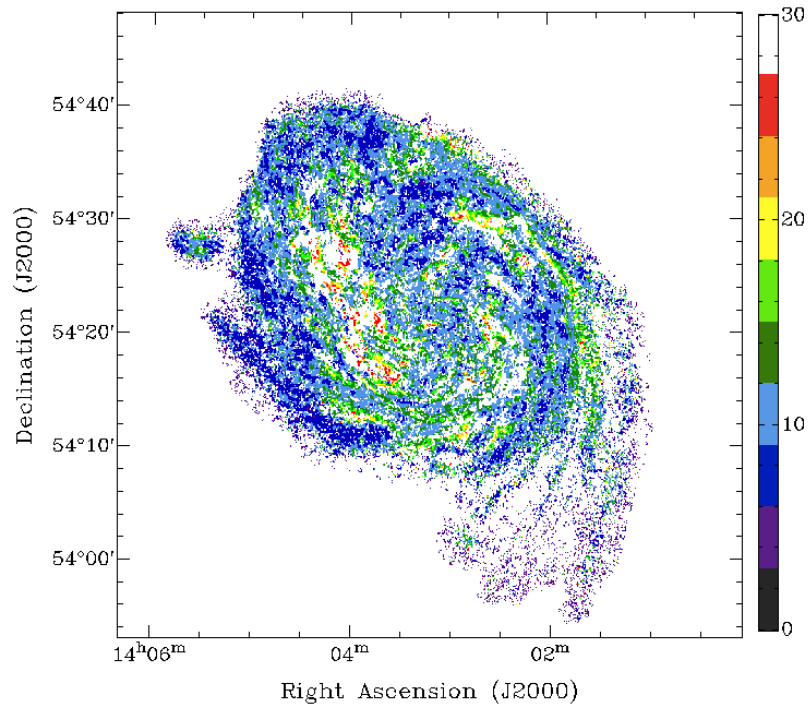
(a) Gaussian fit map
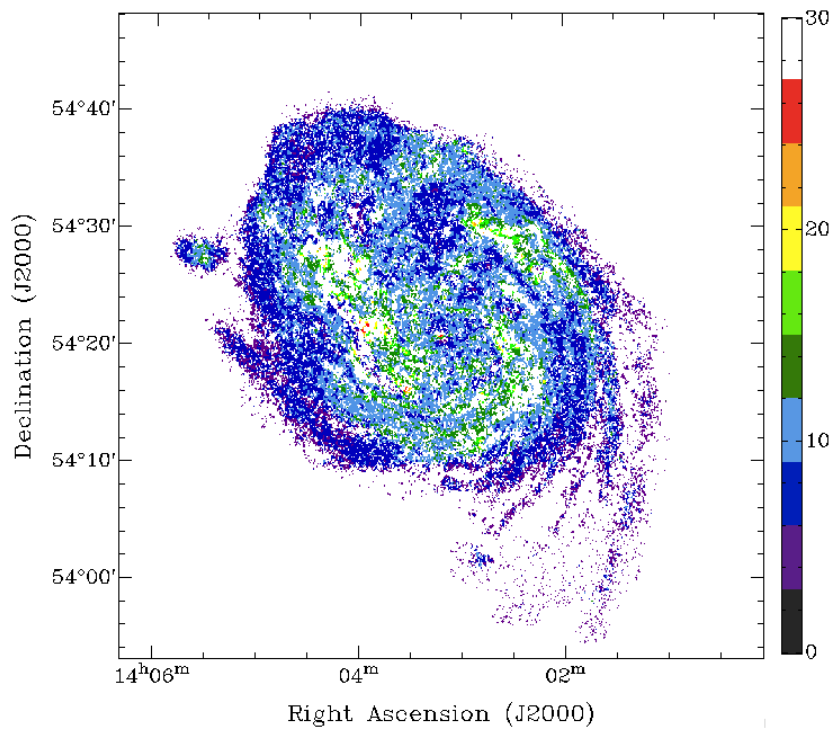
(b) Second moment map

Figure 2.15: As Fig. 2.14, but for M 101.

Chapter 3

Dispersion profiles and spiral structure

In this Chapter we start performing the analysis of the dispersion maps described in Chap. 2 (Fig. 2.14(a) and Fig. 2.15(a)). First of all we discuss the profiles obtained from these maps. Then we describe the adopted procedure to select the arms and the interarms. Later we investigate correlations between HI velocity dispersion and spiral structure in ur two galaxies.

We divide the Chapter in two main sections, one per galaxy. We found this a useful way to present our results, also because the two objects are quite different from each other. At the end of the Chapter we discuss the link between Star Formation Rate and dispersion in the two galaxies, while we leave to Chap. 4 a full comparison of the results obtained.

3.1 NGC 6946

3.1.1 Azimuthal profile

In Fig. 3.1 we report the velocity dispersion azimuthal profile of the NGC 6946 shown in Fig. 2.14(a). To obtain it, we used GIPSY's task ELLINT, with the Inclination and Position Angle parameters reported in Tab. 2.1. Each point in the plot is the average on a beam wide annulus. Error bars are calcolated by ELLINT, as the standard deviation along the ring. Their width reflects the great range of dispersion values present at a fixed radius. Even though these bars are, on average, 2-3 km s^{-1}, from this plot a clear difference between inner and outer disk average
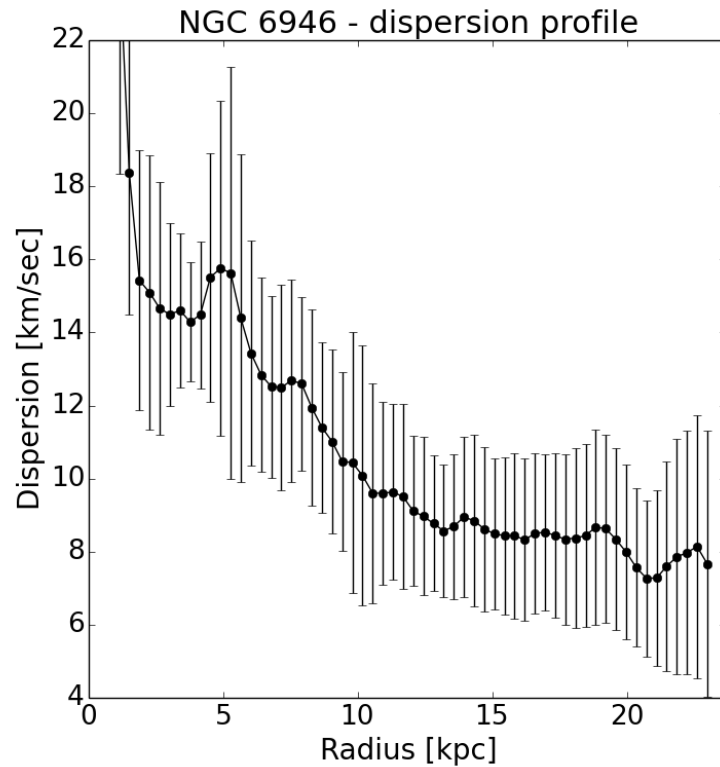
Figure 3.1: Dispersion profile of NGC 6946. Wide error bars are due to the great range of values that dispersion assumes at a fixed radius. Although, a difference is appreciable between inner and outer disk.

values is evident. From the center to the outskirts the average dispersion drops from 14-15 km s^{-1} to 7-8 km s^{-1}. Boomsma et al. (2008) noticed a slope changing at $\sim$ 10 kpc (Fig. 5.1), that it is also visible in our plot (a more complete comparison with literature results is reported in Sect. 5.1.

This decrease between inner and outer dispersion values - that is appreciable also by eye in the map in Fig. 2.14(a) - reflects analogous behaviours observed in infrared and UV Surface Brightness profiles. Muñoz-Mateos et al. (2011) obtained a Star Formation Rate Density profile (SFRD) of NGC 6946(Fig. 3.2), from which the same slope changing is evident, at R$\sim$260 arcsec (near to R$_{25}$ $\sim$ 300 arcsec). In the study that follows, we decided to use this radius to distinguish between the inner and the outer disk.

This close parallel between Star Formation Rate and dispersion profiles in spiral galaxies has already been pointed out in other works (e.g. Lehnert et al. (2009), Green et al. (2010), Green et al. (2014), Moiseev et al. (2015)). These results are of
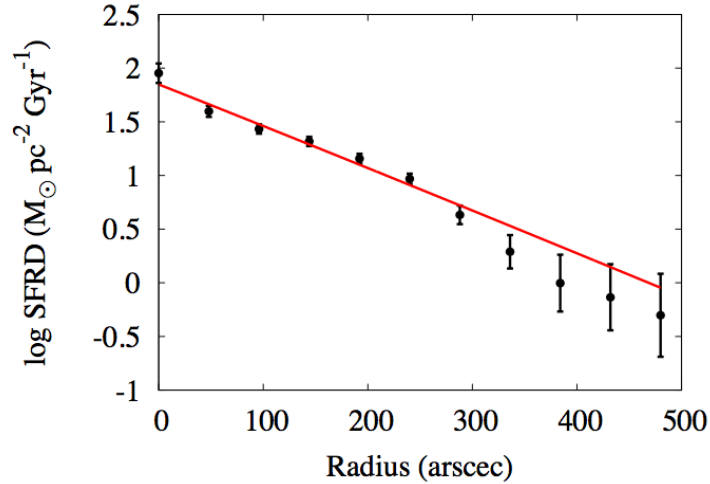
Figure 3.2: Star Formation Rate Density profile of NGC 6946. This picture is taken from the "Atlas" attached to Pezzulli et al. (2015), basing on Muñoz-Mateos et al. (2011) work. Data were obtained from extinction-corrected FUV Galex observation. The red line is a fit realized with a theoretical SFRD profile by Pezzulli et al. (2015). A change in slope is visible at $R \gtrsim 250''$

great interest, being often interpreted as evidence that stellar feedback is the main driver of turbulence in the ISM. In a galaxy like NGC 6946, the high SFR of the central region could explain the high dispersion values there measured. Although that, it is decisive to understand how we can justify the dispersion behaviour in the more external parts of the galaxy, where the star formation does not seem strong.

3.1.2 Tracing arms and interarms

Looking for correlations between stellar feedback and turbulence, our first goal was to compare the dispersion values in the arm and interarm regions.

From wave-density theory indeed, it is though that matter and spiral patterns of a galaxy move at different velocities. As a consequence, gas becomes denser when it enters the arms and this can trigger star formation. Subsequently, stars evolve through the arm, until they leave it from the opposite direction (see the cartoon in Fig. 3.3). Massive stars may complete their evolution remaining within the arm and indeed the arms are regions where we observe SN remnants as well. These phenomena are thought to be at the basis of the feeding of gas turbulence Thus we may expect a correlation between the location of the arms and the measured values of velocity dispersion.

To trace the arms, we used both the HI column density map, and UV surface
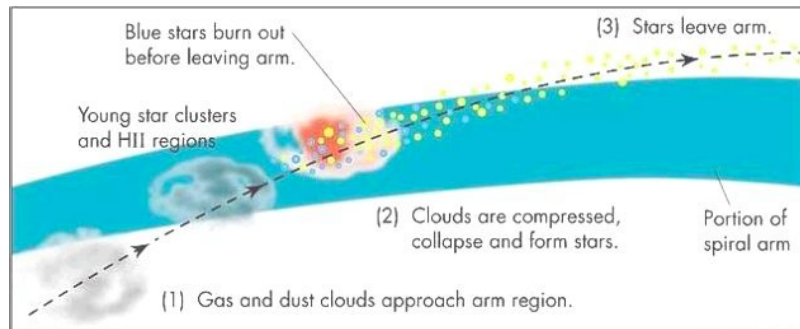
Figure 3.3: A schematic representation of star formation processes along the arms of a spiral galaxy according to the density wave theory. Since a galaxy pattern speed and that of the spiral arms are different (excepted at the corotation radius) gas that encounters a denser region compresses, triggering star formation.

brightness map. We built the HI column density map from our datacube (after eliminating the Milky Way emission, see Sect. 2.2). The procedure used was the following: we smoothed the datacube at two times the original resolution; we calculated the noise of the resulting datacube and we clipped this one at 3σ. In this way, for every channel, we obtained a mask that, in the original cube, individuates the region where there is the proper galactic emission and eliminate the noise. Finally, with GIPSY's task SUM we added single channels emission to obtain the Column Density map (Fig. 3.4(a)). There, arms in the outer disk are visible as higher density regions. For what concerns the inner regions of the galaxy, column densities appear very high, and a distinction between the arms is not recognisable. This should originate from the higher angular velocities and to the strong stellar feedback that appear at low radii. These phenomena might smooth the spiral pattern of the gas in those regions.

We also used a deep UV image of NGC 6946 taken with the Galex satellite (Fig. 3.4(b)). This map (a combination af Near and Far UV) was of decisive importance to trace arms and interarms in the inner disk, for they are not distinguishable in the HI map. In the Galex map there are also various star forming regions in the external part of the galaxy, in particular at least three arm-shaped structures are visible. These structures correspond to the three main arms visible in the HI column density map. We recognized that these three structures are roughly in continuity with the inner arms. We then assumed, determining it by eye, a characteristic flux - both in HI and in UV map - to discriminate arms from interarms, and clipped the data below this threshold. This image was useful to determine the region where arms lie.
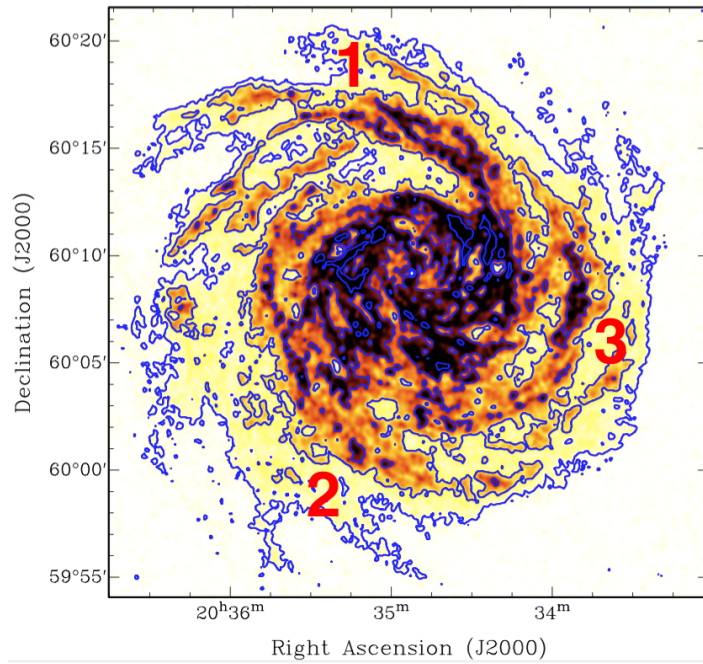
(a) HI column density map
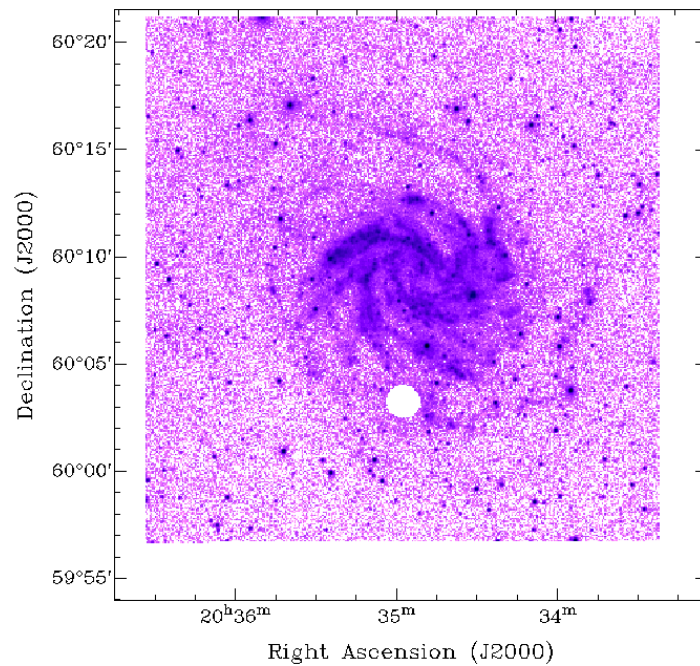
(b) UV Galex map

Figure 3.4: (a) NGC 6946 HI column density map. Contours superimposed are 1, 4, 10, 20 ^{20} cm^{-2} . This map was used in galaxy's arms tracing, in particular in the outer regions (the three most prominent arm-shaped regions are numbered). (b) Galex UV map of M 101 used in our work (taken from the Mikulski Archive for Space Telescopes (*MAST*)). It is a combination of Near and Far UV. Beside the inner bright disk, some external star forming regions are visible.
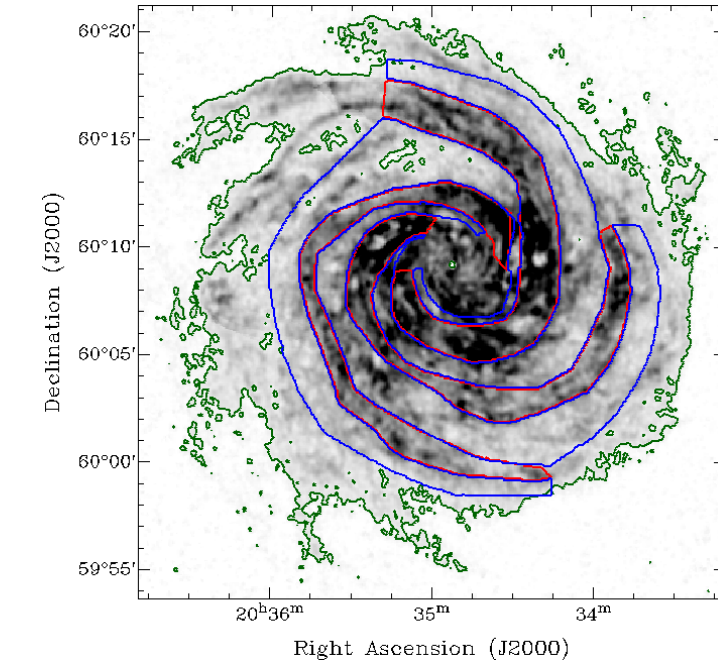
(a) HI column density
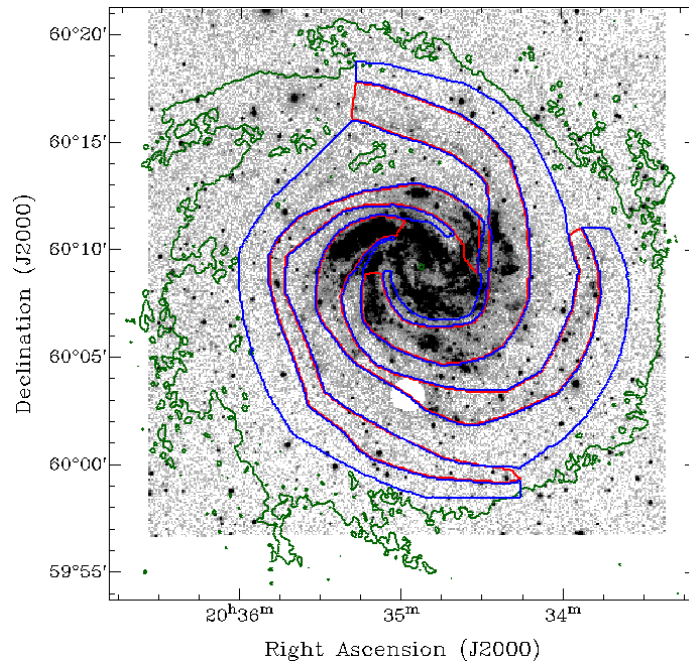
(b) UV

Figure 3.5: (a) NGC 6946 HI column density map and (b) Galex UV map, with arm (red) and interarm (blue) masks superimposed. The blue contour is at 1×10^{20} cm^{-2}. The UV map was important to trace both inner and outer regions, while the HI map was decisive to trace the external parts of the masks. Procedures and criteria to obtain these masks are described in the text.

With all this information collected, using GIPSY's task PYBLOT, we could built by hand a mask for every arm and interarm, see Fig. 3.5.

To obtain these masks presents a number of problems, and in particular the border chosen between arm and interarm could seem a little arbitrary. This is especially a problem in the inner region, where arms and interarms are particularly near one to one another. For this reason we traced very narrow masks there. For the outer disk we decided to be not so strictly tight to the star forming area (evident from the UV picture), but to follow more the HI column density distribution, which generally suggests wider arm structures than the UV bright regions.

3.1.3   Dispersion profiles for arms and interarms

Using the masks in Fig. 3.5, we firstly measured the HI velocity dispersion profiles along the arms and the interarms (Fig. 3.6).

All the points excepted one are compatible within 1σ, then from these data we could
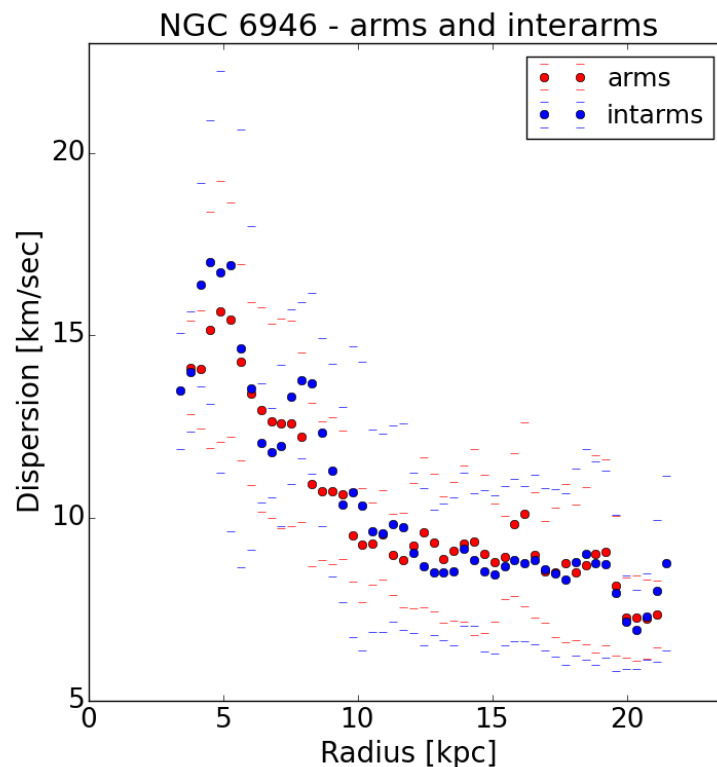
Figure 3.6: Dispersion profiles along arms (red) and interarms (blue) for NGC 6946. Small hyphens indicates the 1σ error bar for each point.

conclude that the two profiles are not significantly different. However, we found an interesting difference between the standard deviations of the two profiles. Averaging them, we found that the one of the interarms is about 0.5 km s^{-1} higher than that of the arms:

$$< \text{RMS}_{\text{arms}} >= 1.98 \pm 0.65 \text{ km } s^{-1} \qquad < \text{RMS}_{\text{intarms}} >= 2.59 \pm 1.17 \text{ km } s^{-1}$$

Considering the average values, the fluctuations of the dispersion values in the regions between the arms are greater than in the arms themselves. The associated standard deviation values tell that the two values are compatible within 1σ, although, the fact that the one of the interarms is almost twice than that of the arms is also significant. Indeed, this might be an indication that the dispersion in the interarms is more variable.

We also studied the RMS profile with radius, but we could not notice variations in its trend from the inner to the outer regions of the galaxy.

3.2   M 101

3.2.1   Azimuthal profile

An analogous analysis to that just described for NGC 6946 has been performed for M 101.

In Fig. 3.7 we report the HI velocity dispersion profile obtained from the map in Fig. 2.15(a). Average dispersion values slightly decrease from $\sim$12 km s^{-1} to $\sim$10
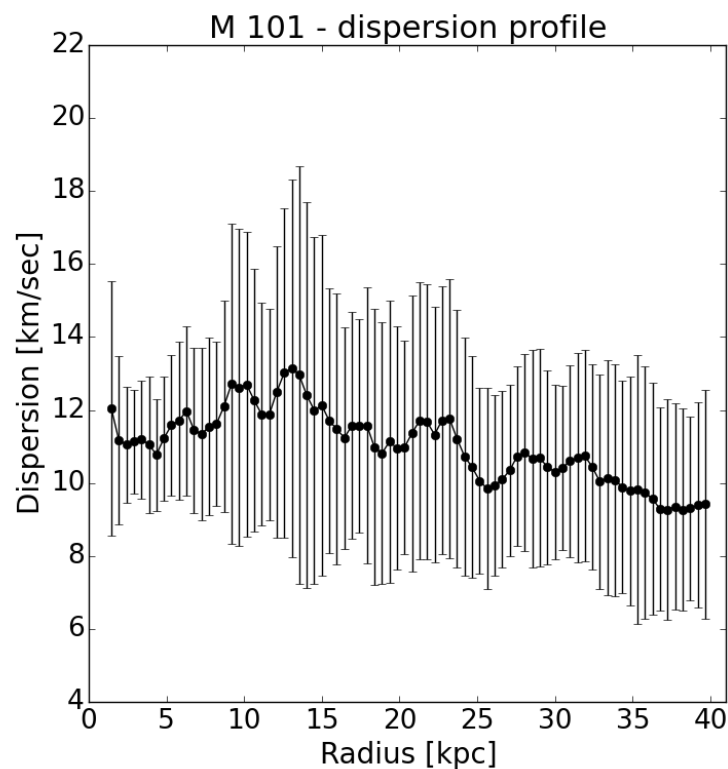
Figure 3.7: Dispersion profile of M 101. Error bars represent the standard deviation calculated for each annulus. The wide ones between R$\sim$8-12 kpc corresponds to the area were the HVC "tail" lies (see Fig. 2.4).

km s^{-1}, even though, considering the error bars, all the values are compatible within 1σ. So, no significant difference between dispersion values seems appreciable in the whole M 101 disk. We refer to Sect. 5.1 for a comparison between our results and the literature. Between 10 and 15 kpc both average dispersion values and the RMS show an increment. This is due to the presence of a significant number of high dispersion values in the region where the the HVC lies.

Also in this case it is interesting to explore a connection between HI velocity disper-

sion and star formation. In M 101, this is strongly taking place not only in the inner regions, but also in the outer disk (out to at least R~23 kpc, also to greater radii in the Northern region of the galaxy), as pointed out by Thilker et al. (2007). This is clearly visible from available deep Galex observations, as that shown in Fig. 3.8(b). For this reason, in M 101 we do not find a clear distinction between inner and outer disk, based on star formation arguments (as we did for NGC 6946, see Sect. 3.1.1). In the next sections, we look for any difference in the dispersion behaviour along arms and interarms, and in the whole galactic disk.

We refer to Sect. 5.1 for a deeper analysis and a comparison between NGC 6946 and M 101 on this point.

3.2.2   Tracing arms and interarms

Using an analogous procedure to that described in Sect. 3.1.2, we produced maps for the arms and interarms of M 101. This result was not straightforward because M 101 is more asymmetrical than NGC 6946. Indeed, in particular in the region where the huge HVC lies, the spiral pattern looks disturbed. In Fig. 3.8(a) we report the HI column density map produced from our observations, while the UV exposure we used is shown in Fig. 3.8(b).

In both images we recognise three main arms that extend from the centre to the outskirts of the galaxy. Many other star forming regions are present, some of these related to minor arms, others with no apparent link with arm structures. In addition to this, also the main arms exhibit non trivial structures: the arm which lies West to the centre (arm n.1 in Fig. 3.8(a)) bifurcates just where the HVC main complex is. A bifurcation is also visible in the southern arm (n.2) - with an elongated star forming structure that extends very far from the centre - and in arm n.3 (just NW to the centre). These bifurcations along the arms are marked in Fig. 3.8(b). In these cases we had three possible strategies to build the masks: i) to interpret all these star forming areas as "arms"; ii) to include at least the UV bright regions related to minor arms (i.e. the bifurcating structures); iii) to limit the "arm" definition to the most prominent features. We decided for this last possibility. Indeed, if our aim is to point out whether energy input from star formation causes turbulence, it should be firstly evident in correspondence with the main arms features.

The resulting mask for arms and interarms is shown in Fig. 3.9, superimposed to the HI column density and UV maps. For the interarms we took care not to include the star forming areas previously described and not considered in the mask of the arms.
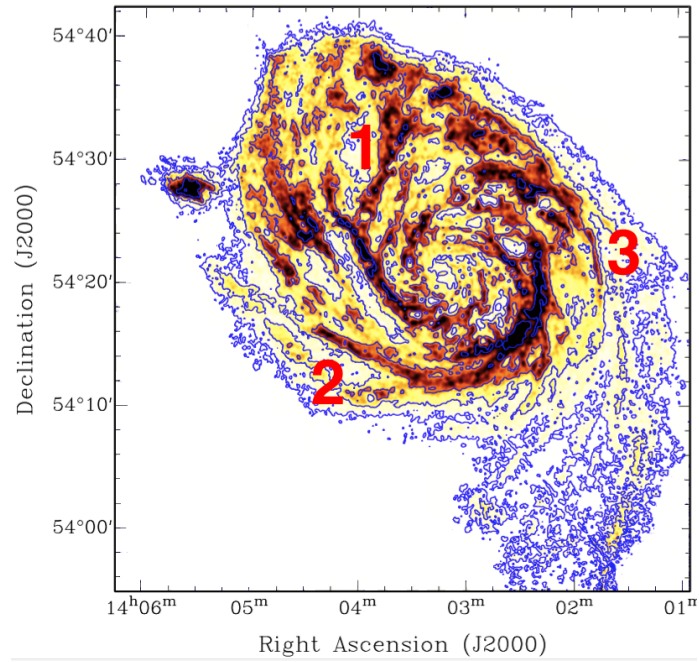
(a) HI column density map
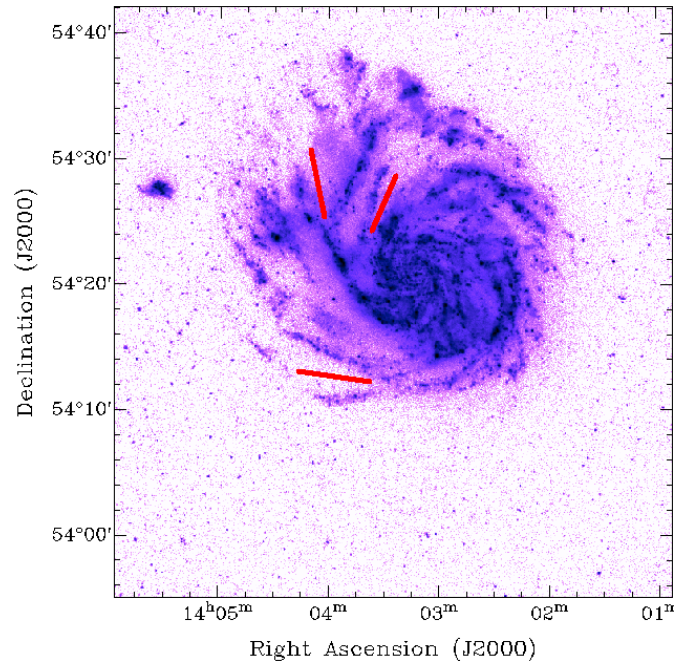
(b) UV Galex map

Figure 3.8: (a) HI column density map of M 101 produced from our observation, with the same procedure as that described in Sect. 3.1.2. The three principal arms are numbered. Contours are 1.2, 4, 10, 25×10^{20}cm^{-2} . (b) Galex UV map of M 101 used in our work (taken from the *MAST* data archive; the PI of the observation is Frank Bigiel), i.e. a combination of Near and Far UV expositions. Main bifurcations between arms are indicated with red lines.
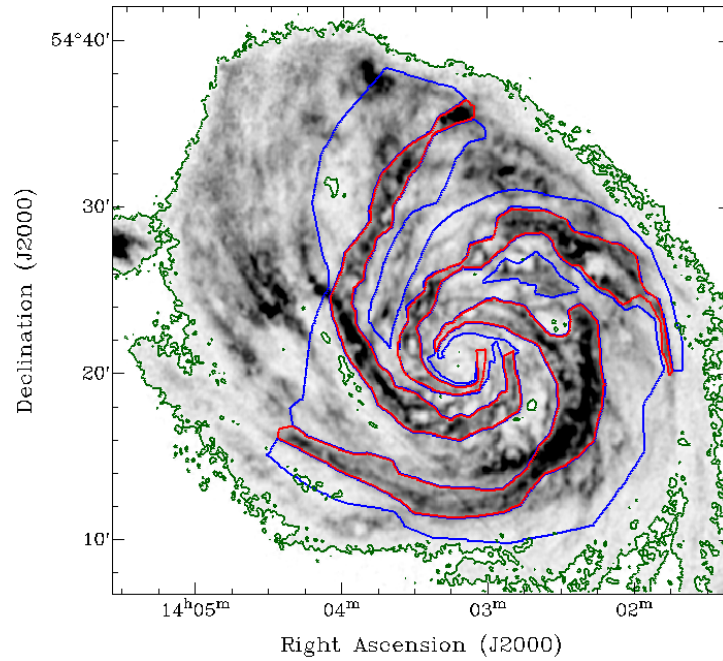
(a) HI column density
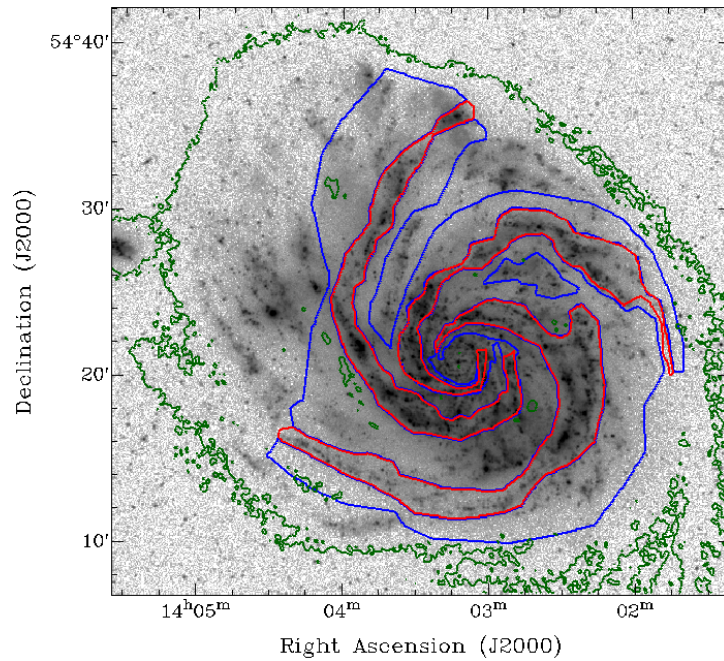
(b) UV

Figure 3.9: (a) M 101 HI column density map and (b) Galex UV map, with arm (red) and interarm (blue) masks superimposed. The blue contour is at column density 2×10^{20} cm^{-2}. In this galaxy, while the external shape of the arms is evident from both HI and UV maps, it was not straightforward to trace the arm shape in the inner regions. To do this, we also compared the HI and UV exposures with visible and infrared images.

3.2.3   Dispersion profiles for arms and interarms

The plot in Fig. 3.10 represents the HI dispersion profile along the selected arms and interarms.
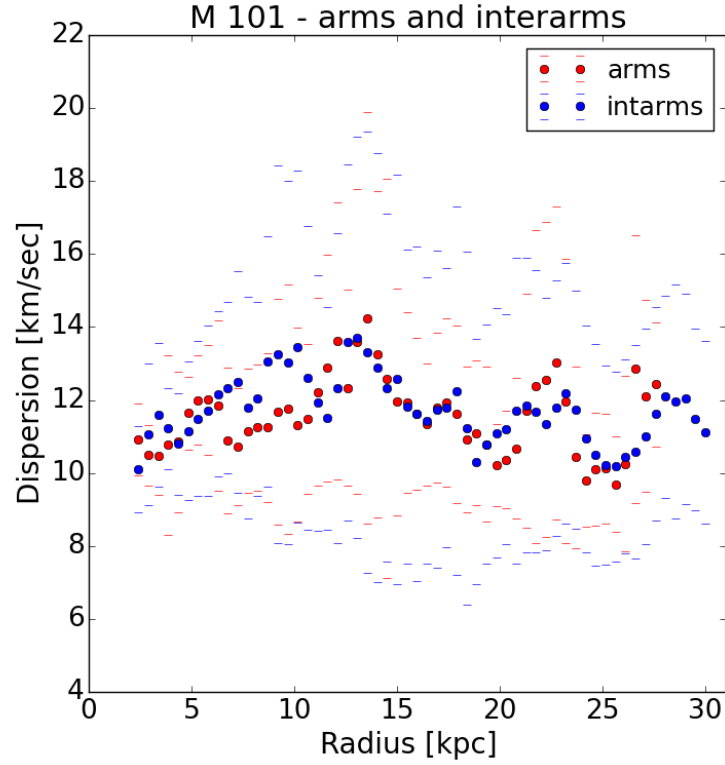
Figure 3.10: Dispersion profiles along arms (red) and interarms (blue) of M 101. Small hyphens indicates the 1σ error bar for each point. The increase in the error bars in both arms and interarms profile around 8 to 15 kpc corresponds to the HVC "tail" (adjacent and external to the western arm, or "n.1").

Almost every point belonging to the arms is comparable to the correspondent one in the interarm within 1σ. Also in this galaxy we can then conclude that no significant differences are present in the profiles.

For the radii correspondent to the region where the HVC lies, an increment in the RMS value is visible. We calculated the average values of the standard deviation for these profiles, obtaining:

$$< \mathrm{RMS_{arms}} >= 2.47 \pm 1.14 \text{ km } s^{-1} \qquad < \mathrm{RMS_{interarms}} >= 3.45 \pm 1.15 \text{ km } s^{-1}$$

Even though the two results are compatible withing 1σ, the average RMS is higher

in the interarms, as was for NGC 6946. In M 101 , this should be also related to the fact that, in the areas corresponding to that where the HVC is (almost all in the interarms region), the profiles are usually wider than the average. The perturbations produced by the HVC could also explain the higher <RMS> found in this galaxy, with respect to NGC 6946(in both arms and interarms).

3.3 Counting the clipped profiles

Once we have decided to eliminate the profiles that are not Gaussian, it is important to understand how much the selection chosen can affect our conclusions. This is decisive also reminding that the profiles we clipped correspond to the regions that should trigger turbulent gas motions (Sect. 1.3).

For both our galaxies we counted this kind of profiles contained in the arms and interarms regions. In Tab. 3.1 and Tab. 3.2 we report the percentages of: profiles which dispersion were not measured by XGAUFIT because the task could not fit the data; asymmetric profiles; high χ^2 profiles. From these tables we see that

profile	Arms	Interarms
not fitted	0.14%	1.64%
asymmetric	6.00%	14.97%
high χ^2	11.69%	4.83%

Table 3.1: Percentages of clipped profiles in NGC 6946, relative to the total surface of the arms and interarms regions (Sect. 3.1.2)

profile	Arms	Interarms
not fitted	0.16%	1.19%
asymmetric	3.38%	10.77%
high χ^2	38.56%	24.91%

Table 3.2: Percentages of clipped profiles in M 101, relative to the total surface of the arms and interarms regions (Sect. 3.2.2)

just a very small number of profiles are not fitted by XGAUFIT. Secondly, in both galaxies there are more asymmetric profiles in the interarms, while in the arms there are significantly more high χ^2 ones. A qualitative interpretation of this result could be the following. The χ^2 method (Sect. 2.5.1) is more suitable in finding double-horn profiles. Since these ones are usually present in correspondence of superbubbles (and then star forming regions, see Par. 2.4), it is expected that these structures are preferentially found in the galactic arms. As explained previously, in a consecutive

moment the profile should evolve, and it could assume a irregular (asymmetric) shape when its gas is become part of the interarm region (due to the galactic evolution).This explanation is particularly fascinating because it may include the results showed in Tab. 3.1 and Tab. 3.2 in the picture described in Sect. 3.1.2 for the feeding of turbulence.

In the Sections that follow we decided to perform our studies on both selected and unselected data, to enlighten the eventual dependence of our results from the sample considered.

Chapter 4

Correlations between dispersion and morphology

In the present Chapter we describe the study that we carried out to look for possible correlations between HI velocity dispersion and the spiral structure of our two galaxies. Also in this case we divided the Chapter in two main sections, one per galaxy.

First, we performed a visual inspection of the dispersion maps, to understand where the broadest profiles are in our sample. Second, we investigated if neutral hydrogen flux and dispersion exhibit some trend depending on their location in the galaxy. Finally, we performed some statistical studies on our results.

4.1   NGC 6946

4.1.1   Broad profiles locations in the galaxy

To understand if a relationship between flux and HI velocity dispersion is present, we started by producing a map that indicates where the broadest profiles in the galaxy are. Fig. 4.1 shows a velocity dispersion map where profiles with width greater and smaller than 10 km s^{-1} are indicated with different colours (green and red, respectively). It is clearly visible that most of the high dispersion values are in the inner region of the disk (see Sect. 3.1.1). Although, the most interesting feature that emerges from this picture is that there are some regions with broad profiles also in the external part of the disk (see the ellipses in Fig. 4.1). Furthermore, these areas are usually located adjacent - but outside - to the arms (shown by the HI contours).

Excluding the most external regions, where the high dispersion values could be due
to uncertainties of measurements (by GIPSY's task XGAUFIT), these result is quite
interesting. Indeed, it is a first indication that in the outer disk, at least locally, low
column densities (as interarms are) can correspond with high velocity dispersions.
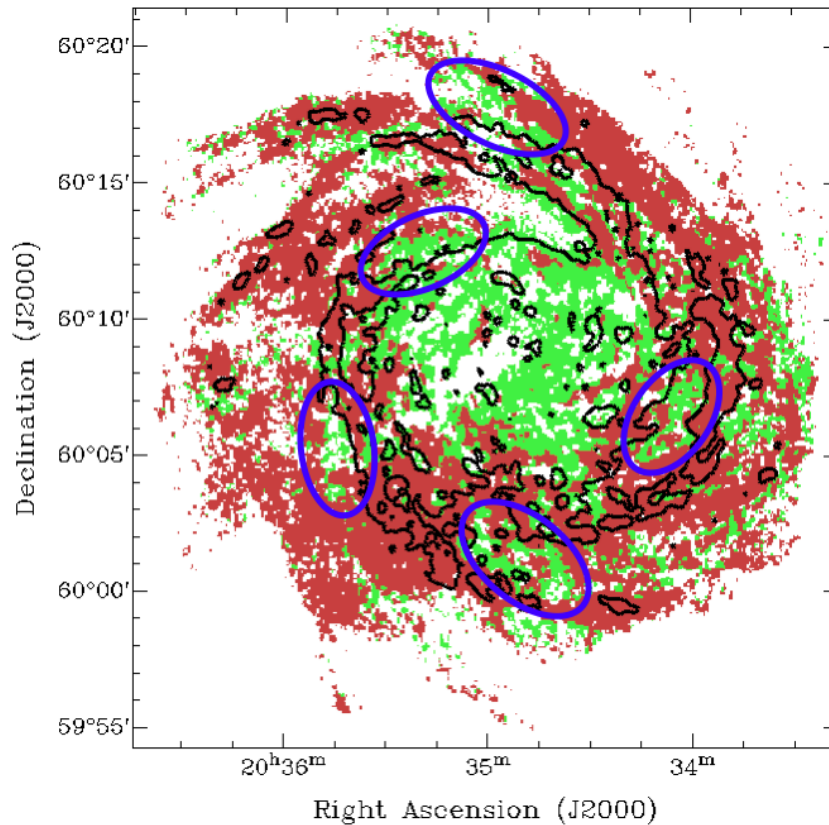
Figure 4.1: Dispersion map of NGC 6946. Profiles with dispersion broader than 10 km
s^{-1} are coloured in green, while red regions correspond to dispersions smaller than 10 km
s^{-1}. The black contour is at a column density of $0.7 \times 10^{21} cm^{-2}$, and it roughly indicates -
for the outer disk - the position and shape of the HI arms. Blue ellipses indicate five main
high dispersion regions in the outer disk. As visible, they are located in the interarm region,
adjacent to the arms.

4.1.2   Contour plots

To investigate more deeply if there is a relationship between HI density and
velocity dispersion, we produced **contour plots** of these two quantities, point by
point across the disk (Fig. 4.2).

We divide this section in two: in the first we plot the dispersion against the peak
flux, while in the second against the column density. The peak flux is measured
in Jy beam^{-1}, then, unlike the column density, it is independent of the width of

the profile. Thus, the analysis of the peak flux might be interesting to study how
dispersion varies in relation to the S/N ratio of the profiles.

Dispersion with peak flux

In each plot we calculate velocity dispersion and peak flux for every pixel in the
galaxy and plot the occurrance of their value in contours in the σ vs. S_{peak} plane.
The contours represent the number density of the data that fall in a certain area of
the plot. In this paragraph the data are normalized to the total number of pixels
considered, hence the final results are given in percentage. The width of the bins (of
the grid used to perform the contour plot), is 1/40 the axis width, in both axes.
First, we produced the contour plots for the inner and the outer region of NGC
6946 disk (the separation between the two is the usual 260 arcsec ellipse, see. Sect.
3.1.1). The results are shown in Fig. 4.2. The main difference which leaps to the
eye is the different shapes these plots have: the one relative to the inner disk has
an approximately "banashape", while the other is almost triangular. Both of them
do not present a significant internal substructure, with a unique contour containing
the 25% of the data in the centre of the distributions. Also reducing the bin size
up to 1/80 the axis width, we could not find significant differences. The "bulk" of
the data is located in different points in the two plots. This is not surprising, as we
have already known from the dispersion profile studies (Fig. 3.1) that in the internal
regions of the disk (obviously more luminous than the outskirts) the dispersion is
higher. Inside 260 arcsec no values below 8 km s^{-1} are present (considering the 5%
limit). The banashape arrangement of the data looks curious. Nevertheless, we think
it is just a consequence of the fact that in the inner disk there are no low column
density profiles. This means that those with low peak fluxes are usually broad, since
the only way to populate the lower-left side of the plot is to have low peaks and
narrow profiles. This suggests a kind of anticorrelation between width and height of
the profiles. We will further investigate this point later.
In the disk outside 260 arcsec the shape is triangular, showing two interesting trends.
For high peak fluxes, the dispersion is confined to a typical value of 8 km s^{-1}. At
lower fluxes the range of allowed dispersion spans from ~ 4 km s^{-1} to ~ 15 km s^{-1}.
Although the general shapes of the plots look very different, in analogy with the
inner disk, we see high dispersion values at low peak fluxes. The main objection that
one could raise, especially for the outer disk, is that the high dispersion at low flux
values are not really significant. We remand to the discussion in Sect. 2.6.1 and to
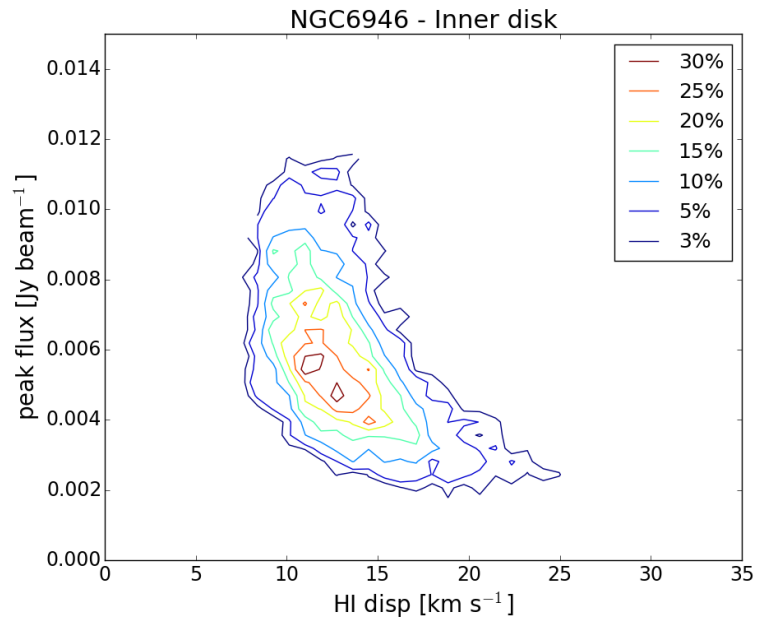
(a) R < 260 arcsec ellipse
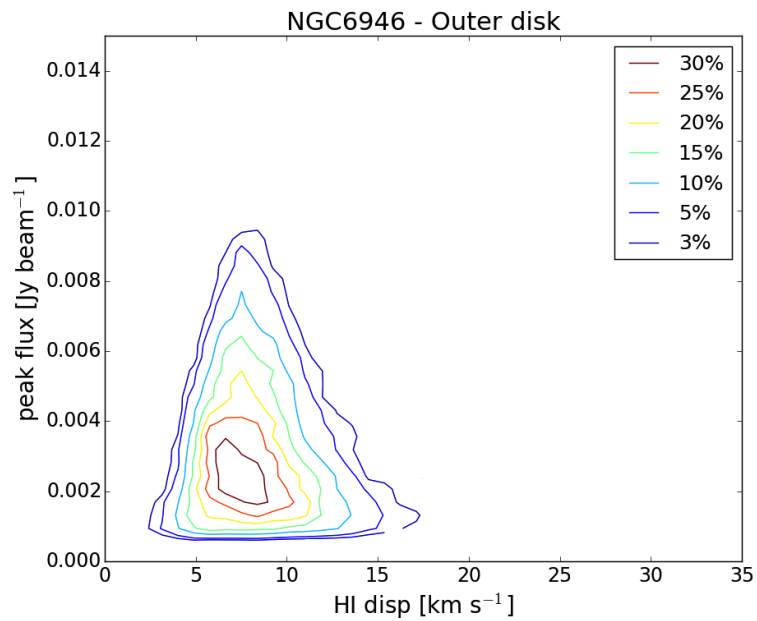
(b) R > 260 arcsec ellipse

Figure 4.2: 2-D histogram ("contour plot") of the dispersion-peak flux relationship in NGC 6946. Contours indicate the (normalized) number density of the profiles extracted from every pixel in the spatial map. The bin size is 1/40 the axis width. Picture (a) is referred to the disk region within R=260 arcsec from the centre, while (b) is relative to the disk beyond that radius.

(a) Arms region
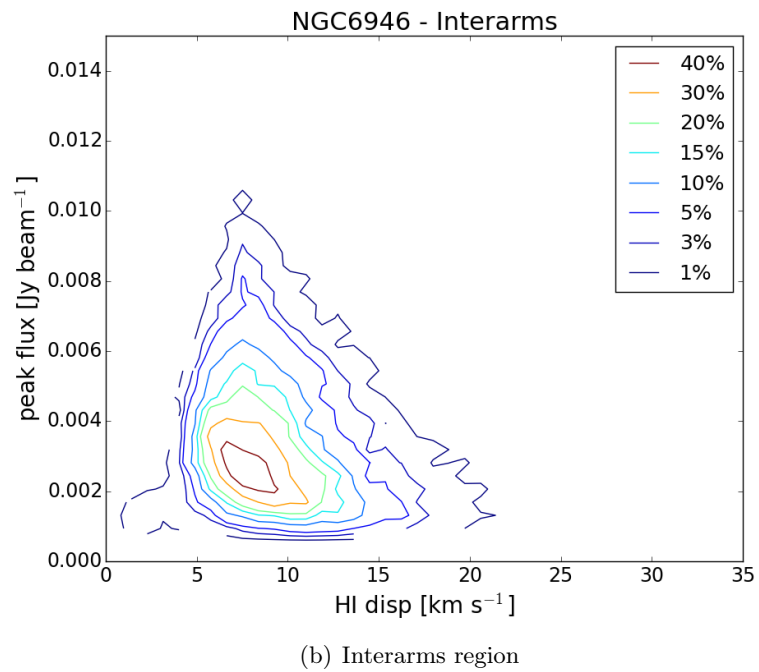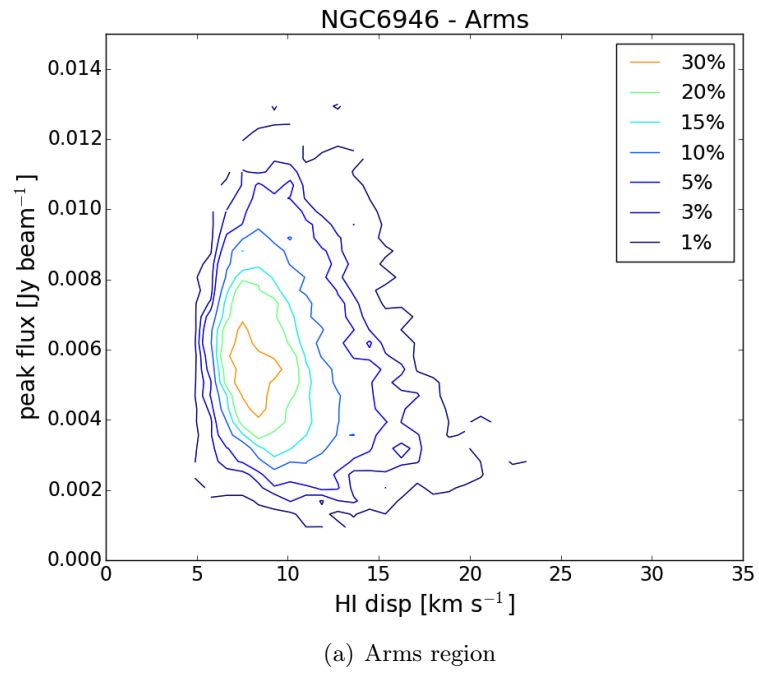
(b) Interarms region

Figure 4.3: The same as Fig. 4.2 but now (a) is referred to the arms region, and (b) to the interarms one.

Fig. 2.13 on this point, where we conclude that we can be confident about the
fits of the low S/N peaks. Another point to discuss is the selection of the profiles
considered: it may exclude particular kind of profiles (for example some that could
be broad and with high flux). However we remind that there are precise reasons for
why we adopted this selection: considering only simple Gaussian profiles, we should
have included regions where just thermal broadening and fully developed turbulence
operates (Sect. 2.4). Then, it is in any case remarkable that - *given this selection -*
the behaviour is the one previously described. Although, we also realized the same
contour plots without any selection of the profiles, i.e. without applying the masks
described in Chap. 3, obtaining really similar results (we do not show these plots).
In conclusion, we can consider the fact that most of the broad profiles have low peak
flux as a real property of the neutral medium. The other interesting outcome we
get is related to the inner disk plot: its banashape suggests that total line flux is
constant, for low peak fluxes have always high dispersion values.

We also produced two contour plots for the arms and the interarms regions. The
masks used to trace them are those described in Sect. 3.1.2. The results are showed
in Fig. 4.3. Also in this case, the shapes are different, even though not as much
as for the previous plots. While the interarms are disposed in a roughly triangular
way, the arms distribution is more oval. In both cases the peak is located around
7-8 km s^{-1}. Considering the 5% contour, for the arms the minimum dispersion is
5 km s^{-1}, while for the interarms is slightly lower: 4 km s^{-1}. Arms do not present
values greater than 15 km s^{-1}, while interarms can reach 17 km s^{-1}. The behaviour
observed in the previous plots relatively to the highest dispersion values (that they
occurr in low S/N profiles) is confirmed in particular for the interarms. We also
produced the same plots without any selection of the profiles, obtaining shapes not
substantially distinguishable from those just described.

Dispersion with column density

The relationship between neutral hydrogen velocity dispersion and column den-
sity may have a deeper physical meaning than that with the peak flux. A similar
analysis was performed in the past by Shostak and van der Kruit (1984) on NGC 628
and by van der Kruit and Shostak (1984) on NGC 1058. We will compare their re-
sults with ours in Sect. 5.2. It is important to be aware that the now we are plotting
two correlated quantities, since the column density is proportional to $\sim$ peak flux $\times$
width. Thus, it is possible to get spurious trends of the dispersion with column den-
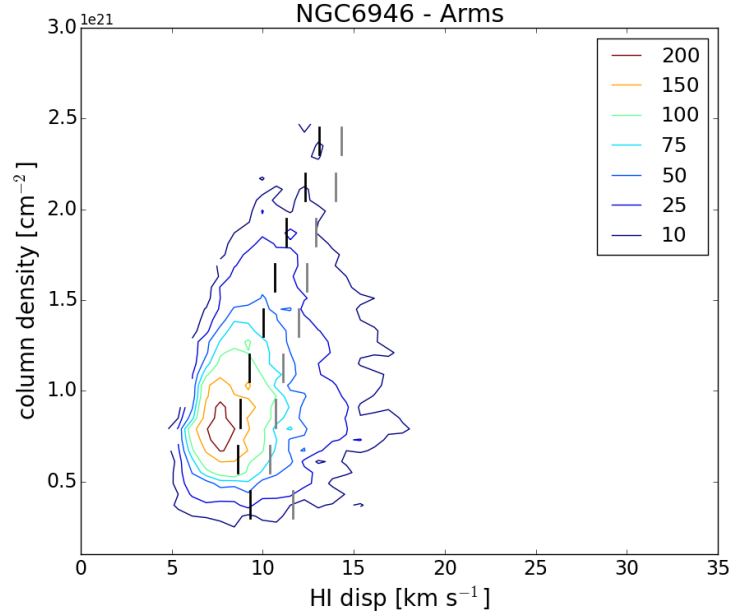
(a) Arms region
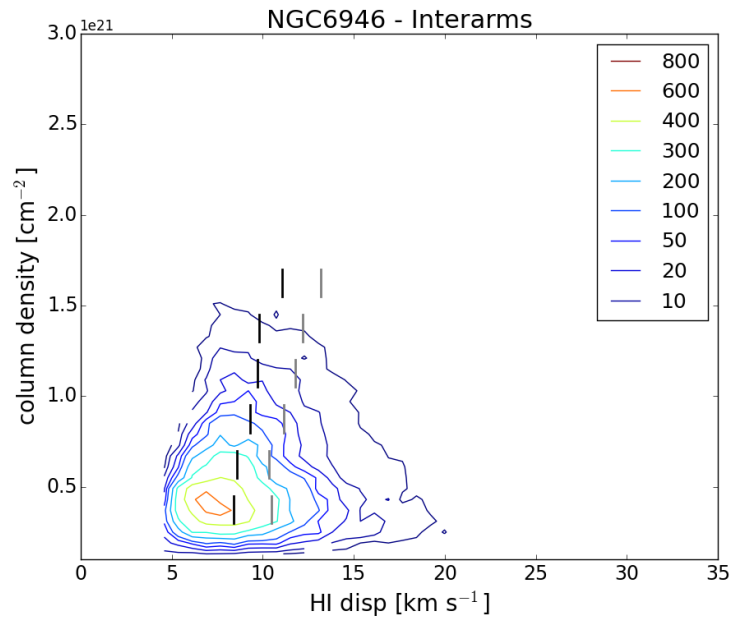
(b) Interarms region

Figure 4.4: Contour plot of the dispersion-column density relationship in NGC 6946.
Contours indicate the number density of the profiles extracted from each spatial pixel on the
galaxy. The bin size is 1/40 the axis width. The black horizontal bars indicate the medians
of the dispersion distributions at fixed density, while grey bars are the third quartiles. Each
distribution spans a range of $\Delta_{HI} = 2.5 \times 10^{20}$ cm^{-2}, starting from 2.5×10^{20} cm^{-2}, and it
contains a minimum of $\sim$250 values. Panel (a) is referred to the arms region, (b) to the
interarms one.

sity. This eventuality may be checked for instance with specific simulations, even
though we think likely that the effect is not strong enough.

In Fig. 4.4 we show the contour plots of the arms and the interarms. For every
fixed density range, we overplotted the median value of the corresponding dispersion
distribution (the black vertical bars in the plot), and the third quartile (grey bars).
Their values are in Tab. 4.1.

	ARMS		INTERARMS	
N_{HI} range $[10^{20}cm^{-2}]$	Median $[km\ s^{-1}]$	3rd quartile $[km\ s^{-1}]$	Median $[km\ s^{-1}]$	3rd quartile $[km\ s^{-1}]$
2.5 - 5.0	9.28	11.63	8.38	10.49
5.0 - 7.5	8.61	10.37	8.56	10.35
7.5 - 10.0	8.77	10.69	9.29	11.14
10.0 - 12.5	9.28	11.13	9.69	11.77
12.5 - 15.0	10.02	11.95	9.81	12.19
15.0 - 17.5	10.66	12.44	11.08	13.17
17.5 - 20.0	11.27	12.90		
20.0 - 22.5	12.35	13.98		
22.5 - 25.0	13.09	14.33		

Table 4.1: Median and third quartile values, for every column density range, for the arms
and interarms distributions of NGC 6946 (cfr. Fig. 4.4).

If we consider a single density range, and we compare the median value of the disper-
sion distribution of the arms with that of the interarms, we cannot observe significant
differences (we will return to this point in the following section). The most interest-
ing feature that emerges in these plots is the trend that the median values exhibit
at increasing column density. In both arms and interarms, the higher the column
density, the broader the profiles. However, in the interarms plot, we see that the
highest dispersions ($\gtrsim 17$ km s^{-1}) correspond to low column densities profiles. The
effect appears less strong than in the peak flux plots we displayed in the previous
section. This is not very surprising, though, since low S/N peaks can have a great
integrated flux.

4.1.3 Statistical analysis

Until now we have described the main analogies and differences between the con-
tour plots that we realized. To understand if we are or not in presence of significant
features a proper statistical analysis is needed.

We simplified the previous analysis realizing simple one-dimensional histograms

of the dispersion. Probably one of the most interesting feature we previously noticed
is the tendency of the high dispersion values to have low peak. Thus, we decided to
compare the higher values of the dispersions distributions. A simple way to obtain
this is to calculate their so called **third quartile**. This is defined as the value below
which three quarters of the data fall. Similarly, in the first quartile one quarter of
the data are contained, while the second, or **median**, divides the distribution in two
parts that contain an equal number of data. The third quartile is then a particularly
useful tool to compare the upper tails of the distributions.

In Tab. 4.2 we show the results obtained for the four sample described in the previous
subsection, with median and first quartile also showed. As expected, all quartiles

	1st quartile [km s^{-1}]	Median [km s^{-1}]	3rd quartile [km s^{-1}]
R < 260" disk	10.99	12.78	15.01
R > 260" disk	6.61	8.09	9.93
Arms	7.81	9.35	11.41
Intarms	7.13	8.66	10.73
WITHOUT SELECTION ON THE PROFILES			
R < 260" disk	11.15	12.99	15.37
R > 260" disk	6.66	8.25	10.22
Arms	8.08	9.68	11.95
Intarms	7.22	8.89	11.13

Table 4.2: Statistical exam of the dispersion in NGC 6946.

referred to the inner and outer parts of the disk (within 260 arcsec) are particularly
different. We also performed a comparison between the arms and the interarms
regions. All the three values are not particularly different, and - a bit surprisingly
- both median and quartiles for the arms are slightly larger ($\sim +0.7$ km s^{-1}). This
could appear in contrast with what we expected from the contour plots in Fig. 4.3,
where the interarms reach the highest dispersion values. The result obtained for
the third quartile then, indicates that this attitude is proper of the very largest
values of the distributions. However, the quartiles are not a very sensitive test to
compare two distributions on their whole. In the following we describe some further
statistical analysis that we think more suitable to attend this goal. Regarding the
first quartile, the lowest value is that of the interarms distribution, confirming what
we have already seen in the contour plots.

We also performed the same analysis but without any selection on the profiles (on
the same regions). The results are in the second half of Tab. 4.2. All the quartiles

are slightly higher than in the case with the selection, but the differences are not
remarkable: the highest are for the third quartile of the arms ($\sim +0.5$ km s^{-1}) and
of the interarms distributions ($\sim +0.6$ km s^{-1}). As a consequence, also the differ-
ence between the quartiles for the distributions without selection is not significant
($\sim +0.8$ km s^{-1}).

We think it is particularly robust that our results do not depend on the selection con-
sidered. However, it is due to say that the quartiles are not a particularly sensitive
test, since they compare just single points of the corresponding cumulative distri-
bution functions (CDF). For this reason we decide to use other statistical methods,
which are sensitive to the entire range of the CDFs.

A widely used method to fulfil this goal is the **Kolmogorov-Smirnov test**
(K-S test), that determines if two cumulative distributions are or not compatible
to one another. To implement the test we used the python function "ks_2samp",
belonging to the scipy.stats library. This compares two empirical distribution, giving
two outputs. The first is the "*D-value*", that is the maximum distance between
the two cumulative distribution of the data (Fig. 4.5). The other is the "*p-value*",
a parameter which defines if the distributions are drawn from the same one. In
practice, the p-value gives the probability that, if the two samples come from the
same distribution, the D-value between their corresponding cumulative distributions
would have been as large or larger than the one measured from the data. Then,
the lower the p-value, the more probable is the hypothesis that the distributions are
different.

The K-S test for the distribution of the inner and outer disk returned a D-value
of 0.63, that corresponds - as expected - to a complete incompatibility of the two
samples. Concerning the arms and interarms regions, we measured D-value = 0.13
and a very small p-value. According to the K-S test indeed, for distributions of such
a big size (the order of magnitude is 20000 elements), just a small difference between
the two cumulative distributions indicates a complete incompatibility among them.

Also K-S test on the unselected data substantially confirm what we concluded in
the analysis just described.

In conclusion, we can summarize what seen until now as follows. Both considering
the single Gaussian profiles and the whole disk without any selection, the dispersion
values in the region within the R = 260 arcsec ellipse in NGC 6946 is statistically
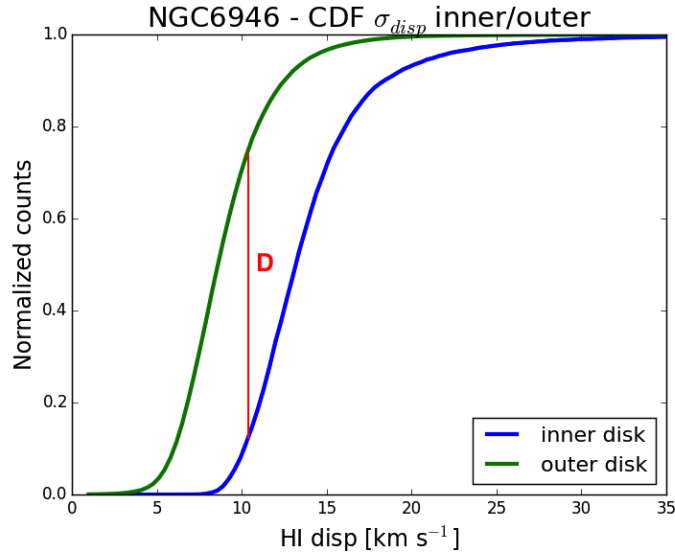
Figure 4.5: Cumulative distributions of the dispersions of the inner (R < 260 arcsec, blue curve) and outer region (R > 260 arcsec, green curve) of NGC 6946. The D-value (maximum distance) is 0.63, and it is indicated with the solid red line. As indicated in the text, the KS-test says that the two distributions are different.

different from the outer disk. The results on the arms/interarms comparison look more complex. Considering the quartiles values the arms sampling does not exhibit *statistically meaningful* differences in HI dispersion from that of the interarms. Otherwise the KS-test (sensible to the entire range of the distributions) would suggest that the distributions are different. This would confirm what we saw in the visual inspection (Sec. 4.1.1). It could be interesting to improve the statistical analysis, for instance performing a bi-dimensional KS-test (Fasano and Franceschini, 1987).

From another point of view, the 2-D contour plots in Fig. 4.4, have shown that dispersion is larger for high column density profiles. Then, the picture that emerges from this study on NGC 6946 is that, both *inside the arms and the interarms regions* the HI dispersion correlates with the gas column density.

In apparent contradiction, from the contour plots referred to the peak flux (Figg. 4.2 and 4.3) we have seen that the broadest profiles have mostly low peak. The fact that, also in this case, this observation is independent from the selection, gives further interest to the result.

4.2 M101

4.2.1 Broad profiles locations in the galaxy

In Fig. 4.6 we show a dispersion map of M 101, where we have indicated with
different colours the profiles with HI dispersion broader or smaller than 10 km s^{-1}.
This is analogous to what we did for NGC 6946 (Fig. 4.1).
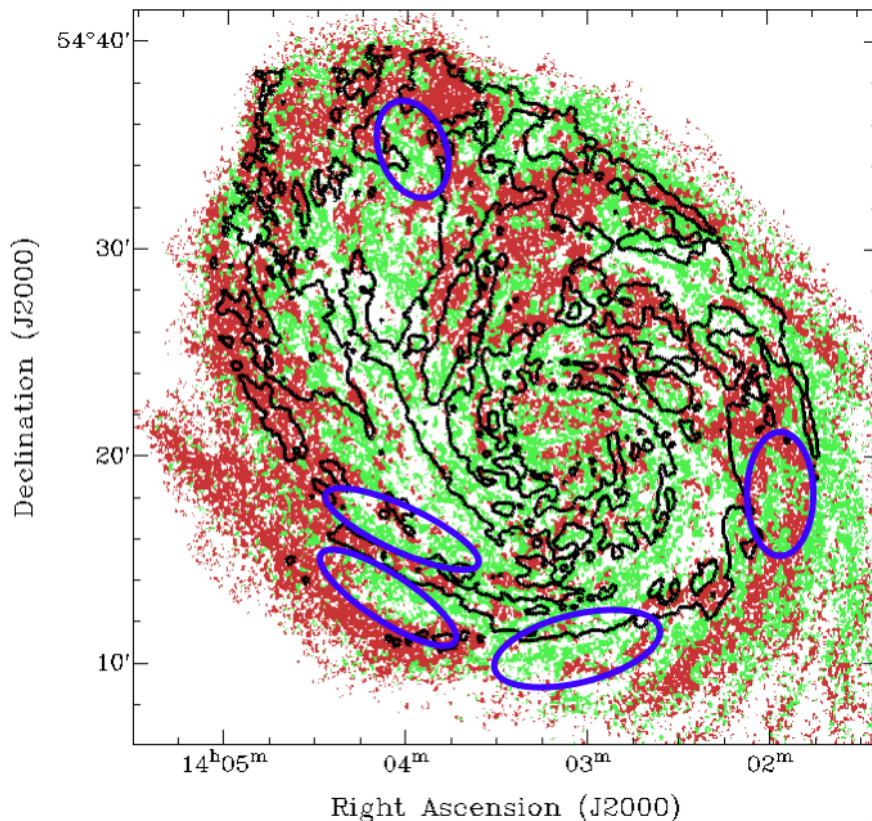
Figure 4.6: Dispersion map of M 101. Description is analogous to that of Fig. 4.1, excepted
that the black contour is at column density of $10^{21}cm^{-2}$.

High dispersion regions (in green) are more distributed all over the disk in this
galaxy, reflecting the azimuthal behaviour of dispersion we discussed in Sect. 3.2.1.
Also in this galaxy we distrust the data relative to the galactic outskirts. Indeed,
they correspond to very low S/N profiles, and they could be affected by uncertainties
in the dispersion measurements operated by GIPSY's XGAUFIT.

Another region which requires some care is that corresponding to the HVC. Although
in that area a lot of values were clipped by our selecting procedure (Sect. 2.5), there
are a significant number of remnant profiles. It is interesting that most of them -

both in the arm and the interarm - have dispersions broader than 10 km s^{-1}. This
probably reflects the highly animated nature of this part of the galaxy.

For what concerns the rest of the galaxy, we could not see the correlation between
broad profiles and low column densities that we outlined in some localized region of
NGC 6946 (Fig. 4.1). The green and red profiles, as said, seem in fact to be more
balanced through the galaxy. However, in Fig. 4.6 we indicated with blue ellipses
some high dispersion region that are located in the interarms. We think that the
most interesting ones are the two adjacent to the end of the southern arm, also
considering that the arm presents dispersion values smaller than them.

4.2.2 Contour plots

Differently from NGC 6946, M 101 galaxy does not show a clear separation
between inner and outer disk, considering the surface brightness. As a consequence
we performed the same analysis explained for NGC 6946 (Sect. 4.1) just for the arms
and interarms regions.

Dispersion with peak flux

To study the arms and the interarms we used the masks described in Sect. 3.2.2.
The contour plots produced between dispersion and peak flux are shown in Fig. 4.7.
Interestingly, we recognized many features found in the arms and interarms plots
of NGC 6946 (Fig. 4.3). In particular, neglecting the 1% contour, the shape of the
arms plot is similar to that of NGC 6946. Also for the interarms the same roughly
triangular shape is observed, even though in this case it is more elongated toward
high dispersions. The peak in velocity dispersion is positioned around ~ 10 km s^{-1}
in both plots of Fig. 4.7.

If we consider the 5% contour, the lowest values for the arms is ~ 8 km s^{-1}, while for
the interarms is ~ 7 km s^{-1}. As regards the highest profile width, we found ~ 15 km
s^{-1} for the arms and ~ 18 km s^{-1} for the interarms. For the latter, the dispersion
values are then slightly higher than in NGC 6946.

Especially in the interarms, it is remarkable the tendency of the broadest profiles to
have low peak fluxes. This trend is analogous to what we have seen in NGC 6946,
and we refer to Sect. 4.1.2 for the discussion on possible biases.

We also produced the same contour plots without selections of the profiles (i.e. not
using the mask we described in Chap. 3). There is just a small difference in the
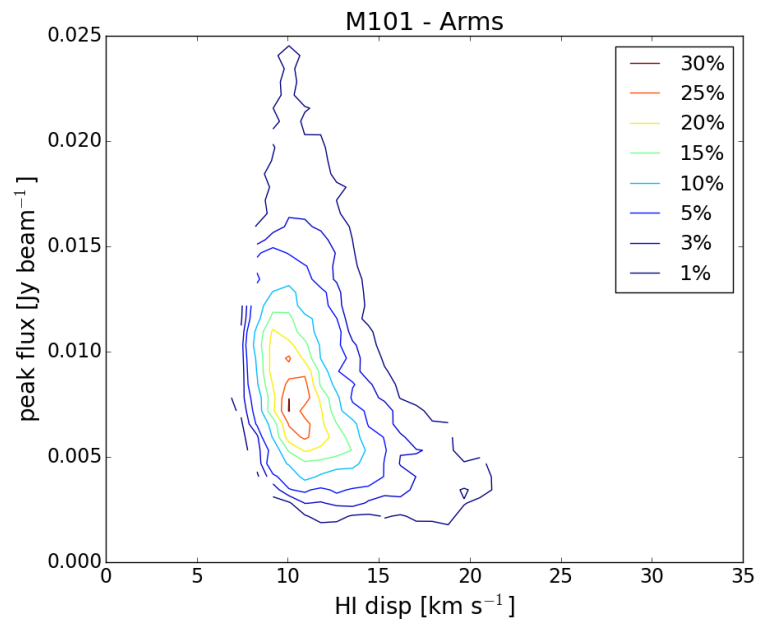
(a) Arms region
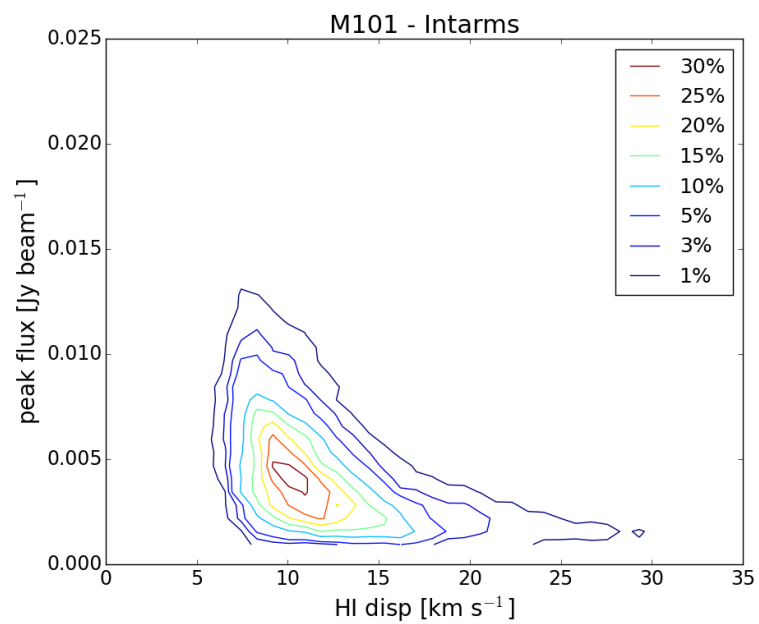
(b) Interarms region

Figure 4.7: The same as Fig. 4.2 but now referred to M 101's arms (a) and interarms (b) region.

interarm plot, where the profile widths reach $\sim$ 19 km s^{-1} (instead of $\sim$ 18 km s^{-1} for the selected Gaussian profiles). This should be due to the inclusion of many profiles which are located in the region where the HVC lies. There, profiles shows deeply disturbed features (broad wings, double peaks), and XGAUFIT's single Gauss fit usually measures dispersions higher than average. Given their anomalous shape, these profiles were eliminated by our selecting procedure (Sect. 2.5).

Dispersion with column density

As for NGC 6946, for both arms and interarms we produced contour plots of the HI dispersion against the column density. We show them in Fig. 4.8.
It is particularly interesting to compare this plots with those of NGC 6946 (Fig. 4.4). We do this considering the quartiles of the dispersion distributions at fixed column density range. We plot them as vertical bars on the contour plots, reporting their values in Tab. 4.3. For what concerns the arms, these quantities are roughly constant. This is decisively different to what we observed in NGC 6946, where dispersion was greater for high column densities. Moreover, the third quartile of the distributions taken for $2.5 \times 10^{20} <$ N$_{HI} < 5.0 \times 10^{20}$ is significantly higher than the others (17.38 km s^{-1}). This reflects what we have seen for low S/N profiles in Fig. 4.7(a).

| N$_{HI}$ range | ARMS | | INTERARMS | |
| | Median | 3rd quartile | Median | 3rd quartile |
[10^{20}cm^{-2}]	[km s^{-1}]	[km s^{-1}]	[km s^{-1}]	[km s^{-1}]
2.5 - 5.0	12..45	17.38	12.18	15.09
5.0 - 7.5	11.62	13.66	11.38	13.71
7.5 - 10.0	11.72	13.55	10.76	12.64
10.0 - 12.5	11.29	12.87	10.53	12.31
12.5 - 15.0	11.16	12.71	10.37	11.67
15.0 - 17.5	10.84	12.17	10.30	11.43
17.5 - 20.0	11.08	12.48		
20.0 - 22.5	11.34	12.55		
22.5 - 25.0	11.47	12.67		

Table 4.3: Median and third quartile values, for every column density range, for the arms and interarms distributions of M 101 (cfr. Fig. 4.8).

Considering the contour plot of the interarms, the difference with that of NGC 6946 are even more pronounced. Indeed, the quartiles tend to increase with decreasing column density, whereas for the other galaxy we observed the opposite trend. We investigate possible causes of this behaviour starting from the presence of the big
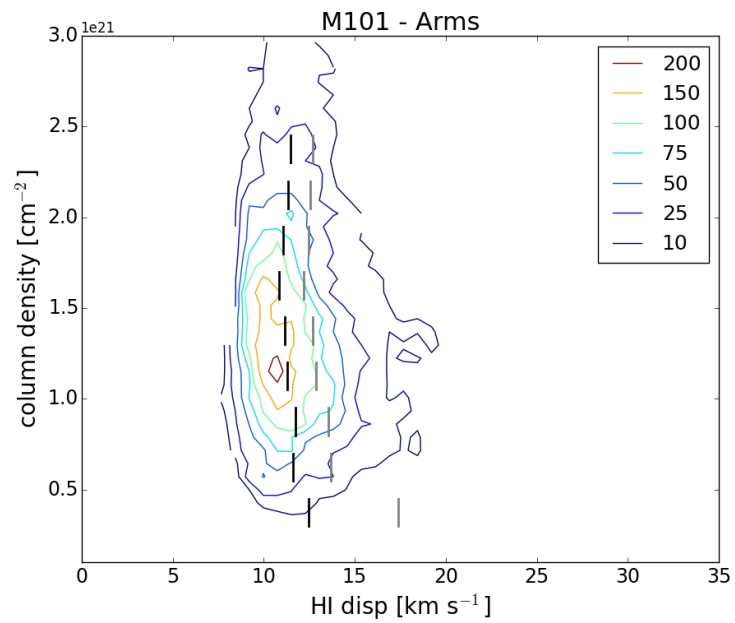
(a) Arms region
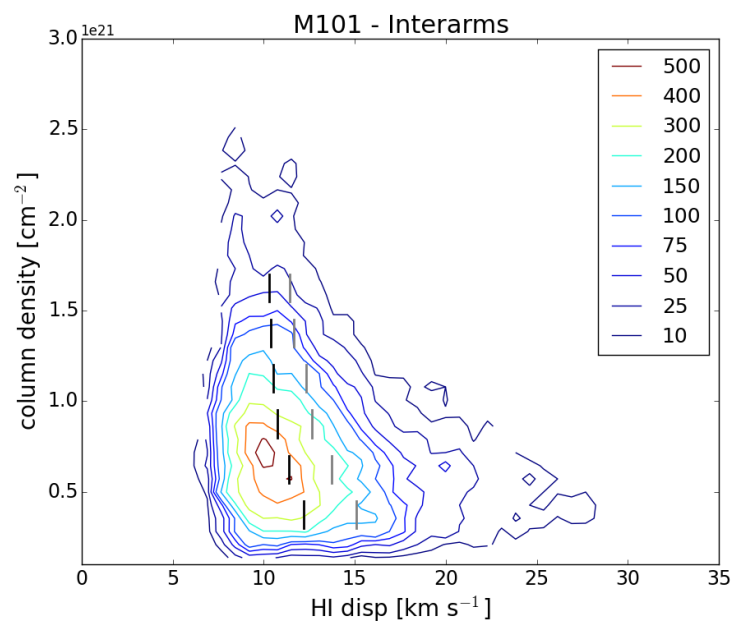
(b) Interarms region

Figure 4.8: As in Fig. 4.4, but for the galaxy M 101. Picture (a) is referred to the arms region, (b) to the interarms one.

HVC east to the centre of M 101. The impact with the HVC have produced indeed
a number of unusually broad profiles. Therefore, we produced contour plots for the
arm and interarm that lie opposite to cloud, with respect to the galaxy centre. The
quartile values relative to these contour plots exhibit the same shape and the same
trend than those in Fig. 4.8. This indicates that the relation between dispersion and
column density we observe in Fig. 4.8 are general throughout the galaxy. However, a
role of the HVC in this phenomenon is not ruled out, since we have seen (Sect. 2.5.1)
that the cloud influence the HI distribution of a great area of the disk. In particular
it could in some way produce the anomalous high column density measured in the
arm opposite from the centre to the HVC (Kamphuis, 1993). However, the dispersion
values in these regions do not present particular anomalies.

In Sect. 5.1 we will discuss the meaning of these findings, also considering the avail-
able literature.

4.2.3 Statistical analysis

To perform a statistically significant analysis of the contour plots just described,
we adopted the same procedure used for NGC 6946. We produced 1-D histograms of
M 101 dispersion values (of arms and interarms), we measured their quartiles, and
we compared the two samples through the K-S test.

The results are in Tab. 4.4.

	1st quartile [km s^{-1}]	Median [km s^{-1}]	3rd quartile [km s^{-1}]
Arms	9.76	10.89	12.48
Interarms	9.15	10.78	13.02
WITHOUT SELECTION ON THE PROFILES			
Arms	9.94	11.14	12.92
Interarms	9.39	11.12	13.71

Table 4.4: Statistical exam of the dispersion in M 101.

Outcomes are really similar between the two distributions. The greatest difference
is in the first quartile: $\sim + 0.6$ km s^{-1} for the arms. Since it is approximately the
5% of the measure, this difference is not particularly significant. The last interarm
quartile is instead $\sim + 0.5$ km s^{-1} higher.

As we did on NGC 6946, we calculated the quartiles for the data without any selection
on the profiles (see the bottom part of Tab. 4.4). The main difference in this case
is that the third quartile for interarms is $\sim + 0.8$ km s^{-1} higher than that of the

arms. This is because we are considering also the broad profiles that characterize the region of the HVC. The difference is not particularly significant, though, because we are averaging over all the interarms.

Relative to the K-S test (for a description see Sect. 4.1), we obtained D-value = 0.12, and this would that the two regions cannot be drawn from the same distribution. Probably this is a consequence of the significant difference visible for high widths. As for NGC 6946, this conclusion is opposite to what the quartiles test indicates.

Chapter 5

Discussion

In this Chapter we discuss the results of the analysis described so far. In particular, we compare our results with the state of art emerging from the available literature. In Sect. 5.1 we compare our velocity dispersion profiles with those obtained in previous studies. In Sect. 5.2 we finalise some points on the relation between dispersion and morphology deeply studied in Chap. 4. In Sect. 5.3 we focus on the mechanisms that could produce the broadening of the HI profiles in our data. In particular we try to figure out the importance of stellar feedback.

5.1 Dispersion profiles: comparison with previous studies

5.1.1 NGC 6946

The HI emission of NGC 6946 has been studied by several authors in the past decades. The most recent works which inspected the kinematic properties of the galaxy are Boulanger and Viallefond (1992), Kamphuis (1993), Boomsma (2007), Boomsma et al. (2008), Tamburro et al. (2009) and Ianjamasimanana et al. (2015), with increasing resolution and S/N. All these studies present velocity dispersion maps (derived through Gaussian fitting of the profiles), and measures of the radial profile of the dispersion. However, their discussion of these results is usually limited to the most evident aspects, since their interest is mainly on other topics. The dispersion profiles extracted in these works always exhibit a decrease from the centre to the outskirts of the galaxy, while less agreement is found on the actual values. Using old Westerbork data at $25''$ spatial and 10 km s^{-1} velocity resolution, Boulanger and

Viallefond (1992) found that the HI dispersion decreases from 19 km s^{-1} to 7 km s^{-1} at 17.5 kpc. Kamphuis (1993) fitted the spectra obtained with observations at 14$''$ spatial and 8.2 km s^{-1} velocity resolution, measuring 13 km s^{-1} in the centre and 6 km s^{-1} at 24 kpc. The best available observations of NGC 6946 are those of Boomsma (2007), Boomsma et al. (2008) which we also used. These data are characterized by a deeper integration time, and a better velocity resolution (4.2 km s^{-1}), with a beam of 13$''$. In Fig. 5.1 we show the dispersion profile obtained in this work which decreases from 13 km s^{-1} to 6 km s^{-1} at 22 kpc, therefore in complete agreement with Kamphuis (1993). The difference between these results and those of Boulanger and Viallefond (1992) is possibly due to beam-smearing effects (that are greater for larger beams). A role may also be played by the velocity resolution, which is worse in the oldest data.
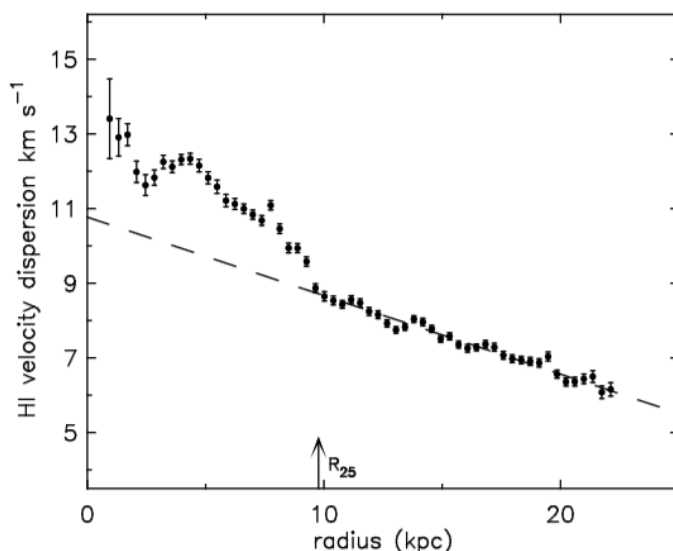
Figure 5.1: Fig. 6 from Boomsma et al. (2008): plot of the azimuthally averaged velocity dispersion of the HI in NGC 6946, as a function of radius. The dashed line shows the approximate linear trend of the profile in the outer disk extrapolated to smaller radii. The R$_{25}$ is indicated by the arrow.

The velocity dispersion map produced by us and shown in Fig. 3.1 exhibits average values that spans from 15 km s^{-1} (ignoring the innermost values) to 8 km s^{-1}. Comparing the general shape of the profiles, we can recognize the three main bumps identified by Boomsma et al. (2008) at R$\sim$2, 4 and 7.5 kpc, and the roughly linear decrease in the outskirts. Recalling that we used the same data of Boomsma et al. (2008), the different values that we measured may seem strange. Let us briefly discuss

this point. First of all, almost every point in our profile is consistent with those of
Boomsma et al. (2008), within our error bars. Boomsma et al. (2008) bars are much
smaller but we did not found any description on how they were determined. For sure,
we can exclude that their errors have have been derived in the same way tha ours
(the standard deviation of dispersion inside every annulus, see Sect. 3.1.1), since they
should be larger. Second, in the two studies, different choices on which profiles not to
consider were made. Boomsma (2007) points out that the dispersion of profiles with
double peaks and major wings were not used in his analysis. Although, he does not
specify how these features were selected. Comparing his dispersion map (Fig. 16 in
Chap. 2 of Boomsma (2007)) with our Fig. 2.14(a), we can notice that his selection
were more strict than ours. In particular, several pixels that in our map show high
dispersion values, are left blank in Boomsma (2007). This should likely justify the
systematic higher values we measured in our profile ($\sim +2$ km s^{-1}).

5.1.2 M 101

The deepest study on the kinematics of M 101 neutral hydrogen emission is that
performed by Kamphuis (1993). He used older Westerbork observations, consisting
of a mosaic of two single pointings (versus our five, see Sect. 2.1) with analogous
beam and velocity resolutions than us. The observations we used are characterized
by a longer integration time in the inner region of the galaxy (approximately the
area corresponding to the stellar disk).
Through Gaussian fitting of the spectra, Kamphuis (1993) produced a velocity dis-
persion map of the HI emission (Fig. 12 of Chap. 7 in his PhD Thesis), claiming
higher values in the arms than in the interarms (about 6-9 km s^{-1} of difference). We
report his dispersion profile in Fig. 5.2. From this plot he concluded that velocity
dispersion slightly decreases from 12 km s^{-1} to 8 km s^{-1}. Looking at his data, one
could note more precisely that, in the innermost region, the dispersion lies between
10 and 11 km s^{-1}, while at 6$'$ ($\sim$ 12 kpc) there is a peak at 12 km s^{-1}.
For what concerns the outer regions, we notice that Kamphuis (1993) profile reaches
radii beyond R=20$'$ ($\sim$ 40 kpc). Comparing his map with ours, we realized that, for
these large radii, just a few pixels are available for estimating the dispersion. Thus,
we are not particularly confident on the latest points in Fig. 5.2. Kamphuis (1993)
estimated the error on every point at $\pm$ 2 km s^{-1}. Excepted some peculiar regions
(e.g. the one corresponding to where the HVC lies), Kamphuis's dispersion values
are compatible with ours (cfr. Fig. 3.7.) Considering the standard deviations, our
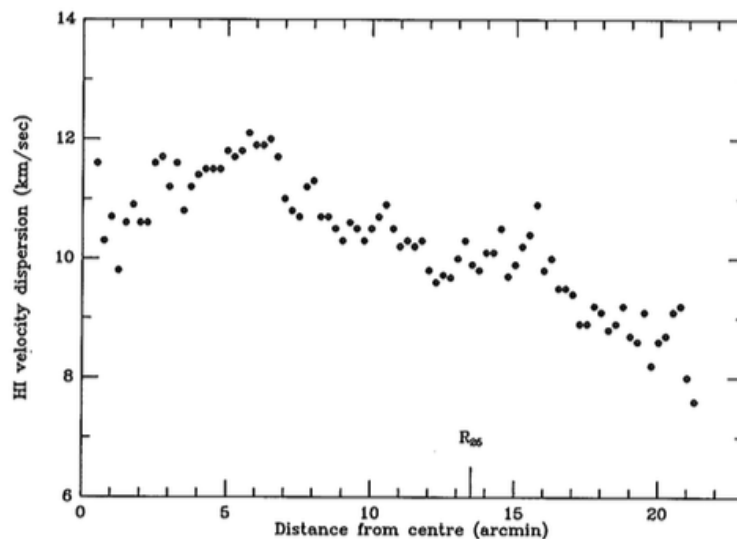
Figure 5.2: Fig. 13 from Chap. 7 in Kamphuis (1993): HI velocity dispersion profile of M 101. The azimuthal dispersion error is $\pm$ 2 km s^{-1}.

profile is in fact completely in agreement with that of Kamphuis (1993). In general, our values are a bit higher (not more than 1 km s^{-1}). This difference could be due to the different selection of the pixels to mask out. Comparing the dispersion maps, it is clearly visible that different selection criteria have been adopted.

In conclusion, we think that our result is compatible with that of Kamphuis (1993). The most striking feature of this profile is that it is really shallower than that of NGC 6946. Moreover, the values at low radii are smaller, and those at high radii are larger than those of the other galaxy. Indeed, a decrease is actually present in the outer parts, even though probably not as pronounced as claimed by Kamphuis (1993). Furthermore, in contrast with his work, we did not find clear differences between arms and interarms regions. We refer to Sect. 3.2.3 and 4.2 for a discussion on this.

Although most of the HI dispersion profiles exhibit negative trends with radius, other galaxies were found to have a roughly flat behaviour (as that of M 101looks like). The most clear example among these is probably NGC 3938 (van der Kruit and Shostak, 1982). Also NGC 1058, excluding the high dispersions in the innermost region, exhibits a flat trend at greater radii (Petric and Rupen, 2007). Ianjamasimanana et al. (2015) noticed also that dwarf galaxies usually show a flatter profile than spirals.

5.2 Expectations of a dispersion-arms correlation

The presence of a correlation between HI velocity dispersion and arms structure of the galaxies has seldom been investigated in the literature. Although, it is generally thought that the line profiles should be broader inside the arms, rather than in the regions among them. As said in Sect. 3.1.2 , this would be expected as a consequence of star formation, which happens mostly in the arms. Indeed, the feedback from stellar activity might be the main feeding mechanism of ISM turbulence. We have already mentioned that in his study of M 101 Kamphuis (1993) found a higher dispersion in the arms. Like most other studies, though, the focus was given to other features of HI kinematics. It is then possible that their conclusion on this point was not deeply pondered, nor experimentally justified.

Rare exceptions are the studies by Shostak and van der Kruit (1984) and van der Kruit and Shostak (1984). In their papers they present a thorough analysis of the neutral hydrogen emission of the spiral galaxies NGC 628 and NGC 1058. An entire section is dedicated to the gas velocity dispersion, and to understand if the latter correlates with the surface density. In NGC 628 they found $\sigma_{\mathrm{disp}} \sim 10$ km s^{-1} in the arms and $\sigma_{\mathrm{disp}} \sim 7$ km s^{-1} in the interarms. In Fig. 5.3(a) we show a plot from their paper that provides the best evidence of this. Similarly to our "contour plots" (Sect. 4.1.2 and 4.2.2), the area of each symbol is proportional to the number of profiles that fall in the corresponding region of the plane. The horizontal bars are the medians of the dispersion distribution at fixed column density. Considering that $N_{\mathrm{HI}} > 10^{21}$ cm^{-2} approximately corresponds to the spiral arms, they concluded that there dispersion is higher than in the interarms, (which are characterized by lower column densities). Performing the same analysis on NGC 1058 (van der Kruit and Shostak, 1984), though, they found a median value of the dispersion constant with the column density (Fig. 5.3(b)). In this plot, N_{HI} values are lower than in NGC 628, because the latter is richer in HI by almost an order of magnitude in solar masses units (considering total HI mass, cfr. Petric and Rupen (2007) and Kamphuis and Briggs (1992)).

Furthermore, the analysis of NGC 628 by Shostak and van der Kruit (1984) is limited to R < 4.25′ (~ 12.3 kpc, assuming a distance of D = 18 Mpc), where the HI spiral pattern is really confuse (for a comparison, look at the inner region of the total HI map of NGC 6946, Fig. 3.4(a)). Moreover, this region is contained within $R_{25} \sim$ 15 kpc (Kennicutt et al., 2003), then the plot in Fig. 5.3(a) is obtained using data

from a region with strong star formation. On the contrary, NGC 1058 has $R_{25} \sim 4.4$ kpc (de Vaucouleurs et al., 1991), then Fig. 5.3(b) refers to an area where few stars should be forming. This difference is not mentioned by the authors, while it could be a reason of the contrasting behaviour exhibited by the two galaxies.

Their results on NGC 628 appear similar to what we found for the relation between dispersion and column density in NGC 6946 (Fig. 4.4). Although, we have seen in Sect. 4.1.3 and Sect. 4.2.3 that dispersion median values does not differ significantly between arms and interarms.

At this point it is important to notice that our analysis was based on a different strategy then that of Shostak and van der Kruit (1984) and van der Kruit and Shostak (1984). Indeed, these authors plotted all the data between R = 1.5′ and R = 4.25′ in a unique plot, using a threshold column density to distinguish between arms and interarms. Differently (see Sect. 3.1.2 and 3.2.2), we preferred to use a morphological criterion, and to consider not only HI emission, but also UV images to trace the arms. Since arms does not always exhibit a continuous shape - in terms of HI emission - in our method could be considered low S/N profiles as part of their masks. The opposite should happen for the interarms. We think that, if one wants to look for a difference between dispersion values in the arms and the interarms, our method is more appropriate.

Considering the contour plots we produced in Fig. 4.4 for NGC 6946 (analogous to those by Shostak and van der Kruit (1984) and van der Kruit and Shostak (1984)), we notice a trend similar to theirs. However, our analysis also indicates that, *both inside the arms and the interarms regions*, the velocity dispersion shows a trend that increases with the column density. This would sensibly correct their conclusion - not based on morphology but on a density criterion - that dispersion *is higher* in the arms. It is more correct to say that it is generally higher for higher column densities. It is important to remind the reader that for M 101 we observed a further different behaviour. There, the dispersion is about constant with column density (in the arms), while it grows for decreasing density in the interarms (Fig. 4.8). Also, at low column densities we found higher average dispersion than in NGC 6946 (compare in particular Fig. 4.4 with Fig. 4.8(b)). We discussed in the text these results. We think that they might reflect the different behaviour of the dispersion vs. radius in the two galaxies. Indeed, while NGC 6946 has in the outskirts low column density gas with low dispersion, M 101 does not have many profiles of this type, since the dispersion is flatter. Moreover, they could be in some way related to the perturbation that

the phenomenon that produced the HVC induced on M 101 gaseous disk (see Sect. 4.2.3).

The HI velocity dispersion of NGC 1058 has been studied in detail also in a more recent work by Petric and Rupen (2007), with four times better velocity resolution than van der Kruit and Shostak (1984). Confirming what previously noticed by them, they concluded that no correlation is present between velocity dispersion and gaseous spiral arms nor star formation regions. Moreover, they observed that the broadest profiles are located preferentially in the interarms region. This finding echoes what we observed in our galaxies, especially in NGC 6946 (see for instance Fig. 4.1). Also Shostak and van der Kruit (1984) and van der Kruit and Shostak (1984) seem to have found something similar (look at the dispersion profiles referred to their P-V diagrams in Fig. 8, in both papers), but they did not discuss it.

A conclusion that we could draw is that there is a tendency for broad line profiles to be located is usually in the regions between the arms. This is observed by us in NGC 6946 (Sect. 4.1) and - less clearly - in some regions of M 101 (Sect. 4.2). Petric and Rupen (2007) observed the same in NGC 1058. Also van Eymeren et al. (2009) noticed something similar in the dwarf galaxy NGC 2366. Although these results could indicate a common feature in the HI velocity dispersion of all galaxies, it is not clear if they are related to any physical property of the neutral medium. The other main result that emerges from this section is the deep difference present between our two galaxies. In particular, it is interesting that M 101 exhibits significantly higher dispersion values at low densities. It is suggestive to interpret these outcomes in terms of different origins of the turbulence in the two disks. Indeed, in M 101 we may see the effect of the HVC as a driver of turbulent motions. We realized the same study considering the region of M 101 opposite to the HVC (respect to the centre), and we obtained an analogous behaviour. This may be an indication that the HVC is producing a perturbation of the whole galactic disk, as already speculated by Kamphuis (1993).

5.2.1   A comparison with a simulated study

A recent paper by Khoperskov and Bertin (2015) presented synthetic HI observations of spiral galaxies, focusing on the outer disk properties and its temporal evolution. They present several results of their simulation, which can be compared with observations. In particular, they calculated the synthetic spectra of the neutral hydrogen emission for a simulated galaxy inclined at an angle of 30°. Reminding that
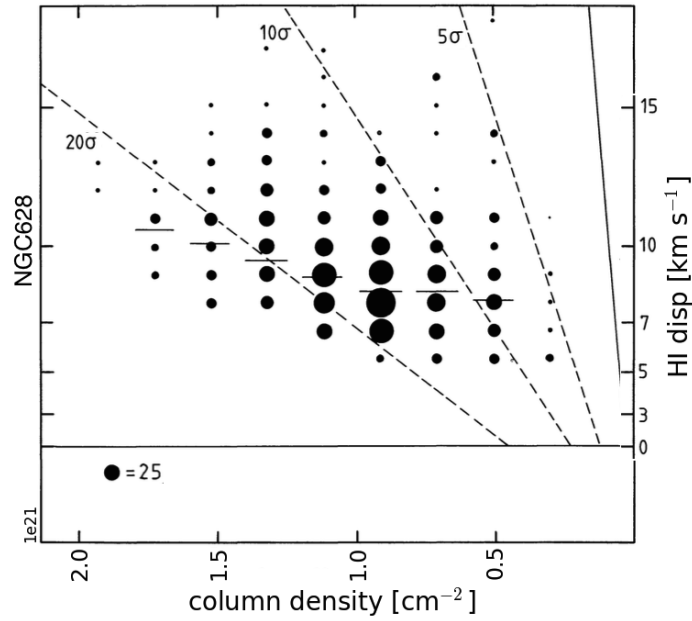
(a) NGC 628
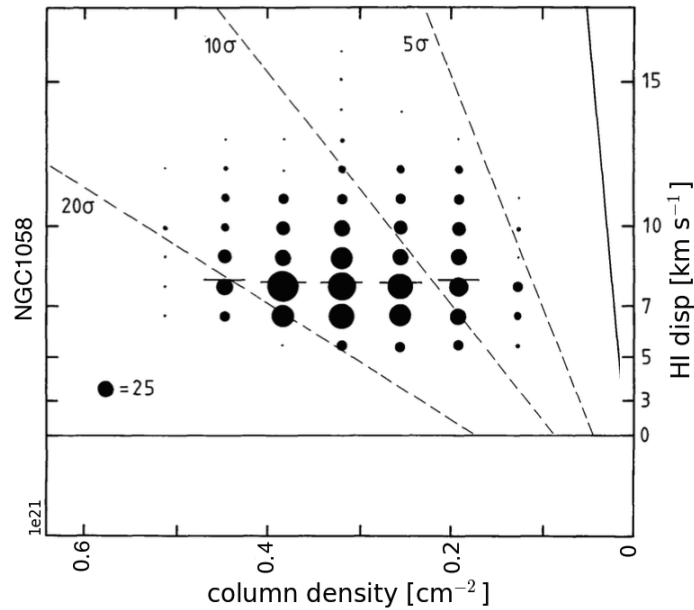
(b) NGC 1058

Figure 5.3: HI column density vs. velocity dispersion as studied by Shostak and van der Kruit (1984) in NGC 628 (**top**) and van der Kruit and Shostak (1984) in NGC 1058 (**bottom**). The area of each circle is proportional to the number of profiles that fall in the corresponding region of the plane. Horizontal black bars are the medians of the dispersion distributions at fixed column densities. (a) Fig. 11 from Shostak and van der Kruit (1984), relative to the inner region of NGC 628 (4.4 kpc < R < 12.3 kpc), inside R_{25}. Shostak and van der Kruit (1984) indicate $N_{HI} = 10^{21}$ as the separation between arms and interarms. (b) Fig. 11 from the study of NGC 1058 by van der Kruit and Shostak (1984). The data are also taken from the region 4.4 kpc < R < 12.3 kpc), that is outside R_{25}. The median values of dispersion are constant with density.

NGC 6946 has i=38° and M 101 has i=28°, it is legitimate to draw a comparison between our data and their results.

One of the outcomes of their simulations is that in the arm regions profiles are expected to be broader than in the region between them ($\gtrsim$10 km s^{-1} versus $\lesssim$5 km s^{-1}, see Fig. 4 in their paper). It is important to notice that in their simulation they does not consider the effect of star formation. In this thesis we did not find a clear distinction in the width of the profiles coming from the arms with respect to that from the interarms, certainly not at the level predicted by these simulations. On the contrary, we found many low density regions which exhibit particularly broad profiles (cfr. Sect. 4.1.2 and Sect-4.1.2). If these features will be confirmed as a general property of the neutral medium in the galaxies, it may indicate that the stellar activity is important for produce the measured gas dispersions (since they have neglected its feedback). As a consequence the simulations would need improvement to describe the HI emission of the disks. However it would also be important to analyse such simulations with the same techniques used for observational data.

5.3   Origin of turbulence in the outer disks

In this section we try to recap all our results and focus on the *origin* of the broadening of the profiles in the outermost regions of the gaseous disks. In particular we discuss whether the energy input from star formation processes can cause turbulence in the ISM.

We follow an empirical approach, looking for a correlation between star formation rate density and HI dispersion. Doing this we are guided by both theoretical and observational argumentations, since stellar feedback is indicated as the main driver of gas turbulence in many works (see the related references indicated in Sect. 1.3, where we also report the other causes of turbulence proposed in the literature).

A way to directly test these possibilities is to calculate the energy input that should come from the proposed physical processes, and to compare them with the energy required by the observed line widths. Hydrodynamical or magneto-hydrodynamical simulations have also been attempted to shed light on the problem.

A recent paper by Krumholz and Burkhart (2015) provides the analytical predictions of the expected star formation rates in a disk where turbulence is driven by gravitational instability or by stellar feedback. Testing their predictions with observational data from the literature, they find that both mechanisms are positively

correlated with ISM velocity dispersions. However, the two trends are different: for the feedback-driven turbulence they obtained SFR $\propto \sigma^2$, while for the gravity-driven one they get SFR $\propto f_{gas}^2 \sigma$ (where f_{gas}^2 is the gas fraction in the galactic midplane). Thus, if the stellar activity is the main regulator of the ISM turbulence, this would result in a steeper rising of the velocity dispersion with the SFR. Subsequently, they compare their models to a collection of data from the literature. Their conclusion is that data with high dispersions ($\gtrsim 50$ km s^{-1}) and moderate star formation rates ($\gtrsim 10$ M$_\odot$ yr^{-1}) are compatible with a gravity-driven turbulence and not with a feedback-driven one. However, data with these characteristics are mostly referred to galaxies at z $\gtrsim 1$, where the resolution is limited and the beam smearing might produce a significant artificial broadening of the profiles (see Sect. 4.2 in their paper). In any case, their strategy cannot work for our galaxies. Indeed, almost every profile in our sample is lower than 30 km s^{-1}. For these values, following Krumholz and Burkhart (2015), we cannot discriminate between the two models (see Fig. 1 in their paper).

In our analysis, we focus on the role of stellar feedback, its relation with dispersion and the differences between the two galaxies on these points.

5.3.1   Star formation rate density: a comparison

A very interesting comparison that can be done between NGC 6946 and M 101 is relative to the radial dispersion profiles. Just having a look at the two plots in Fig. 3.1 and in Fig. 3.7 we realize that their trends are very different: NGC 6946 shows a monotonic decline from ∼15 kpc to ∼8 kpc, while M 101's profile is approximatively flat from the centre to the outer galaxy. In addition to this, M 101 values are lower than those of NGC 6946 in the inner regions, but higher in the outskirts, as already pointed out.
We discussed in Sect. 3.1.1 and 3.2.1 possible links between dispersion profiles and star formation. A particularly interesting parameter is the Star Formation Rate surface Density (herafter Σ_{SFR}). We estimated its average value as:

$$\Sigma_{\text{SFR}} = \frac{\text{SFR}}{\pi R_{25}^2} [\text{M}_\odot \text{ yr}^{-1} \text{ kpc}^{-2}] \qquad (5.1)$$

where SFR is the Star Formation Rate in M$_\odot$ yr^{-1} and R$_{25}$ the radius correspondent to mag=25 in B-band (Tab. 2.1 and Tab. 2.3). For the SFR we used 4 $M_\odot$ yr^{-1} for NGC 6946 (Sauty et al., 1998), and 2 M$_\odot$ yr^{-1} for M 101 (Lanz et al., 2013). We

obtained:

$$\Sigma_{\text{SFR}}(\text{NGC 6946}) = 1.3 \times 10^{-2} \text{ M}_\odot \text{ yr}^{-1} \text{ kpc}^{-2}$$

$$\Sigma_{\text{SFR}}(\text{M101}) = 2.4 \times 10^{-3} \text{ M}_\odot \text{ yr}^{-1} \text{ kpc}^{-2}$$

Could this large difference in star formation rate density (more than a factor 5) be in some way related to the different shapes of the two galaxies dispersion profiles? To check this possibility we proceed to study the Σ_{SFR} profiles of the galaxies.

5.3.2 Star formation rate density profiles

To produce the Σ_{SFR} profiles of our galaxies we followed the method described in Bigiel et al. (2008). They used Galex FUV emission maps, combined with 24 μm emission maps obtained with by the MIPS instrument of the Spitzer satellite. Tracing mostly the light coming from O and B stars, FUV images give a picture of the recent star formation in a galaxy. However, a great part of this emission is obscured by dust, and reradiated in the Mid/Far Infrared. The 24 μm images are therefore used to estimate how much of the young star radiation has been absorbed by dust. The formula proposed in Bigiel et al. (2008) is the following:

$$\Sigma_{\text{SFR}}[\text{M}_\odot \text{ Gyr}^{-1} \text{ pc}^{-2}] = 3.2 \times I_{24}[\text{MJy sr}^{-1}] + 81 \times I_{\text{FUV}}[\text{MJy sr}^{-1}] \qquad (5.2)$$

where I_{24} is the 24 μm intensity and I_{FUV} the FUV intensity. The coefficients used in Eq. 5.2 come from the study of Leroy et al. (2008). We employed this calibration to calculate Σ_{SFR} on local scales of 750 pc. Although the spatial resolution of both the FUV and the 24 μm maps is higher, it is generally preferred to calculate local star formation rate densities on surfaces that include multiple star forming region. In this way indeed, the Σ_{SFR} can be assumed constant over the relevant timescales of the SFR indicators that we are using (Calzetti, 2013). Thus, we convolved both the FUV and 24 μm maps with a gaussian beam, degrading them to a common spatial resolution of 750 pc.

Fig. 5.4 shows the star formation rate density profiles we produced for NGC 6946 and M 101. These ones were realized considering the galaxy on their whole, and not only the regions we selected in the dispersion maps.

For NGC 6946 we plotted also the Σ_{SFR} profile from Muñoz-Mateos et al. (2009). This was also obtained using FUV observations corrected with 24 μm emission, but with a different calibration. The profiles are compatible at 1σ considering our er-

ror bars, but not if we consider their ones. Although, the errors are derived in a different way. These authors considered the uncertainties in the incident flux per pixel (estimated assuming Poissonian statistics) and in the sky level measurement (Muñoz-Mateos et al., 2009). We preferred to use the average RMS of the Σ_{SFR} map of each annulus from which we extracted the profile. This kind of uncertainties are obviously larger. The last point in each plot is an upper limit due to the detection limit of the instruments. We measured a limit of 0.30 $M_\odot$ Gyr^{-1} pc^{-2} for NGC 6946 , and of 0.26 $M_\odot$ Gyr^{-1} pc^{-2} for M 101.

Both profiles show a monotonic decline from the inner to the outer regions of the galaxies, which is steeper for NGC 6946. This galaxy exhibits in fact a very strong star formation activity, especially in the innermost regions. This should be due to the large accumulation of molecular gas in the centre, as pointed out by Crosthwaite and Turner (2007).

The black line superimposed on the profiles indicates the azimuthal velocity dispersion profile of the neutral hydrogen (Sect. 3.1.1 and 3.2.1). In NGC 6946, the dispersion and Σ_{SFR} profiles exhibit a very similar trend. This might suggest a correlation between high dispersions and regions of strong star formation. Although, the plot of M 101 does not show an analogous behaviour: as the Σ_{SFR} profile declines, the HI dispersion remains approximatively constant out to the galaxy's outskirts. This could be an indication that stellar feedback is not the main responsible of the broadening of the HI profiles in the outer disk of M 101. But how can we explain the apparently different behaviour of NGC 6946?

5.3.3 Kinetic energy and stellar feedback: the azimuthal trend

To further investigate the role of stellar feedback in the feeding of turbulence, we studied the relation between the star formation rate density and the **kinetic energy density** of the neutral hydrogen. Here we multiply the one-dimensional component $\Sigma_{HI}\sigma_{HI}{}^2$ by the factor $\frac{3}{2}$ to take into account the three velocity components (assuming that velocity dispersion is isotropic). It is important to note that the resulting quantity is not the kinetic energy of the whole gaseous component of the galaxy, but just of the HI.

The kinetic energy measured from the line widths generally consist of the sum of a **turbulent** and a **thermal** component:

$$E_{kin} = E_{ther} + E_{turb}$$
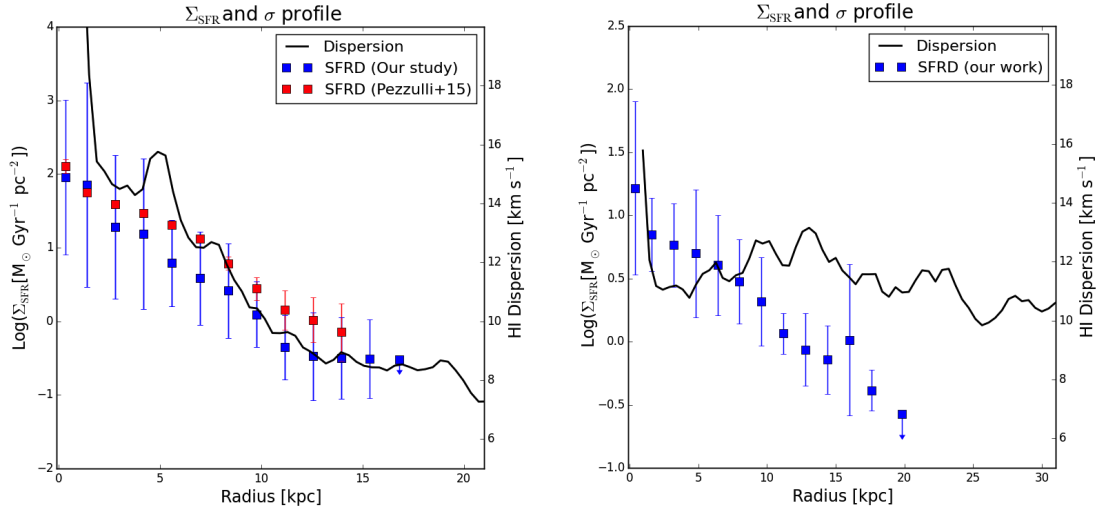
Figure 5.4: Azimuthal $\Sigma_{\text{SFR}}(R)$ profile calculated using the FUV emission corrected for the dust absorption at 24 μm. The **left** panel is the study for NGC 6946, the **right** one is that for M 101. The red points on the left are from the work of **?**, while blue ones come from our study. The solid black lines are the HI dispersion profiles.

where with E we indicate the kinetic energy per unit surface. If thermal broadening is much less effective than turbulence, we have $E_{\text{kin}} \sim E_{\text{turb}}$.

Following the approach of Tamburro et al. (2009), if we assume a steady state equilibrium between the kinetic energy input rate from the SNe to the ISM and the kinetic energy dissipation rate of it through turbulence, we obtain:

$$E_{\text{kin}} = \epsilon_{\text{SN}} \, \dot{E} \, \tau_{\text{SN}} \tag{5.3}$$

where ϵ_{SN} is the fraction of SN energy that is effectively turned into turbulent energy, $\dot{E}$ is the SN energy rate per unit surface, τ_{diss} the timescale of dissipation of the SN driven turbulence. $\dot{E}$ can be estimated from the SN rate per unit surface Σ_{SNR}, which depends on the fraction f_{SN} of all recently formed stars that explode as core-collapse SNae:

$$\Sigma_{\text{SNR}} = \frac{SFR}{<m>} \times f_{\text{SN}} \tag{5.4}$$

where $<m>$ is the average mass of stars of the population. As first estimate we approximate the values suggested by Tamburro et al. (2009), hence: $\tau_{\text{SN}} \sim 10^7$ yr, $f_{\text{SN}}/<m> \sim 10^{-2} \; M_{\text{odot}}^{-1}$. Finally, we consider $E_{\text{SN}} = 10^{51}$erg as the energy released by a SN explosion. Tamburro et al. (2009) estimated that the SN rate calculated in this way is characterized by an uncertainty of a factor $\sim 1/3$, depending

on the adopted assumptions.

Given the above, we obtain a kinetic energy density per unit surface of:

$$\frac{E_{\mathrm{kin}}}{[\mathrm{M}_\odot\ \mathrm{km}^2\ \mathrm{s}^{-2}\ \mathrm{pc}^{-2}]} = 5000 \times \epsilon_{\mathrm{SN}}\ \frac{\Sigma_{\mathrm{SFR}}}{[\mathrm{M}_\odot\ \mathrm{Gyr}^{-1}\ \mathrm{pc}^{-2}]} \qquad (5.5)$$

This formula provides a theoretical estimate of the kinetic energy supplied to the ISM by stellar feedback within a turbulent decay timescale. Thus, we can compare this calculation with the kinetic energy density measured from the HI line widths as a function of the star formation rate density (calculated through Eq. (5.2)).

In Fig. 5.5 we show the azimuthal trends of this (log-log) relation for NGC 6946 and M 101 , respectively.

For NGC 6946 we include both our measure of Σ_{SFR} and that showed in Muñoz-Mateos et al. (2009). In both cases, the data exhibit a good linear correlation. For the data from Muñoz-Mateos et al. (2009) we measured a linear correlation coefficient (usually called "coefficient of determination") $r^2 = 0.97$, while for our we calculated $r^2 = 0.92$.

The overplotted solid magenta line indicates the theoretical estimate of the SN energy input as a function of SFR (Eq. (5.5)). In the plot we assumed a constant ϵ_{SN}=0.1. Although all our data (blue points) are compatible with the theoretical estimate (considering the error bars), for high star formation rate densities and kinetic energies (that correspond to the inner regions of NGC 6946) the line seem to overestimate the data. The opposite happens for low values (the outer regions). We will discuss this trend in the next section.

About M 101, the relation between the two quantities looks completely different, and in total disagreement with the theoretical estimate coming from SN feedback (magenta line, with ϵ_{SN}=0.1). In particular, the inner region (at high Σ_{SFR}) presents slightly lower kinetic energies than the more peripheral area, where E_{kin} looks approximatively constant. This result is not just a consequence of the anomalous flat dispersion profile of the galaxy, but it is also due to the HI surface brightness, that is lower in the centre of the galaxy than in the bright arms region at higher radii.

At this point, it is important to note that - out to the inner 8-10 kpc - M 101 shows an asymmetric pattern that is evident in both the FUV and 24 μm images. Therefore, an azimuthal profile is probably not ideal to quantify the value of the Σ_{SFR} in a determined region. The next step we performed then, is to study the *local*
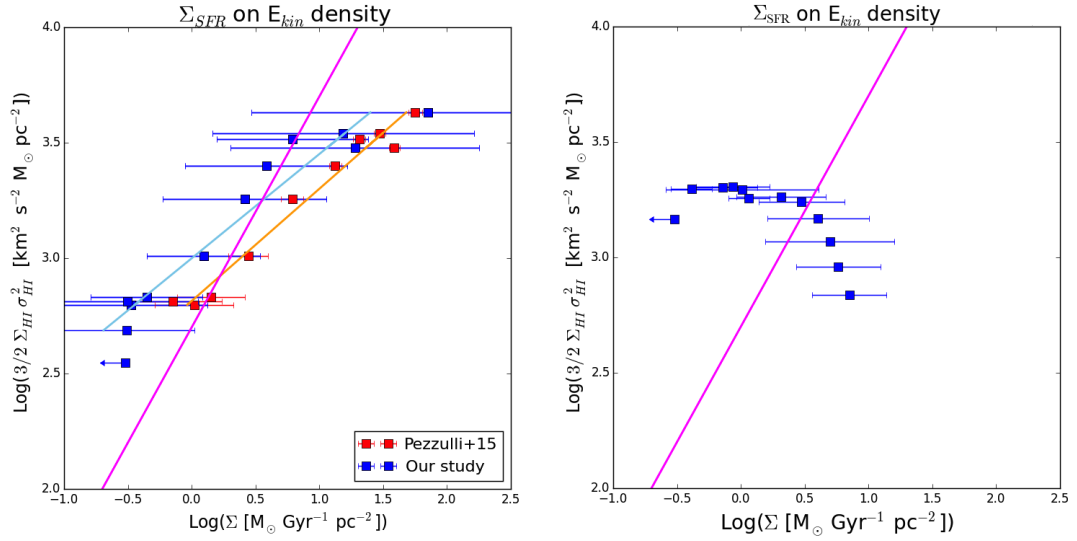
Figure 5.5: Kinetic energy of the HI gas ($E_{\mathrm{kin,\ HI}}$) vs./ the star formation rate density. On the **left** panel we show the study of NGC 6946, while on the **right** that of M 101. The points come from azimuthal averages on annuli of R=46". The solid magenta line of unity slope indicates a theoretical estimate of the SN feedback-driven turbulence, assuming an efficiency ϵ_{SN}=0.1 (see Sect. 5.3.3)

correlation between dispersion and star formation rate density.

5.3.4   Kinetic energy and stellar feedback: the local trend

Having produced the Σ_{SFR} maps of our galaxies, it is straightforward to realize a pixel-by-pixel study of the relation between the star formation rate density and the neutral hydrogen kinetic energy (derived from the HI line widths).

NGC 6946 -   In the top-left panel of Fig. 5.6 we show this relation for the whole galaxy in a contour plot. The general trend is similar to that of the azimuthal average, with the values with the highest kinetic energy showing the strongest star formation rate density. However, this way of plotting gives us a deeper insight on the galactic properties, and the local differences within the disk.

It is interesting to compare the data with the estimate coming from the SN feedback (Eq. (5.5)). We overplotted with solid magenta lines those with ϵ_{SN}=0.1 and with ϵ_{SN}=0.3. The innermost regions of the galaxy (with higher Σ_{SFR} and $E_{\mathrm{kin,\ HI}}$) lie below the ϵ_{SN}=0.1 line. This means that they would require a lower SN efficiency. Tamburro et al. (2009) noticed that the correlation with a constant ϵ_{SN} efficiency becomes better if we consider the total (atomic + molecular) kinetic energy of the
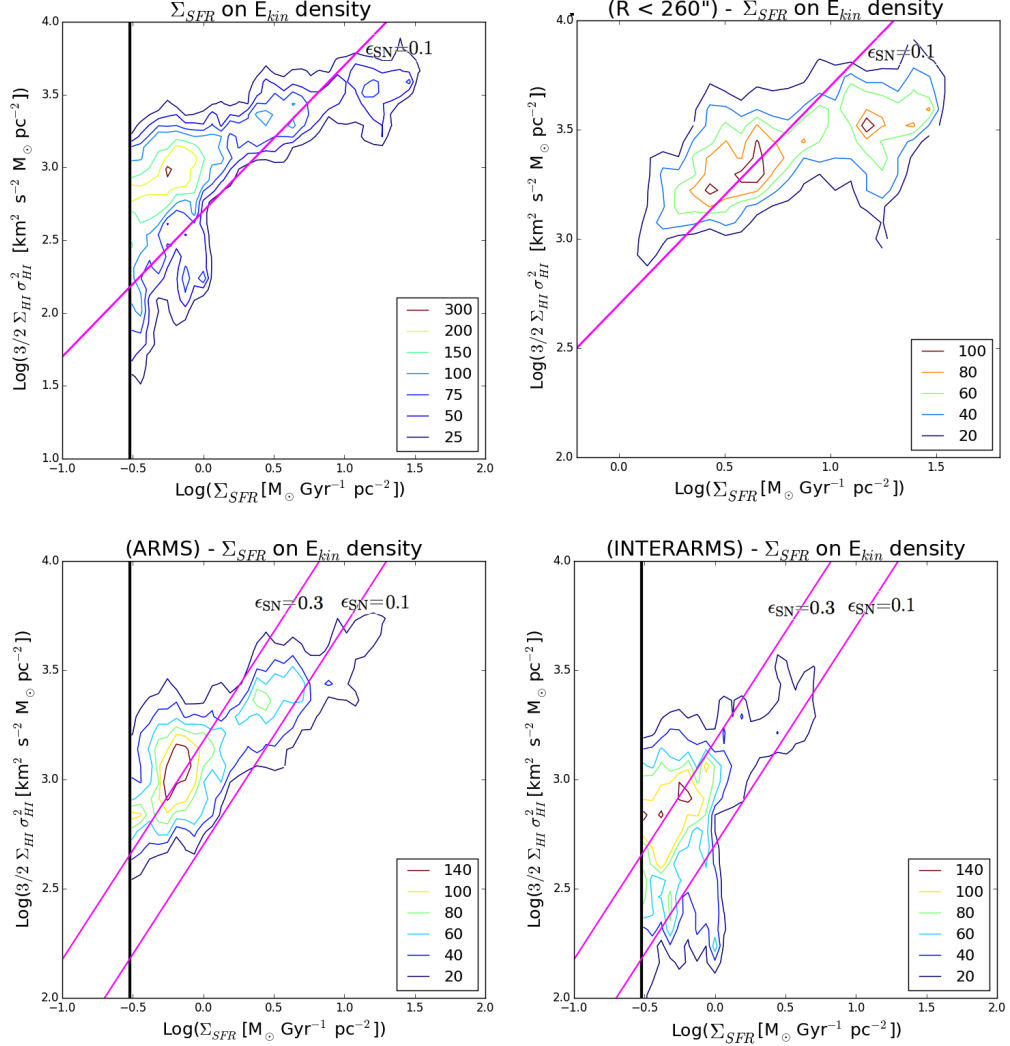
Figure 5.6: Study of the relation between star formation rate density (Σ_{SFR}) and HI velocity dispersion in NGC 6946. **Top-left:** Pixel by pixel contour plot of $E_{\text{kin, HI}}$ vs. Σ_{SFR} for the whole galaxy. The contours indicate the number density of the points falling in the correspondent region of this plane. The black vertical line indicates the noise level of the Σ_{SFR} map. The noise level for the kinetic energy is outside the box. The solid magenta line of unity slope indicates a theoretical estimate of the SN feedback-driven turbulence, assuming an efficiency $\epsilon_{\text{SN}}{=}0.1$ (see Sect. 5.3.3). **Top-right:** The same but for the inner region (R<260"), where there is the strongest star formation. **Bottom:** Same contour plot for the arms region (**left**), and for the interarms region (**right**). The solid magenta line at the highest values is calculated for $\epsilon_{\text{SN}}{=}0.3$, while the lower is for $\epsilon_{\text{SN}}{=}0.1$.

gas (see Fig. 4 of their paper). This may be particularly true for NGC 6946, which has a high density of H_2 in the centre (Crosthwaite and Turner, 2007). The top-right plot in the panel represents an equivalent study of the region of NGC 6946 inside R=260" ($\sim R_{25}$). As we mentioned, this area exhibits the strongest star formation rate density in the disk (Sect. 3.1.1). Here the correlation between the two quantities appears particularly good (although at a slightly different slope than that predicted by a constant ϵ_{SN}). The scatter in the kinetic energy is of a factor ~ 3 at the lowest contours.

Considering again the plot referred to the galaxy as a whole (top-left panel), if we move towards lower star formation rate densities (therefore, in the outskirts), the scatter in the kinetic energy increases a lot, being roughly of a factor 30 at the Σ_{SFR} noise level (considering the lowest contours). This scatter may be largely observational.

In the attempt to understand at what locations of the disk correspond the various regions in the plot, we realized analogous studies for the arms and interarms regions (respectively, the bottom-left and the bottom-right panels of Fig. 5.7). To define these we used the usual masks described in Sect. 3.1.2. We found that the arms dispose themselves on a correlation that looks inclined like that of the inner disk, while the interarms are much more scattered at various energies. The data referred to the arms (but the same could be said for the maxima of the interarms distribution) would be consistent with a linear correlation between E_{kin} and Σ_{SFR}, assuming a varying ϵ_{SN}. The SN efficiency should be higher in the outer than in the inner regions of the galaxy, and this may sound unexpected. For this reason, Tamburro et al. (2009) proposed that the turbulence in the outermost regions of galaxies could be feed by the energy produced by magneto-rotational instabilities that could occur in the disk. A discussion on this possibility (or on the many other mechanism proposed in the literature for the feeding of the gas turbulence) goes beyond the aim of the present work.

We also performed the same study eliminating the arms/interarms regions that are at R<260". We found an analogous behaviour, even though - as expected - the Σ_{SFR} reaches lower values (we do not report these plots). Anyhow, we think that it is very interesting that the interarms plot *includes* most of the kinetic energy values that are measured in the arms plot. This indicates that in the interarms, where the star formation is almost absent (completely absent in the outer disk), the kinetic energy assumes similar values than in the arms. This can seem a bit surprising

admitting a picture where the observed line widths are produced by SN-feedback driven turbulence.

Relatively to these arms/interarms plots, it is due to say that the FUV and 24μm maps on which we calculated the Σ_{SFR} are very near to the noise level in these regions. Hopefully, our choice of excluding points below three times the RMS noise is sufficient to avoid strong contaminations from the sky level.

M 101 - We perform an analogous study on M 101. The contour plot of the gas kinetic energy vs. the star formation rate density for the whole galaxy is reproduced in the top-left panel of Fig. 5.7. From this picture we can recognize the shape that emerged also from the azimuthal plot (top-right panel). The kinetic energy of the HI component looks roughly constant from the lowest to the highest Σ_{SFR}, although with a large scatter (around one order of magnitude). This behaviour, so different from that of NGC 6946, is largely due to the high dispersions measured in the outer regions of M 101. This might indicate that in these area the turbulence is driven by different causes, and we thought accretion the most likely (considering the presence of the HVC). Therefore we repeated the study completely excluding the region influenced by it. Surprisingly the resulting plot was almost identical to the previous one.

In the top-right panel we display the contour plot for the inner 260". We choose this region because beyond this radius the presence of the HVC starts to become relevant. What we found is completely different from the study of the inner region of NGC 6946 (centre-right panel of Fig. 5.6). Indeed the data are not aligned along any linear correlation. A visual inspection of a CO map (coming from the Heracles survey, Leroy et al. (2009)) shows a significant amount of molecular gas around the centre of the galaxy. Although, we judge that this would not be enough to put the inner region of M 101 on the linear correlation suggested by the SN-feedback driven turbulence (the magenta line in the plot). The 24 μm map shows a strong emission in this region (in particular if compared to the UV brightness), therefore the star formation rate density we calculated presents a strong dust correction there. A possibility is that that the calibration used to obtain the Σ_{SFR} (Eq. 5.2) fails in these circumstances.

We tried then to verify if, at least locally, the linear correlation seen in NGC 6946 and in the sample of galaxies studied by Tamburro et al. (2009) is present in M 101. Thus, we extracted the same contour plot for a region of the galaxy that is located
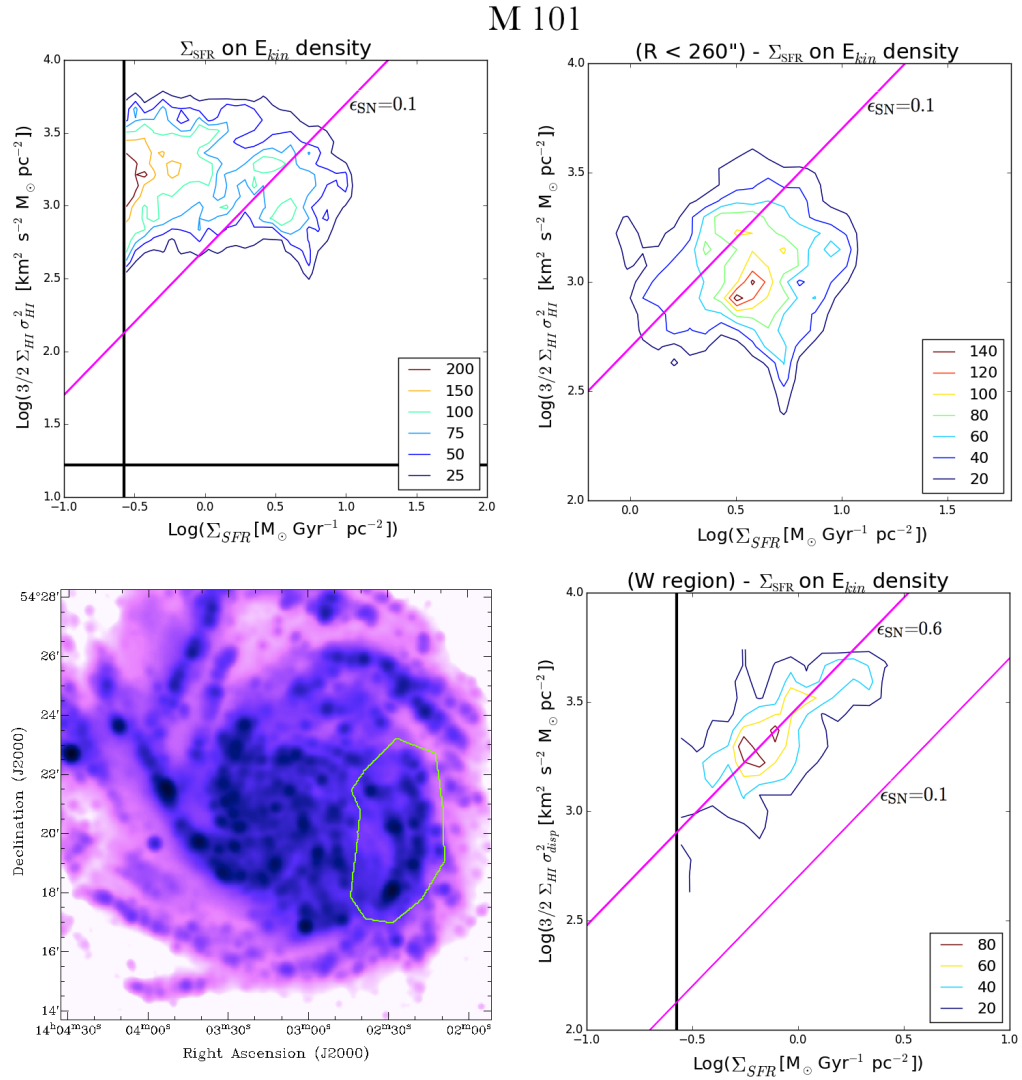
Figure 5.7: Study of the relation between star formation rate density (Σ_{SFR}) and HI velocity dispersion in M 101. **Top** plots: see description in Fig. 5.6. The solid magenta line is for stellar feedback with efficiency ϵ_{SN}=0.1. The two solid black lines in the centre-left panels indicate the noise level for both Σ_{SFR} (vertical) and gas kinetic energy (horizontal). **Bottom-left:** FUV image of the galaxy, smoothed to our working resolution of 750 pc. The brown contour delimitates the area from which we extracted the contour plot on the **bottom-right** panel. The arm in this area is a very strong star-forming region, as it is also evident from the 24μm map. In the bottom-right panel, the solid magenta line at higher values corresponds to ϵ_{SN}=0.6, the lower to ϵ_{SN}=0.1 as usual.

west to the centre. This area is contoured in the bottom-left panel of Fig. 5.7. It corresponds to an arm region that is particularly bright in HI, UV and 24 μm maps. We also included the nearby interarms. In this way we thought to be representative of a "normal" galactic area, far from both the HVC and the heavily dust-absorbed central part. Moreover, the high S/N of the FUV and the 24 μm maps in this region, assures us of the goodness of the Σ_{SFR} calculation.

The resulting contour plot is in the bottom-right panel of Fig. 5.7, where we see a linear correlation between the two plotted quantities, and the maxima looks in good agreement with a ϵ_{SN}=0.6. The 1-1 correlation visible in this area is particularly impressing. Although a SN efficiency of this entity would be a bit high, this result is very interesting. First of all it shows that the correlation between $E_{\mathrm{kin,\ HI}}$ and Σ_{SFR} is present in the some evident star forming regions of both NGC 6946 and M 101 (excluding the centre of the latter, where the high dust absorption makes difficult to measure the star formation rate density). Second, it gives further evidence that SN feedback is a very likely candidate to feed turbulence at least in the regions where stars are forming.

Chapter 6

Conclusions

6.1   Summary of the results

In this thesis we have studied the HI line emission of the two nearby galaxies
NGC 6946 and M 101. For the latter, we made use of new Westerbork observations,
never analysed before. Our goal was to shed new light on the physical origin of the
broadening of the line profiles, especially in the outermost regions of the HI disks.
To obtain this, we first performed precise measures of the velocity dispersion of the
neutral hydrogen component.
In the following, we briefly summarize the main outcomes of our work.

- We studied automatic methods to identify double-peaks and asymmetric pro-
  files (Sect. 2.5). These were both excluded from our subsequent analysis, for
  which we only considered profiles with single-gaussian shape. This choice was
  made in order to have line profiles we could assume to be broadened by thermal
  energy and/or *fully developed* turbulence, and not by transient pheonomena like
  superbubbles expansions (that might produce irregular shapes).
  Moreover, we executed a detailed comparison between the two main methods
  usually employed to measure the velocity dispersion of profiles: gaussian fit-
  ting and second moment. We found that the latter usually gives systematically
  lower values, in general underestimating the real line widths. We concluded
  that the gaussian fitting gives a better measures of the velocity dispersion (Sect.
  2.6.1).

- With the dispersion maps obtained from gaussian fitting, we extracted az-
  imuthally averaged velocity dispersion profiles of the two galaxies (Sect. 3.1.1

and 3.2.1). For NGC 6946 we derived a decreasing behaviour from ~ 15 km s^{-1} to ~ 8 km s^{-1}. This is slightly higher than that obtained by Boomsma et al. (2008), likely because they chose a different selection on the profiles. For M 101 we obtained a shallower profile, that in the centre has values of ~ 11 km s^{-1}, and in the outskirts decreases only to ~ 9 km s^{-1}.

- Producing appropriate masks, we studied the dispersion trends with radius in the spiral arm and interarm regions of the two galaxies (Sect. 3.1.3 and 3.2.3). In both cases, we could not notice any significant difference between the line profiles of arms and of the interarms.

- A visual inspection highlighted the presence of some high dispersion regions in the interarms of both galaxies (Sect. 4.1.1 and 4.2.1). Producing pixel-by-pixel contour plots, we inspected correlations of the dispersion vs. column density (N_{HI}) and line peak flux (Sect. 4.1.2 and 4.2.2). Considering both arms and interarms, we obtained a growing trend of the dispersion with N_{HI} for NGC 6946, while we found the opposite in M 101. This might reflect the different behaviour of the dispersion vs. radius in the two galaxies, i.e. steep in NGC 6946 and shallower in M 101 (Sect. 5.2).
The statistical analysis of the dispersion distributions is debatable (Sect. 4.1.3 and 4.2.3). On the one side, the comparison of the quartiles does not show a significant difference between arms and interarms. However, the Kolmogorov-Smirnov test suggests that, for both galaxies, the distributions cannot be drawn from a common one. All considered, our analysis significantly moderates the contention of a higher dispersion in the spiral arms, claimed both in observational (Shostak and van der Kruit, 1984; Kamphuis, 1993) and computational works (Khoperskov and Bertin, 2015).
The inner and the outer regions of the disk of NGC 6946 shows clear differences, indicating that in this galaxy the width of the profiles depends more on its distance from the centre than on its location in an arm rather than an interarm region.

- In the latest part of the thesis we studied the relation between the HI gas kinetic energy density and the star formation rate density (Σ_{SFR}), following an approach already suggested by Tamburro et al. (2009). To measure the Σ_{SFR} we used the FUV emission combined with that at 24 μm to account for dust extinction (Sect. 5.3.2). We studied the relation between Σ_{SFR} and the kinetic

energy both radially (Sect. 5.3.3) and locally (building pixel-by-pixel contour plots, see Sect. 5.3.4).

In NGC 6946 we found a good correlation between the two quantities, that approximatively agrees with a simple model of stellar feedback driven turbulence. Moreover, performing the same study in the arm and interarm regions, we showed that the correlation is present in both, although with higher scatter in the interarms.

In M 101 we obtained a flatter Σ_{SFR} profile. Considering the whole galaxy, we could not find a correlation between star formation rate and HI kinetic energy. This may indicate the need to also include the molecular (H_2) component in our analysis. However, M 101's behaviour can also be caused by strong dust absorption in its inner regions. Interestingly, considering the bright arm lying east to the nucleus, we found an excellent relation between the two quantities, indicating that in some localized areas our galaxies exhibit the same behaviour. In conclusion, this analysis suggests that the broadening of the HI profiles is in some way regulated, in addition to thermal energy, also by turbulent processes driven by stellar activity.

- As frequently noted in the text, the two galaxies that we studied in this thesis exhibit large differences. We think that several of them could be reconducted to the different dispersion radial profiles, in particular to the high dispersion values that M 101 shows out to its outskirts, where little star formation is present. But why these dissimilar trends of the dispersion? It is suggestive to interpret this in terms of different origins of the turbulence. While in NGC 6946 the contribution from the stellar feedback seems dominant, in the outer regions of M 101 we might be seeing the effect of other mechanisms. We think that the most likely is gas accretion or a merger event, that could have produced the HVC as well, and perturbed large portions of the galaxy disk.

6.2 Future perspectives

Further investigations should be conducted to make our conclusions more robust. Here, we point out those that we think are more promising:

- The dispersion maps in Figg. 2.14(a) and 2.15(a) show by eye a non-random pattern that presents a roughly spiral shape. This is even more evident in the

maps obtained before the clipping of the non-gaussian profiles. We first thought that this could suggest some correlation between the dispersion and the spiral structure in these galaxies. However, our study did not reveal a significant evidence for this. Despite that, there could exist correlations between the two quantities of different nature from the one we have looked for. In particular, depending from on typical time-scales of turbulent processes (triggering and decay), there could be a sort of delay between the stellar activity in the arms, and its effect in the gaseous disk. As a consequence, the broadest profiles might occur in the low column density regions of the interarms. This could also explain the tendency, observed in both galaxies, of the highest dispersions to belong to low S/N profiles.

- A further topic that would deserve a deeper analysis is the role of the HVC in the global kinematics of M 101. Indeed, even though its influence on the galaxy is evident and necessary to explain several of its peculiar features (from the HI density distribution to the flat dispersion profile), many mysteries are still unsolved, for instance its origin and its connection with the disturbances in the disk.

- The analysis that we performed in Sect. 5.3 to verify whether SN-feedback is a likely candidate to drive turbulent motions in the ISM needs improvements. In particular, the other components of the medium should be included in the measure of the gaseous kinetic energy of galaxies, starting from the molecular hydrogen (that exists in a significant fraction in the innermost regions).

- Another interesting test might concern the role of the thermal energy in the broadening of the profiles. We have already mentioned that some recent studies have shown that the WNM might be the dominant component of the neutral medium in the disk's outskirts (Pineda et al., 2013; Ianjamasimanana et al., 2015). It is suggestive that the thermal broadening expected for the WNM produces linewidths of $\sigma_{\mathrm{WNM}} \sim 8 \, \mathrm{km \, s^{-1}}$, which are similar to the typical values measured in the outer regions of galaxies. Thus, it would be interesting to check which fraction of WNM would be required to admit that the broadening of the HI is generated by this thermal contribution. This eventuality is particularly intriguing, for it would significantly diminish the importance of turbulence in the kinematics of the neutral medium in the outskirts of galaxies.

Bibliography

F. Bigiel, A. Leroy, F. Walter, E. Brinks, W. J. G. de Blok, B. Madore, and M. D. Thornley. The Star Formation Law in Nearby Galaxies on Sub-Kpc Scales. *Astronomical Journal*, 136:2846–2871, December 2008. doi: 10.1088/0004-6256/136/6/2846.

R. Boomsma. *The disk-halo connection in NGC 6946 and NGC 253*. PhD thesis, Kapteyn Astronomical Institute, University of Groningen, 2007.

R. Boomsma, T. A. Oosterloo, F. Fraternali, J. M. van der Hulst, and R. Sancisi. HI holes and high-velocity clouds in the spiral galaxy NGC 6946. *Astronomy and Astrophysics*, 490:555–570, November 2008. doi: 10.1051/0004-6361:200810120.

A. Bosma, W. M. Goss, and R. J. Allen. The giant spiral galaxy M101. VI - The large scale radial velocity field. *Astronomy and Astrophysics*, 93:106–112, January 1981.

F. Boulanger and F. Viallefond. Observational study of the spiral galaxy NGC 6946. I - H I and radio-continuum observations. *Astronomy and Astrophysics*, 266:37–56, December 1992.

J. N. Bregman. The galactic fountain of high-velocity clouds. *Astrophysical Journal*, 236:577–591, March 1980. doi: 10.1086/157776.

E. Brinks. The cool phase of the interstellar medium - Atomic gas. In H. A. Thronson, Jr. and J. M. Shull, editors, *The Interstellar Medium in Galaxies*, volume 161 of *Astrophysics and Space Science Library*, pages 39–65, 1990. doi: 10.1007/978-94-009-0595-5_3.

D. Calzetti. *Star Formation Rate Indicators*, page 419. October 2013.

C. Carignan, P. Charbonneau, F. Boulanger, and F. Viallefond. Observational study of the spiral galaxy NGC 6946. II - H I kinematics and mass distribution. *Astronomy and Astrophysics*, 234:43–52, August 1990.

W. N. Christiansen and J. V. Hindman. Cable to the editor. *Nature*, 167:358, September 1951. doi: 10.1038/167635a0.

C. Clarke and B. Carswell. *Principles of Astrophysical Fluid Dynamics*. Cambridge University Press, January 2014.

L. P. Crosthwaite and J. L. Turner. CO(1-0), CO(2-1), and Neutral Gas in NGC 6946: Molecular Gas in a Late-Type, Gas-Rich, Spiral Galaxy. *Astronomical Journal*, 134:1827–1842, November 2007. doi: 10.1086/521645.

G. de Vaucouleurs, A. de Vaucouleurs, and H. G. Corwin, Jr. *Second reference catalogue of bright galaxies. Containing information on 4,364 galaxies with references to papers published between 1964 and 1975.* 1976.

G. de Vaucouleurs, A. de Vaucouleurs, H. G. Corwin, Jr., R. J. Buta, G. Paturel, and P. Fouqué. *Third Reference Catalogue of Bright Galaxies. Volume I: Explanations and references. Volume II: Data for galaxies between 0^h and 12^h. Volume III: Data for galaxies between 12^h and 24^h.* 1991.

J. M. Dickey, E. E. Salpeter, and Y. Terzian. Temperature Distribution of Neutral Hydrogen at High Galactic Latitudes. *Astrophysical Journal, Letters to the Editor*, 211:L77, January 1977. doi: 10.1086/182345.

J. M. Dickey, M. M. Hanson, and G. Helou. NGC 1058 - Gas motions in an extended, quiescent spiral disk. *Astrophysical Journal*, 352:522–531, April 1990. doi: 10.1086/168555.

B. G. Elmegreen and J. Scalo. Interstellar Turbulence I: Observations and Processes. *Annual Review of Astronomy and Astrophysics*, 42:211–273, September 2004. doi: 10.1146/annurev.astro.41.011802.094859.

B. G. Elmegreen, S. Kim, and L. Staveley-Smith. A Fractal Analysis of the H I Emission from the Large Magellanic Cloud. *Astrophysical Journal*, 548:749–769, February 2001. doi: 10.1086/319021.

B. G. Elmegreen, D. M. Elmegreen, and S. N. Leitner. A Turbulent Origin for Flocculent Spiral Structure in Galaxies. *Astrophysical Journal*, 590:271–283, June 2003. doi: 10.1086/374860.

H. I. Ewen and E. M. Purcell. Observation of a Line in the Galactic Radio Spectrum: Radiation from Galactic Hydrogen at 1,420 Mc./sec. *Nature*, 168:356, September 1951. doi: 10.1038/168356a0.

G. Fasano and A. Franceschini. A multidimensional version of the Kolmogorov-Smirnov test. *Monthly Notices of the RAS*, 225:155–170, March 1987. doi: 10.1093/mnras/225.1.155.

G. B. Field. Thermal instability. *Astrophysical Journal*, 142:531, August 1965. doi: 10.1086/148317.

G. B. Field, D. W. Goldsmith, and H. J. Habing. Cosmic-Ray Heating of the Interstellar Gas. *Astrophysical Journal, Letters to the Editor*, 155:L149, March 1969. doi: 10.1086/180324.

F. Fraternali, G. van Moorsel, R. Sancisi, and T. Oosterloo. Deep H I Survey of the Spiral Galaxy NGC 2403. *Astronomical Journal*, 123:3124–3140, June 2002. doi: 10.1086/340358.

A. Gil de Paz, B. F. Madore, S. Boissier, R. Swaters, C. C. Popescu, R. J. Tuffs, K. Sheth, R. C. Kennicutt, Jr., L. Bianchi, D. Thilker, and D. C. Martin. Discovery of an Extended Ultraviolet Disk in the Nearby Galaxy NGC 4625. *Astrophysical Journal, Letters to the Editor*, 627:L29–L32, July 2005. doi: 10.1086/432054.

A. W. Green, K. Glazebrook, P. J. McGregor, R. G. Abraham, G. B. Poole, I. Damjanov, P. J. McCarthy, M. Colless, and R. G. Sharp. High star formation rates as the origin of turbulence in early and modern disk galaxies. *Nature*, 467:684–686, October 2010. doi: 10.1038/nature09452.

A. W. Green, K. Glazebrook, P. J. McGregor, I. Damjanov, E. Wisnioski, R. G. Abraham, M. Colless, R. G. Sharp, R. A. Crain, G. B. Poole, and P. J. McCarthy. DYNAMO - I. A sample of Hα-luminous galaxies with resolved kinematics. *Monthly Notices of the RAS*, 437:1070–1095, January 2014. doi: 10.1093/mnras/stt1882.

P. Hennebelle and E. Audit. On the structure of the turbulent interstellar atomic hydrogen. I. Physical characteristics. Influence and nature of turbulence in a ther-

mally bistable flow. *Astronomy and Astrophysics*, 465:431–443, April 2007. doi: 10.1051/0004-6361:20066139.

E. Holmberg. A photographic photometry of extragalactic nebulae. *Meddelanden fran Lunds Astronomiska Observatorium Serie II*, 136:1, 1958.

R. Ianjamasimanana, W. J. G. de Blok, F. Walter, and G. H. Heald. The Shapes of the H I Velocity Profiles of the THINGS Galaxies. *Astronomical Journal*, 144:96, October 2012. doi: 10.1088/0004-6256/144/4/96.

R. Ianjamasimanana, W. J. G. de Blok, F. Walter, G. H. Heald, A. Caldú-Primo, and T. H. Jarrett. The Radial Variation of H I Velocity Dispersions in Dwarfs and Spirals. *Astronomical Journal*, 150:47, August 2015. doi: 10.1088/0004-6256/150/2/47.

J. Kamphuis and F. Briggs. Kinematics of the extended H I disk of NGC 628 - High velocity gas and deviations from circular rotation. *Astronomy and Astrophysics*, 253:335–348, January 1992.

J. J. Kamphuis. *Neutral Hydrogen in nearby Spiral Galaxies - Holes and High Velocity Clouds*. PhD thesis, PhD Thesis, University of Groningen, (1993), 1993.

I. D. Karachentsev, M. E. Sharina, and W. K. Huchtmeier. A group of galaxies around the giant spiral NGC 6946. *Astronomy and Astrophysics*, 362:544–556, October 2000.

R. C. Kennicutt, Jr., L. Armus, G. Bendo, D. Calzetti, D. A. Dale, B. T. Draine, C. W. Engelbracht, K. D. Gordon, A. D. Grauer, G. Helou, D. J. Hollenbach, T. H. Jarrett, L. J. Kewley, C. Leitherer, A. Li, S. Malhotra, M. W. Regan, G. H. Rieke, M. J. Rieke, H. Roussel, J.-D. T. Smith, M. D. Thornley, and F. Walter. SINGS: The SIRTF Nearby Galaxies Survey. *Publications of the Astronomical Society of the Pacific*, 115:928–952, August 2003. doi: 10.1086/376941.

S. A. Khoperskov and G. Bertin. Synthetic HI observations of spiral structure in the outer disk in galaxies. *Journal of Plasma Physics*, 81(6):495810607, December 2015. doi: 10.1017/S0022377815001439.

A. Kolmogorov. The Local Structure of Turbulence in Incompressible Viscous Fluid for Very Large Reynolds' Numbers. *Akademiia Nauk SSSR Doklady*, 30:301–305, 1941.

M. R. Krumholz and B. Burkhart. Is Turbulence in the Interstellar Medium Driven by Feedback or Gravity? An Observational Test. *ArXiv e-prints*, December 2015.

L. Lanz, A. Zezas, N. Brassington, H. A. Smith, M. L. N. Ashby, E. da Cunha, G. G. Fazio, C. C. Hayward, L. Hernquist, and P. Jonsson. Global Star Formation Rates and Dust Emission over the Galaxy Interaction Sequence. *Astrophysical Journal*, 768:90, May 2013. doi: 10.1088/0004-637X/768/1/90.

M. D. Lehnert, N. P. H. Nesvadba, L. Le Tiran, P. Di Matteo, W. van Driel, L. S. Douglas, L. Chemin, and F. Bournaud. Physical Conditions in the Interstellar Medium of Intensely Star-Forming Galaxies at Redshift~2. *Astrophysical Journal*, 699:1660–1678, July 2009. doi: 10.1088/0004-637X/699/2/1660.

M. D. Lehnert, L. Le Tiran, N. P. H. Nesvadba, W. van Driel, F. Boulanger, and P. Di Matteo. On the self-regulation of intense star-formation in galaxies at z = 1-3. *Astronomy and Astrophysics*, 555:A72, July 2013. doi: 10.1051/0004-6361/201220555.

A. K. Leroy, F. Walter, E. Brinks, F. Bigiel, W. J. G. de Blok, B. Madore, and M. D. Thornley. The Star Formation Efficiency in Nearby Galaxies: Measuring Where Gas Forms Stars Effectively. *Astronomical Journal*, 136:2782–2845, December 2008. doi: 10.1088/0004-6256/136/6/2782.

A. K. Leroy, F. Walter, F. Bigiel, A. Usero, A. Weiss, E. Brinks, W. J. G. de Blok, R. C. Kennicutt, K.-F. Schuster, C. Kramer, H. W. Wiesemeyer, and H. Roussel. Heracles: The HERA CO Line Extragalactic Survey. *Astronomical Journal*, 137: 4670–4696, June 2009. doi: 10.1088/0004-6256/137/6/4670.

M. Lesieur. *Turbulence in Fluids*. Springer, 2008.

C. F. McKee and J. P. Ostriker. A theory of the interstellar medium - Three components regulated by supernova explosions in an inhomogeneous substrate. *Astrophysical Journal*, 218:148–169, November 1977. doi: 10.1086/155667.

J. C. Mihos, P. Harding, C. E. Spengler, C. S. Rudick, and J. J. Feldmeier. The Extended Optical Disk of M101. *Astrophysical Journal*, 762:82, January 2013. doi: 10.1088/0004-637X/762/2/82.

K. M. Mogotsi, W. J. G. de Blok, A. Caldú-Primo, F. Walter, R. Ianjamasimanana, and A. K. Leroy. Hi and CO Velocity Dispersions in Nearby Galaxies. *Astronomical Journal*, 151:15, January 2016. doi: 10.3847/0004-6256/151/1/15.

A. V. Moiseev, A. V. Tikhonov, and A. Klypin. What controls the ionized gas turbulent motions in dwarf galaxies? *Monthly Notices of the RAS*, 449:3568–3580, June 2015. doi: 10.1093/mnras/stv489.

J. C. Muñoz-Mateos, A. Gil de Paz, J. Zamorano, S. Boissier, D. A. Dale, P. G. Pérez-González, J. Gallego, B. F. Madore, G. Bendo, A. Boselli, V. Buat, D. Calzetti, J. Moustakas, and R. C. Kennicutt, Jr. Radial Distribution of Stars, Gas, and Dust in SINGS Galaxies. I. Surface Photometry and Morphology. *Astrophysical Journal*, 703:1569-1596, October 2009. doi: 10.1088/0004-637X/703/2/1569.

J. C. Muñoz-Mateos, S. Boissier, A. Gil de Paz, J. Zamorano, R. C. Kennicutt, Jr., J. Moustakas, N. Prantzos, and J. Gallego. Radial Distribution of Stars, Gas, and Dust in SINGS Galaxies. III. Modeling the Evolution of the Stellar Component in Galaxy Disks. *Astrophysical Journal*, 731:10, April 2011. doi: 10.1088/0004-637X/731/1/10.

C. A. Muller and J. H. Oort. Observation of a Line in the Galactic Radio Spectrum: The Interstellar Hydrogen Line at 1,420 Mc./sec., and an Estimate of Galactic Rotation. *Nature*, 168:357–358, September 1951. doi: 10.1038/168357a0.

P. C. Myers. A compilation of interstellar gas properties. *Astrophysical Journal*, 225: 380–389, October 1978. doi: 10.1086/156500.

A. M. Obukhov. On the distribution of energy in the spectrum of turbulent flow. *Akademiia Nauk SSSR Doklady*, 32:19, 1941.

T. Oosterloo, F. Fraternali, and R. Sancisi. The Cold Gaseous Halo of NGC 891. *Astronomical Journal*, 134:1019, September 2007. doi: 10.1086/520332.

A. O. Petric and M. P. Rupen. H I Velocity Dispersion in NGC 1058. *Astronomical Journal*, 134:1952–1962, November 2007. doi: 10.1086/518558.

G. Pezzulli, F. Fraternali, S. Boissier, and J. C. Muñoz-Mateos. The instantaneous radial growth rate of stellar discs. *Monthly Notices of the RAS*, 451:2324–2336, August 2015. doi: 10.1093/mnras/stv1077.

J. L. Pineda, W. D. Langer, T. Velusamy, and P. F. Goldsmith. A Herschel [C ii] Galactic plane survey. I. The global distribution of ISM gas components. *Astronomy and Astrophysics*, 554:A103, June 2013. doi: 10.1051/0004-6361/201321188.

W. W. Roberts. Large-Scale Shock Formation in Spiral Galaxies and its Implications on Star Formation. *Astrophysical Journal*, 158:123, October 1969. doi: 10.1086/150177.

R. Sancisi, F. Fraternali, T. Oosterloo, and T. van der Hulst. Cold gas accretion in galaxies. *The Astronomy and Astrophysics Review*, 15:189–223, June 2008. doi: 10.1007/s00159-008-0010-0.

S. Sauty, M. Gerin, and F. Casoli. FIR and C^+ emissions of spiral galaxies disks. The example of NGC 6946. *Astronomy and Astrophysics*, 339:19–33, November 1998.

J. Scalo and B. G. Elmegreen. Interstellar Turbulence II: Implications and Effects. *Annual Review of Astronomy and Astrophysics*, 42:275–316, September 2004. doi: 10.1146/annurev.astro.42.120403.143327.

J. Schaye. Star Formation Thresholds and Galaxy Edges: Why and Where. *Astrophysical Journal*, 609:667–682, July 2004. doi: 10.1086/421232.

J. A. Sellwood and S. A. Balbus. Differential Rotation and Turbulence in Extended H I Disks. *Astrophysical Journal*, 511:660–665, February 1999. doi: 10.1086/306728.

G. S. Shostak and P. C. van der Kruit. Studies of nearly face-on spiral galaxies. II - H I synthesis observations and optical surface photometry of NGC 628. *Astronomy and Astrophysics*, 132:20–32, March 1984.

D. Tamburro, H.-W. Rix, A. K. Leroy, M.-M. Mac Low, F. Walter, R. C. Kennicutt, E. Brinks, and W. J. G. de Blok. What is Driving the H I Velocity Dispersion? *Astronomical Journal*, 137:4424–4435, May 2009. doi: 10.1088/0004-6256/137/5/4424.

D. A. Thilker, L. Bianchi, S. Boissier, A. Gil de Paz, B. F. Madore, D. C. Martin, G. R. Meurer, S. G. Neff, R. M. Rich, D. Schiminovich, M. Seibert, T. K. Wyder, T. A. Barlow, Y.-I. Byun, J. Donas, K. Forster, P. G. Friedman, T. M. Heckman, P. N. Jelinsky, Y.-W. Lee, R. F. Malina, B. Milliard, P. Morrissey, O. H. W. Siegmund, T. Small, A. S. Szalay, and B. Y. Welsh. Recent Star Formation in the

Extreme Outer Disk of M83. *Astrophysical Journal, Letters to the Editor*, 619: L79–L82, January 2005. doi: 10.1086/425251.

D. A. Thilker, L. Bianchi, G. Meurer, A. Gil de Paz, S. Boissier, B. F. Madore, A. Boselli, A. M. N. Ferguson, J. C. Muñoz-Mateos, G. J. Madsen, S. Hameed, R. A. Overzier, K. Forster, P. G. Friedman, D. C. Martin, P. Morrissey, S. G. Neff, D. Schiminovich, M. Seibert, T. Small, T. K. Wyder, J. Donas, T. M. Heckman, Y.-W. Lee, B. Milliard, R. M. Rich, A. S. Szalay, B. Y. Welsh, and S. K. Yi. A Search for Extended Ultraviolet Disk (XUV-Disk) Galaxies in the Local Universe. *Astrophysical Journal, Supplement*, 173:538–571, December 2007. doi: 10.1086/523853.

A. G. G. M. Tielens. *The Physics and Chemistry of the Interstellar Medium*. Cambridge University Press, August 2010.

R. B. Tully, H. M. Courtois, A. E. Dolphin, J. R. Fisher, P. Héraudeau, B. A. Jacobs, I. D. Karachentsev, D. Makarov, L. Makarova, S. Mitronova, L. Rizzi, E. J. Shaya, J. G. Sorce, and P.-F. Wu. Cosmicflows-2: The Data. *Astronomical Journal*, 146: 86, October 2013. doi: 10.1088/0004-6256/146/4/86.

H. C. Van de Hulst. Radiostraling uit het wereldruim. II. Herkomst der radiogolven. *Nederlands Tijdschrift voor Natuurkunde*, 11:210–221, 1945.

J. M. van der Hulst, J. P. Terlouw, K. G. Begeman, W. Zwitser, and P. R. Roelfsema. The Groningen Image Processing SYstem, GIPSY. In D. M. Worrall, C. Biemesderfer, and J. Barnes, editors, *Astronomical Data Analysis Software and Systems I*, volume 25 of *Astronomical Society of the Pacific Conference Series*, page 131, 1992.

T. Van der Hulst and R. Sancisi. High-velocity gas in M101. *Astronomical Journal*, 95:1354–1359, May 1988. doi: 10.1086/114731.

P. C. van der Kruit and G. S. Shostak. Studies of nearly face-on spiral galaxies. I - The velocity dispersion of the H I gas in NGC 3938. *Astronomy and Astrophysics*, 105:351–358, January 1982.

P. C. van der Kruit and G. S. Shostak. Studies of nearly face-on spiral galaxies. III - H I synthesis observations of NGC 1058 and the mass distribution in galactic disks. *Astronomy and Astrophysics*, 134:258–267, May 1984.

R. P. van der Marel and M. Franx. A new method for the identification of non-Gaussian line profiles in elliptical galaxies. *Astrophysical Journal*, 407:525–539, April 1993. doi: 10.1086/172534.

S. D. van Dyk, S. D. Hyman, R. A. Sramek, and K. W. Weiler. Supernova 1968D in NGC 6946. *IAU Circ.*, 6045:2, August 1994.

J. van Eymeren, M. Marcelin, B. Koribalski, R.-J. Dettmar, D. J. Bomans, J.-L. Gach, and P. Balard. A kinematic study of the irregular dwarf galaxy NGC 2366 using HI and Hα observations. *Astronomy and Astrophysics*, 493:511–524, January 2009. doi: 10.1051/0004-6361:200809585.

L. van Zee and J. Bryant. Neutral Gas Distribution and Kinematics of the Nearly Face-on Spiral Galaxy NGC 1232. *Astronomical Journal*, 118:2172–2183, November 1999. doi: 10.1086/301082.

E. Vázquez-Semadeni. Are There Phases in the ISM? In M. A. de Avillez, editor, *EAS Publications Series*, volume 56 of *EAS Publications Series*, pages 39–49, September 2012. doi: 10.1051/eas/1256005.

M. G. R. Vogelaar and J. P. Terlouw. The Evolution of GIPSY—or the Survival of an Image Processing System. In F. R. Harnden, Jr., F. A. Primini, and H. E. Payne, editors, *Astronomical Data Analysis Software and Systems X*, volume 238 of *Astronomical Society of the Pacific Conference Series*, page 358, 2001.

K. Wada, G. Meurer, and C. A. Norman. Gravity-driven Turbulence in Galactic Disks. *Astrophysical Journal*, 577:197–205, September 2002. doi: 10.1086/342151.

B. P. Wakker and H. v. Woerden. *High-Velocity Clouds*, page 587. 2013. doi: 10.1007/978-94-007-5612-0_12.

M. G. Wolfire, D. Hollenbach, C. F. McKee, A. G. G. M. Tielens, and E. L. O. Bakes. The neutral atomic phases of the interstellar medium. *Astrophysical Journal*, 443: 152–168, April 1995. doi: 10.1086/175510.